Atomised Spray Plasma Deposition of Functional Polymer Coatings

CASTANEDA-MONTES, ISAIAS

Atomised Spray Plasma Deposition of Functional Polymer Coatings

Isaias Castaneda-Montes

PhD Thesis

Department of Chemistry

Durham University

2021

DECLARATION

The work described in this thesis was carried out in the Department of Chemistry, Durham University between October 2015 and June 2019. It is the original work of the author except where otherwise stated or acknowledged, and hast not been previously submitted for a degree in this or any other university.

STATEMENT OF COPYRIGHT

PUBLICATION

Castaneda-Montes, I.; Ritchie, A. W.; Badyal, J. P. S. Atomised Spray Plasma Deposition of Hierarchical Superhydrophobic Nanocomposite Surfaces. *Colloid Surf.* **2018**, *558*, 192–199.

ACKNOWLEDGEMENTS

I would like to express my gratitude to Prof. Karl Coleman FRSC for his guidance to complete my work, and his kind help and support. The work of this thesis was carried out in the chemistry lab CG98 of Prof. JPS Badyal FRS. Special thanks to lab 98 members: Matt, Bekah, and Hannah for their support during my PhD; to Angus for acquiring the XPS analysis; thanks to Dr. Preeti Garg from the University of Panjab, India, for synthetizing the antibacterial metallosurfactants and carrying out the antibacterial test together with Samantha. N. Barrientos-Palomo; I would like to thank to the staff of the chemistry stores (Annette), solvent stores (Gary), mechanical workshop (Neil), electrical workshop (Dr. Kelvin Appleby, Dr. Bryan Denton, and Omer Ekinoglu), and glassblowing workshop (Aaron, and Malcolm); to Dr. Richard Thompson for the training in the AFM; to T. Davey of the electron microscopy research services at Newcastle University; Mexico-CONACyT supported my studies with the scholarship reference 409139.

To Samantha and my family for their unconditional help and support through our PhD studies.

"*There is no crueler tyranny than that which is perpetuated under the shield of law and in the name of justice"*

–Charles Montesquieu–

ABSTRACT

Atomised spray plasma deposition (ASPD) is a technique used to functionalise surfaces. The atomisation of precursor into electrical discharges allows the deposition of: (i) non-polymerisable precursors, which cannot be deposited through conventional surface functionalisation methods; (ii) viscous or low-vapour-pressure precursors, which cannot be deposited in conventional gas-phase plasma polymerisation; (iii) precursor–nanoparticle slurry. In this thesis, atomised spray plasma deposition was employed to fabricate functional polymer coatings for diverse applications such as liquid repellent, wet electrical, and antibacterial coatings.

Liquid-repellent surfaces were fabricated by the deposition of a mixture of nanoparticles and a perfluorinated precursor forming a highly crosslinked polymer matrix containing the nanoparticles. The wettability of the ASPD nanocomposite coatings resulted in water contact angle values of ~170°; the nanoparticles, acting as nanofillers, enhanced the mechanical properties of the ASPD polymer coatings.

Fluorine-free and low-vapour-pressure precursor was used to fabricate hydrophobic ASPD polymer coatings and the effect of the *in situ* plasma post-treatment of ASPD poly (isodecyl acrylate) coatings was tested. The effect of the plasma post-treatment enhanced the crosslinking degree, mechanical and adhesion properties as well as the enhancement of the wet electrical barrier of the ASPD poly (isodecyl acrylate) coatings preventing the electrical breakdown of microcircuit boards in contact with water for an applied electric field of 10 V mm^{-1}. Further enhanced liquid repellency, mechanical properties, and wet electrical barrier to at higher applied electric field (75 V mm^{-1}) were found for plasma post-treated ASPD 20% w/v (*1H,1H,2H,2H*-perfluorododecyl acrylate–perfluorotributylamine) coatings.

Finally, bis-dodecylamine copper dichloride (CuDDA) metallosurfactant was employed to fabricate antibacterial-agent-release 2% w/v ASPD (CuDDA–isodecyl acrylate) coatings. It is likely that the metallosurfactant remained trapped within the plasma polymer coating through electrostatic interactions because there was a reduction of the antibacterial activity of the antibacterial polymer coating as it leached out. These antibacterial polymer

coating displayed highly antibacterial activity efficiency against Gram negative *E. coli* and Gram-positive *S. aureus* bacteria. The maximum antibacterial efficiency (>99.999%) was found at 10 min of interaction time tested on both bacteria individually on the antibacterial ASPD polymer coating, which is attributed to the synergetic effect of the long hydrophobic alkyl chain and the complexation of the surfactant with Cu^{2+} ions.

Table of Contents

List of Schemes

List of Figures

List of Tables

1. Introduction

1.1 Superhydrophobicity

Superhydrophobicity is the characteristic of some material surfaces to show high water repellency, and self-cleaning properties, these properties are commonly attributed to the lotus leaf effect. In terms of the lotus leaf effect, superhydrophobicity can be achieved through the modification induced surface roughness and surface chemistry. The natural surface roughness, fabrication of nanostructured surfaces, or the incorporation of nanoparticles are the common approaches to modify the surface topography in the fabrication of superhydrophobic surfaces. On the other hand, surface modification with low-surface-energy precursor creates hydrophobic surfaces on natural hydrophilic surfaces; whereas high surface energy precursors, are needed if more hydrophilic surfaces are required.[1]

The water contact angle measurement is an indirect method used to correlate the free surface energy of the material surface with the contact angle formed between the liquid droplet and the solid surface. Regarding to the water contact angle (θ), a surface can be directly classified into two conventional wetting regimes: hydrophilic ($10° < \theta < 90°$) and hydrophobic ($90° < \theta < 150°$).[1] On the other hand, the modification of the surface morphology in conjunction with the surface chemistry allows the obtention of surfaces with extreme wetting regimes, such as superhydrophilic ($\theta < 10°$), which is a nearly-complete wet surface, and superhydrophobic ($\theta > 150°$), which is a highly water-repellent surface.[2] This section will be limited to the discussion of the superhydrophobic properties and the considerations for surface morphology and surface chemistry modifications.

Superhydrophobicity was conceptualised from the natural phenomenon of the lotus leaf (*Nelumbo nucifera*) and its self-cleaning properties described by Barthlott & Neinhuis.[3] This phenomenon is attributed to (i) the hierarchical surface morphology, and (ii) the superhydrophobic wax (surface chemistry) of the lotus leaf—the two main criteria to fabricate superhydrophobic surfaces.

The modification of the surface topography and surface chemistry is essential to make superhydrophobic surfaces. The equilibrium water contact

angle, formed between a rough surface and a water droplet, is explained by the Cassie–Baxter model.[4] This model proposes the formation of trapped air pockets between the liquid droplet and the rough surface. This leads to the reduction of contact lines in the solid–liquid interface where the liquid droplets remain suspended on the top of the porous surface, and thus, increase of the apparent contact angle. The following section will describe the criteria to fabricate superhydrophobic surfaces, the choice of the low surface energy materials, and the obtention of surface roughness as detailed from previous reports.

1.1.1 Superhydrophobic Surfaces

In the fabrication of superhydrophobic surfaces, two factors must be taken in consideration regarding surface wettability: (i) material with low surface energy to modify the surface chemistry and (ii) a hierarchical surface topography either obtained by the nature of the material surface,[5] modified hierarchical surface templates,[34] or induced by introducing nanoparticle fillers.[11,12,13] In other words, the material surface must be chemically and physically modified to reduce the surface energy, and thus, to have weaker adhesion forces than the cohesive forces between the liquid droplet and the superhydrophobic material surface.

The intermolecular forces are composed of two main domains: polar forces and London dispersive forces. Polar forces are created by the permanent dipole moment of molecules and contribute to cohesion forces; London dispersive forces are created by the distortion of electron cloud which is sufficient to cause a temporary dipole moment in the surrounding molecules. Polar liquids have both polar forces and London dispersive forces because of the presence of the polar functional groups (e.g., carboxyl, hydroxyl, water). All molecules have London dispersion forces, indistinctly whether they are polar liquids, thus, non-polar liquids present only London dispersive forces (e.g., perfluorocarbon, hydrocarbon) due to the absent of any polar functional groups. Thus, non-polar liquids have low surface tension, and weak cohesive forces because of the low polarizability of the chemical bonds, for example,

hydrocarbon and perfluorocarbon compounds.[6] Fluorinated materials are commonly proposed for superhydrophobicity because they possess the lowest surface tension due to the saturated perfluoroalkyl chains.[7] Fluorine is the most electronegative element, and in perfluorocarbons, the difference of electronegativity between fluorine and carbon makes the C–F a strong bond and, due to the electron-withdrawing effect of fluorine in the C–F in fluorinated molecules, it reduces the polarisability of the C–F bond, the van der Waals interactions, and the free surface energy.[8] The polarisability and the free surface energy decrease with the number of fluorine substitution, i.e. CF > CF_2 > CF_3, being CF_3 the component with the lowest free surface energy. Therefore, due to the low polarisability of the fluorinated materials, they possess properties such as high chemical, thermal, and weather resistance, low flammability, low dielectric constants, low moisture absorption, low refractive index, and low surface energy which makes them ideal for high liquid repellence.[9]

The wetting behaviour of the superhydrophobic surfaces is described by the proposed Cassie–Baxter wetting model.[4] The modification of the surface topography in superhydrophobic coatings is generally prepared by introducing inorganic nanoparticles mixed with the polymer coating deposited by various methods; the introduction of nanoparticles are used for: enhanced mechanical properties,[10,11] enhanced photocatalytic activities,[20] corrosion protection,[14] tuning of magnetic and electrical properties.[21,14,35,26] Alternatively, surface roughness can be prepared through lithography, creating micropatterns or microprotrusions.[12,13]

Various deposition methods have been used for the fabrication of superhydrophobic surfaces using fluorinated and non-fluorinated polymers in conjunction with nanoparticle fillers, Table 1.1. Numerous nanoparticles have been employed to induce surface roughness, for instance: AlO particles,[17,29] SiO_2 nanoparticles,[33,25] carbon nanotubes,[21,23] kaolin nanoparticles,[28] graphite flakes,[15] TiO_2 nanoparticles,[15,20] iron nanoparticles,[14,35] CuO nanoparticles,[30] ZnO nanoparticles,[22,31,32] silver nanoparticles,[32] graphene nanoplatelets.[26] For example, Ye et al.[21] fabricated a superhydrophobic surface with controllable electrical conductivity using the electrospinning deposition method using a mixture of poly (L-lactide) / polyoxymethylene with carbon nanotubes, and they

reported a water contact angle (WCA) value of ~165°. Nine et al.[15] reported the obtention of superhydrophobic surfaces by combining graphene with diatomaceous earth particles in conjunction with polydimethylsiloxane using a simple spray coating method obtaining ~165° of WCA. Yang et al.[35] prepared a smart and magnetically responsive superhydrophobic coating with reversible-switching wettability and adhesion which operates under the influence of an applied magnetic field. This smart coating was deposited by a combined magnetic-field-directed self-assembly and spray coating method. Zhou et al.[14] prepared a new class of multi-hybrid superhydrophobic coating based on iron nanoparticles and alkyl silanes prepared by a spray coating method, in addition to the superhydrophobic applications, these coatings showed enhanced mechanical properties and corrosion protection immersed in acid or alkaline solutions (0–14 in pH) for ten days. Among the coating deposition methods, the spray coating method is a one-step and not lengthy process for the fabrication of the superhydrophobic coatings, in which both surface chemistry and surface roughness can be modified in one step. A combination of the spray coating and plasma polymerisation will be discussed in the following experimental chapters in which the chemical, mechanical, electrical, and antibacterial properties are enhanced for different applications.

Table 1.1: Summary of superhydrophobic coatings fabricated by various deposition methods with their additional functional applications.

Precursors / Materials	**Deposition Technique**	**Static WCA / °**	**Comments**	**Ref.**
• Fe_3O_4 • Ethyl silicate • Cetyl trimethyl ammonium bromide • *N*-octyl triethoxysiloxane	Spray coating	>170°	• Multiple hybrid coatings for corrosion protection	14
• Diatomaceous earth • Graphite flakes • TiO_2 nanoparticles • Polydimethylsiloxane	• Spray coating • Brush coating • Dip coating	~170°	• Multifunctional barrier coating	15

Precursors / Materials	Deposition Technique	Static WCA / °	Comments	Ref.
• Polybutadiene • CF_4 plasma fluorination	• Solvent casting • Plasma functionalisation	~170°	• Honeycomb structures	16
• Hierarchical boehmite film • Stearic acid	• Hydrothermal growth in acid solution • Deep coating	~169°	• Mechanically and chemically stable towards ultrasonic treatment	17
• Perfluorodecyl-trimethylsiloxane • Tetraethylorthosilicate	• Sol-gel • Spin coating	~167°	• One-step deposition process • Antibacterial activity	18
• Polydimethylsiloxane • Multiwalled carbon nanotubes	• Spin coating • Thermal treatment	~167°	• Stability toward harsh environments	19
• TiO_2 nanoparticles • Octadecyl phosphonic acid	• CF_4 plasma	>165°	• Photocatalytic switchable wettability	20
• Poly (L-lactide) / polyoxymethylene • Multiwalled carbon nanotube	• Electrospinning	~165°	• Superhydrophobic surface with controllable electrical conductivity	21
• ZnO nanoparticles • Stearic acid	• Spray coating	>160°	• Unstable under hydrostatic pressure	22
• High viscosity carbon nanotube paste • Polydimethylsiloxane • Multiwalled carbon nanotubes	• Roll-to-roll process	>160°	• Instabilities for drag reduction	23
• Polystyrene • Polyisoprene • Fluorinated polyol resin	• Spray coating	>160°	• Self-healing • Enhanced mechanical properties	24

Precursors / Materials	Deposition Technique	Static WCA / °	Comments	Ref.
• Perfluorodecyl-trichlorosilane • Perfluorodecyl-dimethyl chlorosilane • SiO_2 nanoparticles	• Spin coating • Chemical vapour deposition	>160°	• Highly transparent superhydrophobic coating	25
• Fluoroacrylic polymer Capstone ST-100® • Electrically conductive carbon black (ENSACO®) • Carbon nanotubes • Graphene nanoplatelets	• Drop casting • Thermal treatment	~160°	• Electrically polymer-based superhydrophobic coating	26
• 3,4-ethylenedioxythiophene • Tetradecane • Octane	• Electrodeposition	~160°	• Multifunctional coatings superhydrophobic coatings	27
• Kaolin particles • Stearic acid • Diethoxydimethylsilane • Triethoxymethylsilane • Perfluorooctanoic acid • Perfluorooctyl silane	• Drop coating	~160°	• Superomniphobic surface	28
• AlO nanoparticles • Perfluorotetradecanoic acid • Perfluorononanoic acid • Stearic acid	• Spray coating	~155°	• Highly branched hydrocarbon groups replaced perfluorocarbon groups	29
• CuO • Vinyl-terminated polydimethylsiloxane • Trimethylolpropane triacrylate	• Dip coating • Thermal treatment	~153°	• Superhydrophobic coatings for oil–water separation membranes	30
• Perfluorooctyl-trichlorosilane • ZnO nanoparticles	• Hydrolysation	~153°	• Lengthy process	31

Precursors / Materials	Deposition Technique	Static WCA / °	Comments	Ref.
• ZnO nanorods • Silver nanoparticles • Stearic acid	• Chemical bath deposition	~153°	• Uniformly distributed coating	32
• Tetraethyl silicate • Perfluorooctyl trichlorosilane • Trichloromethyl-silane • Perfluorodecyl-trichlorosilane	• Chemical vapour deposition • Photolithography • Plasma activation • Dip coating	>150°	• Formation of micropillars	33
• Polydimethylsiloxane	• Replica moulding	~150°	• Biomimetic replica of the lotus leaf	34
• Iron particles • Polydimethylsiloxane	• Spray coating • Self-assembly	~150°	• Smart surface with switchable wettability	35

1.2 Plasmas

1.2.1 Plasma Classification

Plasma is an ionised gas referred as the fourth state of matter following to the increase of temperature that transforms the mater from solid, to liquid, to gas, and to plasma where at least one electron is stripped out from neutral particles. Plasmas are constituted of electrons, ions, excited and neutral particles. Particles found in the excited state can return to the ground state by photon emission, a process which is responsible for the plasma luminosity. The presence of free electrons and the equal density of electrons and ions within the plasmas, allows the plasmas to be electrically conductive and neutral.[36]

Plasmas can be classified, according to their thermodynamic equilibrium, into (i) complete thermodynamic equilibrium, (ii) complete local thermodynamic equilibrium, and (iii) non-local thermodynamic equilibrium. Plasmas in complete thermodynamic equilibrium exist in the stars, fusion plasmas; they are characterised by presenting uniform homogeneous plasmas with high temperatures, and ionisation degree near to 100%, i.e. high-

temperature plasmas may have electron temperatures of ≥ 10^7 K with electron and ion densities ≥ 10^{26} m^{-3}.[36,37] These high-temperature plasmas occur in harsh conditions and are unable to be used in a research laboratory for materials processing. Plasmas in complete local thermodynamic equilibrium are commonly known as thermal plasmas. In plasmas with local equilibrium, the plasma chemical properties, plasma species temperatures are homogenous locally confined in small dimensions related to the Debye length, λ_D. Generally, in thermal plasmas, the temperature of the electron (T_e), and ions (T_i), is equal to the plasma temperature (T_p) ($T_e \approx T_i \approx T_p \leq 10^4$ K) and the electron density varies between 10^{21}–10^{26} m^{-3}.[37,38] Finally, non-local thermodynamic equilibrium plasmas are also known as cold plasmas where there exist a deviation of the particle temperatures and, therefore, the $T_e >> T_i$. The electron energy is much higher than the rest of the particles ($T_e >> T_i$, $T_e \approx 10^4$–10^5 K; $T_i \approx T_p \approx 300$ K), and due to the small mass of the electrons as compared to the other particles, the plasma temperature may remain at room temperature; typically, the electron density of cold plasmas under vacuum is 10^5–10^7 m^{-3}.[37,38]

Cold plasmas are commonly used in plasma chemistry for materials processing or surface functionalisation due to the energetic electrons with high activation energies at a relatively low plasma temperature which can be used for plasma polymerisation, otherwise, it may result unpractical by other means. Therefore, cold plasmas are useful for the synthesis of polymers such as thin functional coatings with tuneable chemical, physical, mechanical, and electrical properties which is the subject of this work.

1.2.2 Plasma Species

The physical parameters of the cold plasmas such as the electron energy, plasma sheath, affect the plasma chemistry in the plasma phase and at the plasma–surface interface. These characteristics depend on intrinsic properties as mentioned in Section 1.2.2 but also to external parameters such as time, flow rate, pressure, power, etc., which affect the synthesis of the final product. Within the plasma, species gain energy through the elastic and inelastic

collisions. Particles exchange energy through elastic collisions, whereas in inelastic collisions there occur some chemical reactions such as dissociation and ionisation either in the gas phase or through surface reactions. In the following sections, the characteristics and chemical reactions attributed to each type of plasma specie are described.

1.2.2.1 Electrons

Electrons are the lightest particle of the plasma species and produced by the application of radiofrequency (RF) power to a gas at low pressure. The electrons gain energy through the electric fields and directed by the magnetic field lines, Section 1.2.3.5. The kinetic energy of the electrons is represented as an electron energy distribution function, Section 1.2.3.1. An electron can transfer their energy to molecules through inelastic collisions. Electrons with energy higher than 3 eV have enough energy to break most of the chemical bonds leading to chemical reactions such as dissociation, and ionisation, producing radicals, ions, photons, lower-energy electrons.[37,39]

1.2.2.2 Ions

Collisions between electrons and molecules produce energetic positive ions (~10 eV) in the plasma, Equation 1.1. Negative ions are present in the plasma, but they do not participate at plasma–surface interaction due to the negative potential formed on the surface, Section 1.2.3.4. It is considered that ions do not respond to the magnetic fields or to the electric fields to gain energy due to their mass as compared to the electrons.[37,39]

$$e^- + X \rightarrow X^+ + 2e^- \qquad \text{Equation 1.1}$$

1.2.2.3 Radicals

Electrons with the energy of 3–5 eV have enough energy to break bonds of most of the organic molecules to form radicals, Equation 1.2:[37,39]

$$e^- + X_2 \rightarrow e^- + X^\bullet + X^\bullet$$ Equation 1.2

Radicals can recombine with other radicals through radical propagation if the molecule contains a functional vinyl group and thus participate in the plasma polymerisation and polymer growth at surfaces.

1.2.2.4 Exited State Molecules and Vacuum Ultraviolet Photons

Energetic electrons (5–10 eV) produce higher energetic collisions with neutral molecules to produce excited species molecules. The excess of kinetic energy is absorbed by the core level electron of the molecule and then it is excited to a higher energy level, Equation 1.3:[37,39]

$$e^- + X_2 \rightarrow e^- + X_2^*$$ Equation 1.3

The excited state molecules have a short life and then release a photon to return to the ground state, Equation 1.4. The released photons are found in the UV–visible electromagnetic range with a variety of energy. The vacuum UV photons have enough energy to cause any chemical reaction such as dissociation or ionisation. The photons in the visible region give the characteristic glow of the plasma.[37,39]

$$X_2^* \rightarrow h\lambda + X_2$$ Equation 1.4

1.2.3 Plasma Parameters

Several parameters affect the plasma density, plasma reactivity, and process efficiency, which are dependent on the energy and density of charged particles. These parameters are the electron temperature, degree of

ionisation, Debye length, plasma frequency, plasma sheath. These parameters need to be considered to sustain the plasma and for plasma processing, and thus, they are required to find the optimum conditions for specific plasma reactor configurations and plasma process.

1.2.3.1 Electron Temperature

The plasma species consist of electrons, ions, radicals, and neutral molecules which can be divided into two categories: electrons, and heavy species corresponding to ions, radicals, and neutral molecules. For plasmas in non-local thermodynamic equilibrium, the electron temperature is much higher than the temperature of the heavy species which remain near to room temperature.[37] Therefore, the electron energy can be represented in terms of electron energy distribution function, f(E).

To determine the electron energy distribution function, it is assumed that the electron velocity distribution is equal in any part of the plasma and that the electric field gradient in the plasma does not affect the electron velocity distribution. Therefore, it is assumed that the electron temperature is equal to the plasma temperature ($T_e = T_p$). Under this consideration, the electron energy distribution is known as Maxwellian energy distribution for the electrons, and it is described by Equation 1.5:[37]

$$f(E) = 2.07E_{av}^{-3/2}\, E^{1/2}\, exp\left(\frac{-1.5E}{E_{av}}\right) \qquad \text{Equation 1.5}$$

where E_{av} is the average energy of electrons.

Therefore, due to the assumption that $T_e = T_p$ in the Maxwellian energy distribution, the Maxwellian energy distribution function provides an approximation of the electron temperature in thermal plasmas or local thermodynamic equilibrium.

In contrast, for low-pressure plasmas calculations, the Druyvesteyn energy distribution is employed. Druyvesteyn energy distribution replaces the assumption made in the Maxwellian energy distribution. The Druyvesteyn

energy distribution is based on: (i) the electric field in the plasma is low enough to neglect the inelastic collision, but high enough for the electron to have much higher energy than the ions; (ii) the frequency of the electric field is much lower than the frequency of the collisions; (iii) the collision frequency is independent of the electron energy. Therefore, the Druyvesteyn energy distribution is a better approximation of the electron energy distribution than the Maxwellian energy distribution for low-pressure plasmas, Equation 1.6:[37]

$$f(E) = 1.04\, E_{av}^{-3/2}\, E^{1/2}\, exp\left(\frac{-0.55E^2}{E_{av}^2}\right) \qquad \text{Equation 1.6}$$

Therefore, the Druyvesteyn distribution gives a better approximation to low-pressure steady plasmas than the Maxwellian distribution, Figure 1.1. Comparing the two different average electron energies (1 eV and 3 eV), it is observed that the Druyvesteyn distribution is characterised by a shift toward higher electron energies as compared to the Maxwellian distribution. The high-energy tail of the electron energy distribution distributes their energy through collision with other species in the plasma, which could lead to the ionisation process in the plasma.[37,39] This is an essential factor to consider in the optimisation of the plasma process or plasma polymerisation.

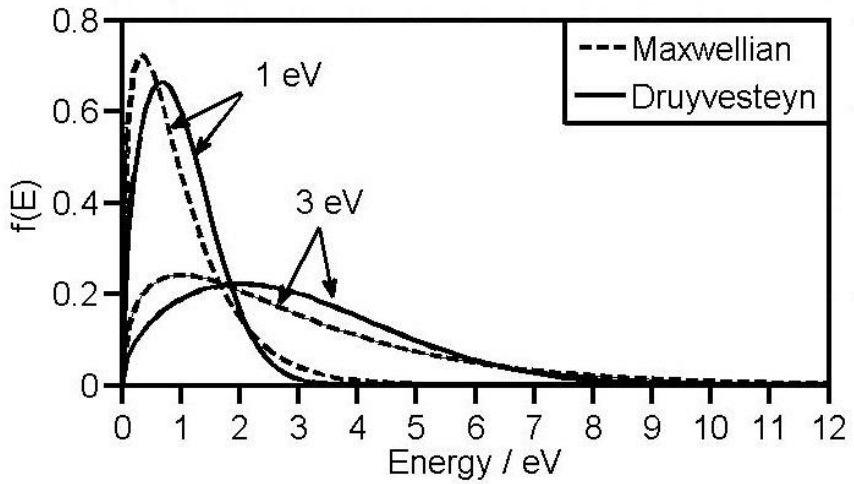

Figure 1.1: Maxwellian (Equation 1.5) and Druyvesteyn (Equation 1.6) electron energy distribution functions. The electron energy distribution functions were plotted at 1 eV and 3 eV indicating the average electron energy. Adapted from reference 37.

1.2.3.2 Ionisation Degree

Another intrinsic parameter that determines the characteristic of plasmas is the ionisation degree. The ionisation degree specifies the density of charged particles as a fraction of the total density of the gas, i.e. the fraction of ionised particles in the gas bulk. The ionisation degree (α) is defined as Equation 1.7:

$$\alpha = \frac{n_i}{n_i + n_n} \qquad \text{Equation 1.7}$$

where n_i, and n_n are the densities of ions and neutral particles. Typically, cold plasmas are weakly ionised with an ionisation degree of $\alpha \approx 10^{-4}$–10^{-7}.[37,40]

1.2.3.3 Debye Length

In the plasma, the positive and negative particles are attracted each other to cancel the charge, which exists under the influence of an electric field. The attraction of the charged particles forms a charged cloud, and beyond the diameter of the charged cloud, there will be no electric field. The local concentration of charged clouds created by the charged particles gives the character to the plasma of quasi-neutrality. Therefore, the Debye length (λ_D), is a dimension that characterises the neutrality breakdown in the plasmas, i.e. the dimension where local charge densities exits, Equation 1.8:

$$\lambda_D = \left(\frac{\varepsilon_o k T_e}{n_e e^2}\right)^{1/2} \qquad \text{Equation 1.8}$$

where ε_o is the permittivity of the free space, and e is the charge of the electron. Typically, the λ_D is in the order of microns, and a sphere volume with a radius equal to the λ_D contains 10^4–10^7 electrons at a $T_e > 1$ eV, and $n_e < 10^6$ m^{-3}.[37,40]

1.2.3.4 Plasma Sheath

The plasma sheath is a region where the surface develops a negative potential relative to the plasma bulk. The density of ions and electrons are equal in the plasma bulk, so quasi-neutrality of the plasma is conserved. The electrons are more energetic and lighter, and thus, electrons reach the surface creating a negative potential rapidly. This causes that only the most energetic electrons reach the surface while the negative potential repels the least energetic electrons. On the other hand, ions are accelerated to the surface by the negative potential in the plasma sheath, Figure 1.2.[39]

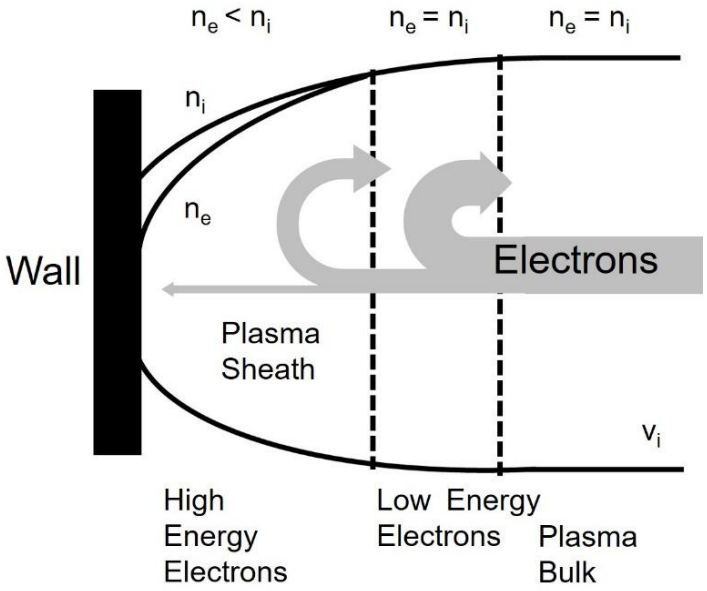

Figure 1.2: Schematic representation of the electrons repelled by the negative potential created in the plasma sheath. Scheme adapted from reference 39.

Therefore, the potential gradient between the plasma bulk (V_f) and the surface (V_p) is defined by Equation 1.9, which eventually reach the equilibrium. In cold plasmas used for chemical functionalisation, the potential difference is in the order of 10–30 V ($V_p - V_f$).

$$V_p - V_f = \frac{kT_e}{e}\left(\frac{1}{2} + \ln\left(\frac{M}{2\pi m_e}\right)\right) \qquad \text{Equation 1.9}$$

where *k* is the Boltzman constant, *e* is the electron charge, M is the molecule mass, m_e is the electron mass.[39]

1.2.3.5 Charged Particle Motion in Electromagnetic Fields

The understanding of the charged particle motion in the plasma is essential to determine the optimum conditions and reactor configuration to carry out the plasma processing. Under the consideration of no collisions, the movement of the charged particles of mass m, charge q, and velocity $\vec{v}$, the charged particles in an applied magnetic field $\vec{B}$, the particle experience a force $\vec{F}$, Equation 1.10:[40]

$$\vec{F} = m\frac{d\vec{v}}{dt} = q\left(\vec{v}\ x\ \vec{B}\right) \qquad \text{Equation 1.10}$$

If the derivative of velocity is multiplied by $\vec{v}$, it results in constant kinetic energy of the charged particle, and thus, the equation is equal to zero (i.e., a derivative of the constant kinetic energy is zero). Therefore, it results that $\vec{v}$ is composed of parallel $\vec{v}_{\parallel}$, and perpendicular $\vec{v}_{\perp}$ to the magnetic field lines which result in two different motions around the magnetic field lines, Equation 1.11 and Equation 1.12. These two motions represent the circular motion ($\vec{v}_{\perp}$) of the charged particle (Equation 1.11) around the magnetic guiding centre, and the linear motion ($\vec{v}_{\parallel}$) with constant velocity around the magnetic guiding centre, resulting in a helical motion, Figure 1.3, with Larmor radius, r_L, Equation 1.13.[40]

$$m\frac{d\vec{v}_{\perp}}{dt} = q\left(\vec{v}_{\perp} x\ \vec{B}\right) \qquad \text{Equation 1.11}$$

$$m\frac{d\vec{v}_{\parallel}}{dt} = q\left(\vec{v}_{\parallel}\ x\ \vec{B}\right) \qquad \text{Equation 1.12}$$

$$r_L = \frac{mv_L}{qB}$$ Equation 1.13

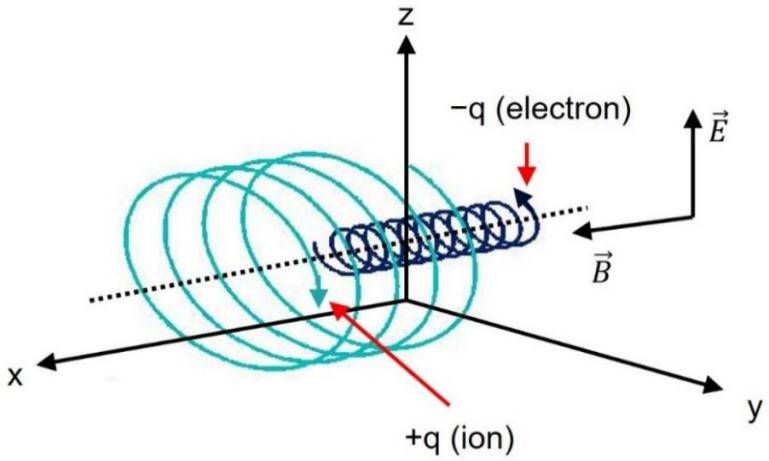

Figure 1.3: Schematic representation of the motion of the electrons and positive ions parallel to the magnetic fields ($\vec{B}$). The electrons and ions gyrate around a magnetic field line (dashed line). The direction of the charged particles changes according to the charge of the particle. Scheme adapted from reference 40.

Therefore, in the presence of electric field $\vec{E}$, the charged particles are exposed to the Lorentz forces, Equation 1.14. The $\vec{E}$ provides kinetic energy to the charged particles and induces constant acceleration perpendicular to the $\vec{E}$ and $\vec{B}$.[40]

$$m\frac{d\vec{v}}{dt} = q\left(\vec{E} + \vec{v}_{\perp}\, x\, \vec{B}\right)$$ Equation 1.14

1.2.4 Types of Plasmas

Cold plasmas are produced by applying power to a gas, and the applied energy creates a breakdown on the gas and the generated electron gain energy from the electric field. There are different energy sources to ignite plasmas, such as the application of direct current (DC), radiofrequency (RF) discharges, or microwave (MW) discharges. The choice of the power supply will depend on the specific method, equipment, and external parameters used

for plasma processing and is independent of the electron energy and temperature. This section will be focused on the description of the plasmas generated by RF discharges.[37,41]

The plasma reactors used for surface material modification or thin-film deposition are commonly driven by three different commercial radiofrequency generators, 40 kHz, 13.56 MHz, and 2.45 GHz.[40] The application of RF discharges between two parallel electrodes or in coils produces the generation of an RF electromagnetic field which sustain the plasma. The RF electromagnetic field is coupled to the electrons in the plasma, and the electrons gain energy from the generated electric field to maintain the plasma, Section 1.2.3.5. The RF discharge can be coupled in two different ways to produce RF electromagnetic fields and produce plasma: inductively coupled plasma (ICP), and capacitively coupled plasma (CCP).

1.2.4.1 Inductively Coupled Plasmas

In inductively coupled plasmas, the RF electric field is coupled to the plasma via an electromagnetic field produced by a helical coil which surrounds the plasma system. The conductive coil is connected to an RF generator which generates an alternating magnetic field, and thus, an electric field within the plasma volume that provides energy to the electrons to sustain the plasma. The flow of the current in the plasma generates a magnetic flux denoted as inductance, L_p, the inductance created by the coil and the matching network (a device used to match and maximise the power transfer from the RF generator to the coil and plasma volume) are used to optimise the power transfer, discharge uniformity, heat dissipation in the coil and plasma—enhancing the performance of the plasma processing. The quantification of the magnetic flux, Φ, is proportional to the magnetic field, H_z, and the inner radius of the conductive coil, r_0, Equation 1.15:[40]

$$\Phi = \mu_o H_z \pi r_0^2 \qquad \text{Equation 1.15}$$

where μ_0 is the vacuum permittivity, the magnetic field (H_z) is proportional to the plasma current, I_p, ($I_p = NI_{coil}$, N = number the turns of the conductive coil; I_{coil} = current on the coil) and inversely proportional to the coil length, L, Equation 1.16. Therefore, by combining Equation 1.15 and Equation 1.16, the plasma inductance (L_p) can be determined by Equation 1.17. The flow of the current around the RF conductive coil induces the generation of electromagnetic field lines, Figure 1.4; each magnetic guiding centre transport the electrons within the plasma while the electrons gain energy from the electric field, Section 1.2.3.5.[40]

$$L_p = \frac{l_p}{L} \qquad \text{Equation 1.16}$$

$$L_p = \frac{\mu_0 \pi r_0^2}{L} \qquad \text{Equation 1.17}$$

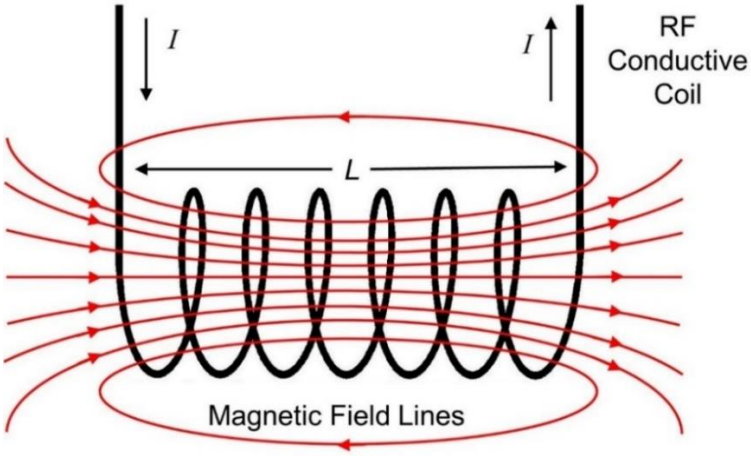

Figure 1.4: Schematic representation of the current flow (I) through the RF conductive coil and the induction of the RF magnetic field lines. Adapted from reference 38.

1.2.4.2 Capacitively Coupled Plasmas

In capacitively coupled plasmas (CCP), RF voltage is applied between two parallel electrodes which generate an oscillating electric field between the parallel electrode plates. Usually, one electrode is grounded, and the other is

powered by an RF generator, Figure 1.5. The CCP produces more energetic ions in direction of the electric field towards the powered electrode as compared to the ICP configuration, although ICP configuration produces more energetic electrons at low applied power. The surface of the electrode is not required to be conductive since the RF voltage discharge can be matched to any kind of impedance. Therefore, due to the parallel electrodes in the CCP configuration, and uniformity of the electric potential across the electrodes, it is possible to obtain consistency in the plasma processing which is determined by the electrode size.[40,41]

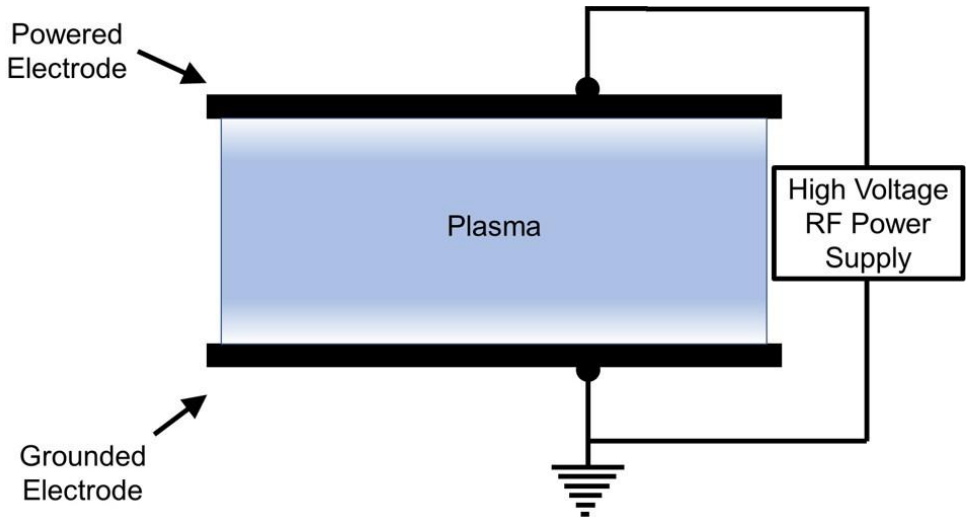

Figure 1.5: Schematic representation of the inductively coupled plasma configuration. Adapted from reference 37.

1.2.5 Plasma Polymerisation

Plasma polymerisation is a type of plasma chemistry where the plasma species activate monomer molecules in the gas phase of the plasma and in the plasma–surface interface to obtain plasma polymers. Generally, in the gas phase of plasma, the monomer molecules are converted into monomer radicals which are then recombined with surface radicals for the propagation and growth of the plasma polymer.[42] The electrons which get energy from the electric field, have enough energy (typically 1–10 eV, Section 1.2.3.1) to dissociate or break chemical bonds, Table 1.2.[43]

Table 1.2: Typical dissociation bond energies of some chemical bonds in organic molecules.[43]

Bond	Dissociation Energy / eV
C–C	3.61
C=C	6.35 (2.74 for π bond)
C–H	4.30
C–N	3.17
C=N	9.26
C–O	3.74
C–F	5.35
O–H	4.83

Plasma polymerisation produces ultrathin polymer coatings which are pin-hole free, with regular structure and variable chemical composition, these properties also depend on the precursor. Depending on the plasma conditions, it is possible to tune the retention of functional groups, enhanced mechanical, chemical, and electrical properties. Some of the external parameters that affect the plasma polymerisation are the Yasuda parameter, which is used to control the energy-per-molecule ratio (W/F) and thus optimising the plasma deposition conditions, the flow rate of the precursor (F), working pressure, applied power (W), reactor configuration, etc.[44] Therefore, these external parameters affect the plasma processing, and allow to set the optimum parameters for the plasma deposition conditions which are required for the synthesis of the plasma polymer.

Depending on the chemical structure of the precursors, plasma polymerisation is carried out by two main mechanisms: conventional radical polymerisation, and ionic deposition.[39,43,44,45] For instance, it has been confirmed that precursors having a polymerisable group follow the conventional radical polymerisation through the unsaturated vinyl group.[46,47,48] While precursors having a non-polymerisable group may follow an ion–molecule chain polymerisation which was observed between a positively

charged oligomer and a neutral species leading to highly branched products.[49,50]

Therefore, the control and optimisation of the external parameters during the plasma polymerisation, affect the chemical, mechanical, and electrical properties of the plasma polymers, thus, the optimum conditions are required to obtain the desired plasma polymer coatings and thicknesses for the required industrial application based on the plasma polymerisation.

1.3 Scope of Thesis

In this thesis, the atomised spray plasma deposition (ASPD) technique was used to fabricate different functional plasma polymer coatings, such as liquid repellent, wet electrical barrier, and antibacterial coatings. The atomisation of the precursor into the plasma allows to the plasma polymerisation of the precursors which are activated by the reactive plasma species and subsequently leading to the plasma polymer growth on the substrate surface. Chapter 3 reports the fabrication of superhydrophobic and oleophobic plasma polymer coatings. The approach to fabricate these liquid repellent coatings was to use perfluorocarbon materials to modify the surface chemistry—because of the —CF_2—, and —CF_3 bonds which are the functional groups with the lowest surface tension—and nanoparticles to induce surface roughness and decrease further the wettability. The mixture of perfluorocarbon precursors with nanoparticles was plasma polymerised through the atomised spray plasma deposition technique yielding high water repellency. The incorporation of nanoparticles not only improved the liquid repellency but also improved the mechanical properties of the plasma polymer coatings.

In Chapter 4, wet electrical barrier coatings were fabricated and tested on micro-circuit boards with the aim to protect electronic devices from electrical failure in contact with moisture or water. Fluorine-free hydrophobic precursor was employed to synthesize the plasma polymer coatings. Hydrophobic hydrocarbon precursors have low polarizability, and low dielectric constant which make them suitable for insulating polymer coatings. The improved method of the ASPD with plasma post-treatment applied to the

plasma polymer coatings allowed to improve the electrical barrier and mechanical properties due to the further increase of the crosslinking degree.

The fabrication of superhydrophobic wet electrical barrier coatings were reported in Chapter 5. The mixture of two perfluorocarbon precursors atomised into the plasma to form superhydrophobic polymer coatings. Because of the different of the physicochemical properties of the perfluorocarbon precursors, the plasma polymer coatings resulted in self-induced roughness which helped to further increase the liquid repellency and enhance the wet electrical barrier coatings.

Chapter 6 reports the fabrication of highly antibacterial polymer coatings. The approach to produce these antibacterial polymer coatings is to use the metallosurfactant composed of a hydrophobic double-long-alkyl-chain surfactant complexed with copper ions which synergistically interact with the bacterial cell wall. The antibacterial metallosurfactant was incorporated into the plasma polymer matrix through the atomised spray plasma deposition technique resulting in a metallosurfactant–polymer nanocomposite coatings.

1.4 References

(1) Celia, E.; Darmanin, T.; Taffin de Givenchy, E.; Amigoni, S.; Guittard, F. Recent Advances in Designing Superhydrophobic Surfaces. *J. Colloid Interface Sci.* **2013**, *402*, 1–18.

(2) Guo, Z.; Liu, W.; Su, B.-L. Superhydrophobic Surfaces: From Natural to Biomimetic to Functional. *J. Colloid Interface Sci.* **2011**, *353*, 335–355.

(3) Barthlott, W.; Neinhuis, C. Purity of the Sacred Lotus, or Escape from Contamination in Biological Surfaces. *Planta* **1997**, *202*, 1–8.

(4) Cassie, A. B. D.; Baxter, S. Wettability of Porous Surfaces. *T. Faraday Soc.* **1944**, *40*, 546–551.

(5) Coulson, S. R.; Woodward, I. S.; Badyal, J. B. S. Plasmachemical Functionalisation of Solid Surfaces with Low Surface Energy Perfluorocarbon Chains. *Langmuir* **2000**, *16*, 6287–6293.

(6) Butt, H.-J; Graf, K.; Kappl, M. *Physics and Chemistry of Interfaces;* Wiley-VCH Verlag GmbH & Co.: Weinheim, 2003.

(7) Shafrin, E. G.; Zisman, W. A. Constitutive Relations in the Wetting of the Low Energy Surfaces and the Theory of the Retraction Method of Preparing Monolayers. *J. Phys. Chem.* **1960**, *64*, 519–524.

(8) Fromel, T.; Knepper, T. P. Mass Spectrometric Approaches to Reveal Biotransformation Products from Per- and Polyfluorinated Chemicals. In *Polyfluorinated Chemicals and Transformation Products;* Springer: London; 2012; pp 41–61.

(9) Vitale, A.; Bongiovanni, R.; Ameduri, B. Fluorinated Oligomers and Polymers in Photopolymerization. *Chem. Rev.* **2015**, *115*, 8835–8866.

(10) Brown, P. S.; Bhushan, B. Durable, Superolephobic Polymer–Nanoparticle Composite Surfaces with Re-entrant Geometry via Solvent-Induced Phase Transformation. *Sci. Rep.* **2016**, *6*, 21048.

(11) Castaneda-Montes, I.; Ritchie, A. W.; Badyal, J. S. P. Atomised Spray Plasma Deposition of Hierarchical Superhydrophobic Nanocomposite Surfaces. *Colloid Surf.* **2018**, *558*, 192–199.

(12) Choo, S.; Choi, H.-J.; Lee, H. Replication of Rose-Petal Structure Using UV-Nanoimprint Lithography. *Matter. Lett.* **2014**, *121*, 170–173.

(13) Feng, J.; Tuominen, M. T.; Rothstein, J. P. Hierarchical Superhydrophobic Surfaces Fabricated by Dual-Scale Electron-Beam-Lithography with Well-Ordered Secondary Nanostructures. *Adv. Funct. Mater.* **2011**, *21*, 3715–3722.

(14) Zhou, Y.; Ma, Y.; Sun, Y.; Xiong, Z.; Qi, C.; Zhang, Y.; Liu, Y. Robust Superhydrophobic Surface Based on Multiple Hybrid Coatings for Application in Corrosion Protection. *ACS Appl. Interfaces* **2019**, *11*, 6512–6526.

(15) Nine, M. J.; Cole, M. A.; Johnson, L.; Tran, D. N. H.; Losic, D. Robust Superhydrophobic Graphene–Based Composite Coatings with Self-Cleaning and Corrosion Barrier Properties. *ACS Appl. Mater. Interfaces* **2015**, *7*, 28482–28493.

(16) Brown, P. S.; Talbot, E. L.; Wood, T. J.; Bain, C. D.; Badyal, J. P. S. Superhydrophobic Hierarchical Honeycomb Surfaces. *Langmuir* **2012**, *28*, 13712–13719.

(17) Liu, L.; Zhao, J.; Zhang, Y.; Zhao, F.; Zhang, Y. Fabrication of Superhydrophobic Surface by Hierarchical Growth of Lotus-Leaf-Like Boehmite on Aluminum Foil. *J. Colloid Interf. Sci.* **2011**, *358*, 277–283.

(18) Privett, B. J.; Youn, J.; Hong, S. A.; Lee, J.; Han, J.; Shin, J. H.; Schoenfisch, M. H. Antibacterial Fluorinated Silica Colloid Superhydrophobic Surfaces. *Langmuir* **2011**, *27*, 9597–9601.

(19) Wang, C.-F.; Chen, W.-Y.; Cheng, H.-Z.; Fu, S.-L. Pressure-Proof Superhydrophobic Films from Flexible Carbon Nanotube/Polymer Coatings. *J. Phys. Chem. C* **2010**, *114*, 15607–15611.

(20) Zhang, X.; Jin, M.; Liu, Z.; Nishimoto, S.; Saito, H.; Murakami, T.; Fujishima, A. Preparation and Photocatalytic Wettability Conversion of TiO2-Based Superhydrophobic Surfaces. *Langmuir* **2006**, *22*, 9477–9479.

(21) Ye, L.; Guan, J.; Li, Z.; Zhao, J.; Ye, C.; You, J.; Li, Y. Fabrication of Superhydrophobic Surfaces with Controllable Electrical Conductivity and Water Adhesion. *Langmuir* **2017**, *33*, 1368–1374.

(22) Li, J.; Jing, Z.; Zha, F.; Yang, Y.; Wang, Q.; Lei, Z. Facile Spray-Coating Process for the Fabrication of Tunable Adhesive Superhydrophobic Surfaces with Heterogeneous Chemical Compositions Used for Selective Transportation of Microdroplets with Different Volumes. *ACS Appl. Mater. Interfaces* **2014**, *6*, 8868–887.

(23) Park, S. H.; Lee, S.; Moreira, D.; Bandaru, P. R.; Han, I. T.; Yun, D. J. Bioinspired Superhydrophobic Surfaces, Fabricated Through Simple and Scalable Roll-to-Roll Processing. *Sci. Rep.* **2015***, 5,* 15430.

(24) Golovin, K.; Boban, M.; Mapry, J. M.; Tuteja, A. Designing Self-healing Superhydrophobic Surfaces with Exceptional Mechanical Durability. *ACS Appl. Mater. Interfaces* **2017**, *9*, 11212–11223.

(25) Xu, L.; Karunakaran, R. G.; Guo, J.; Yang, S. Transparent, Superhydrophobic Surfaces from One-Step Spin Coating of Hydrophobic Nanoparticles. *ACS Appl. Mater. Interfaces* **2012**, *4*, 1118–1125.

(26) Asthana, A.; Maitra, T.; Buchel R.; Tiwari, M. K.; Poulikakos, D. Multifunctional Superhydrophobic Polymer/Carbon Nanocomposites: Graphene, Carbon Nanotubes, or Carbon Black? *ACS Appl. Mater. Interfaces* **2014**, *6*, 8859–8867.

(27) Darmanin, T.; Taffin de Givenchy, E.; Amigoni, S.; Guittard, F. Hydrocarbon versus Fluorocarbon in the Electrodeposition of Superhydrophobic Polymer Films. *Langmuir* **2010**, *26*, 17596–17602.

(28) Qu, M.; Ma, X.; He, J.; Feng, J.; Liu, S.; Yao, Y.; Hou, L.; Liu, X. Facile Selective and Diverse Fabrication of Superhydrophobic, Superolephobic–Superhydrophilic and Superamphiphobic Materials from Kaolin. *ACS Appl. Mater. Interfaces* **2017**, *9*, 1011–1020.

(29) Alexander, S.; Eastoe, J.; Lord, A. M.; Guittard, F.; Barron, A. R. Branched Hydrocarbon Low Surface Energy Materials for Superhydrophobic Nanoparticle Derived Surfaces. *ACS Appl. Interfaces* **2016**, *8*, 660–666.

(30) Su, X.; Li, H.; Lai, X.; Zhang, L.; Liang, T.; Feng, Y.; Zeng, X. Polydimethylsiloxane-Based Superhydrophobic Surfaces on Steel Substrate: Fabrication, Reversibly Extreme Wettability and Oil–Water Separation. *ACS Appl. Interfaces* **2017**, *9*, 3131–3141.

(31) Liu, H.; Sxunerits, S.; Xu, W.; Boukherroub, R. Preparation of Superhydrophobic Coatings on Zinc as Effective Corrosion Barriers. *ACS Appl. Mater. Interfaces* **2009**, *1*, 1150–1153.

(32) Xu, F.; Zhang, Y.; Sun, Y.; Shi, Y.; Wen, Z.; Li, Z. Silver Nanoparticles Coated Zinc Oxide Nanorods Array as Superhydrophobic Substrate for the Amplified SERS Effect. *J. Phys. Chem.* **2011**, *115*, 9977–9983.

(33) Shi, C.; Cui, X.; Zhang, X.; Tchoukov, P.; Liu, Q.; Encinas, N.; Paven, M.; Geyer, F.; Vollmer, D.;Xu, Z.; Butt, H.J.; Zeng, H. Interaction Between and Superhydrophobic Surfaces in Aqueous Solutions. *Langmuir* **2015**, *31*, 7317–7327.

(34) Verbanic, S.; Brady, O.; Sanda, A.; Gustafson, C.; Donhauser, Z. J. A Novel General Chemistry Laboratory: Creation of Biomimetic Superhydrophobic Surfaces Through Replica Molding. *J. Chem. Educ.* **2014**, *91*, 1477–1480.

(35) Yang, C.; Wu, L.; Li, G. Magnetically Responsive Superhydrophobic Surface: In situ Reversible Switching of Water Droplet Manipulation. *ACS Mater. Interfaces* **2018**, *10*, 20150–20158.

(36) Eliezer, S.; Eliezer, Y. *The Fourth State of Matter: An Introduction to Plasma Science*; IOP Publishing: Bristol UK, 2001; pp 1–76.

(37) Grill, A. Cold Plasma in Materials Fabrication: From Fundamentals to Applications; Wiley-IEEE Press: EUA, 1994.

(38) Hippler, R.; Pfau, S.; Schmidt, M.; Schoenbach, K. H. *Low Temperature Plasma Physics.* Wiley-VCH: Berlin, 2001; pp 15–42.

(39) Michelmore, A.; Steele, D. A.; Whittle, J. D.; Bradley, J. W.; Short, R. D. Nanoscale Deposition of Chemically Functionalised Films via Plasma Polymerisation. *RSC Adv.* **2013**, *3*, 13540–13557.

(40) Meichsner, J.; Schmidt, M.; Schneider, R.; Wagner, H.-E. *Nonthermal Plasma Chemistry and Physics*; CRS Press: London, 2013.

(41) Lieberman, A.; Lichtenberg, A. J. *Principles of Plasma Discharges and Materials Processing;* Wiley-Interscience: New Jersey, 2005.

(42) Hegemann, D.; Hossain, M. M.; Korner, E.; Balazs, D. J. Macroscopic Description of Plasma Polymerization. *Plasma Process. Polym.* **2007**, *4*, 229–238.

(43) Yasuda, H. *Plasma Polymerization*. Academic Press Inc.: London, 1985; pp 19–63.

(44) Morosoff, N. An Introduction to Plasma Polymerization. In *Plasma Deposition, Treatment, and Etching of Polymers; dÁgostino,R.;* Academic Press Inc.: San Diego CA, 1990; pp 1–84.

(45) Beck, A. J.; Candan, S.; Short, R. D.; Goodyear, A.; Braithwaite, N. S. J. The Role of Ions in the Plasma Polymerization of Allylamine. *J. Phys. Chem. B.* **2001**, *105*, 5730–5736.

(46) O´Toole, L.; Beck, A. J.; Short, R. D. Characterization of Plasma Polymers of Acrylic Acid and Propionic Acid. *Macromol.* **1996**, *29*, 5172–5177.

(47) Haddow, D. B.; France, R. M.; Short, R. D.; Bradley, J. W.; Barton, D. A Mass Spectrometric and Ion Energy Study of the Continuous Wave Plasma Polymerization of Acrylic Acid. *Langmuir* **2000**, *16*, 5654–5660.

(48) Hegemann, D.; Koner, E.; Guimond, S. Plasma Polymerization of Acrylic Acid Revisited. *Plasma Process. Polym.* **2009**, *6*, 246–254.

(49) O´Toole, L.; Beck, A. J.; Ameen, A. P.; Jones, F. R.; Short, R. D. Radiofrequency-Induced Plasma Polymerisation of Propenoic Acid and Propanoic Acid. *J. Chem. Soc. Faraday Trans*, **1995**, *91*, 3907–3812.

(50) Friedrich, J. The Plasma Chemistry of Polymer Surfaces. Wiley-VCH: Germany, 2012; pp 337–370.

2. Experimental Techniques

2.1 Experimental Details of Atomised Spray Plasma Deposition

Precursors loaded into a sealable glass delivery tube were degassed using 5–6 freeze–pump–thaw cycles. Substrates used for coating were glass microscope slides (Academy Science Ltd.), silicon (100) wafers (0.014–0.024 Ω cm resistivity, Silicon Valley Microelectronics Inc.), microcircuit boards (two copper contact pads mounted on an epoxy glass laminate substrate), and hierarchical-coarse non-woven polypropylene cloth (0.41 mm thick, 22.7 ± 4.4 µm fibre diameter, and dimpled structure 0.68 ± 0.16 µm separation, Spunbond, 70 g m^{-2}, Avoca Technical Ltd., UK). These were cleaned in three steps: ultrasonicated in a 1:1 v/v mixture of propan-2-ol (+99.5 wt %, Fisher Scientific Ltd.) / cyclohexane (+99.7%, Sigma-Aldrich Ltd.) for 5 min and air dried, followed by UV ozone cleaning (ProCleaner model UV.TC.EU.003, BioForce Nanosciences Inc.) for 10 min, and finally ultrasonicated in a 1:1 v/v solvent mixture of propan-2-ol / cyclohexane for 5 min followed by air drying. The hierarchical-course non-woven polypropylene cloth substrates were washed and soaked with ethanol for 20 min, and vacuum dry to remove any excess of ethanol (+99.8%, Fisher Scientific Ltd., UK) before placement downstream in line-of-sight from the atomiser, Figure 2.1.

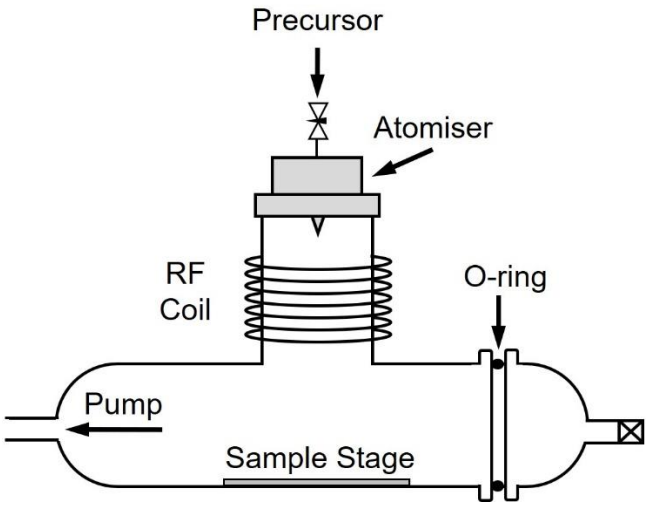

Figure 2.1: Atomised spray plasma deposition (ASPD) chamber. [1]

Atomised spray plasma deposition was carried out in an electrodeless, cylindrical, T-shape glass reactor (volume 1117 cm^3, base pressure of 3 x 10^{-3} mbar, and a leak rate better than 2 x 10^{-9} mol s^{-1})[2] enclosed in a Faraday cage. The chamber was pumped by a 30 L min^{-1} two-stage rotary pump (model E2M2, Edwards Vacuum Ltd.) attached to a liquid nitrogen cold trap, and the system pressure monitored by a Pirani gauge. An inductor–capacitor (L–C) impedance matching network was used to minimise the standing wave ratio for power transmitted from a 13.56 MHz radiofrequency (RF) power supply to a copper coil (4 mm diameter, 7 turns) located downstream from an atomiser (20 µm diameter median droplet size,[3,4] model No. 8700-120, Sono-Tek Corp.), which was driven by a broadband ultrasonic generator (120 kHz, model No. 06-05108, Sono-Tek Corp.). Prior to each deposition, the chamber was scrubbed with detergent, rinsed with propan-2-ol and acetone (+99%, Fisher Scientific Ltd.), and oven dried. Next, a continuous-wave air plasma was run at 0.2 mbar pressure and 50 W power for 30 min to remove any remaining trace contaminants from the chamber walls. Then, ambient-temperature atomised spray plasma deposition was carried out using 30–50 W continuous-wave plasma in conjunction with the atomisation of the precursor solution. Upon plasma extinction, the atomiser was switched off, and the system was evacuated to base pressure, followed by venting to atmosphere.

2.2 Experimental Details of X-ray Photoelectron Spectroscopy

Deposited layers were analysed by X-ray photoelectron spectroscopy (XPS) using a VG ESCALAB II electron spectrometer equipped with a non-monochromatic Mg Kα X-ray source (1253.6 eV) and a concentric hemispherical analyser. Photoemitted electrons were collected at a take-off angle of 20° from the substrate normal with electron detection in the constant analyser energy mode (CAE, pass energy = 20 eV).[5] Experimentally determined instrument sensitivity (multiplication) factors were C(1s): N(1s): F(1s): O(1s): Si(2p): Zn(2p) equals 1.00:0.70:0.25:0.35:0.97:0.056.[5] Data analysis of the XPS spectra data was carried out in an Excel spreadsheet,

where a linear background was subtracted from core level spectra and then fitted using Gaussian peak shapes with a constant full-width-half-maximum (FWHM).[6,7] Each Gaussian peak shapes was fitted to the corresponding chemical environment of the elements presented in the plasma polymer coating. All binding energies are referenced to the Mg $K\alpha_{1,2}$ C(1s) –$\underline{C}F_2$– peak at 291.2 eV binding energy in the case of the ASPD perfluorinated polymer coatings,[8,9] and to the Mg $K\alpha_{1,2}$ C(1s) –$\underline{C}_xH_y$– peak at 285.0 eV binding energy for the ASPD hydrocarbon polymer coatings.

2.3 Experimental Details for Infrared Spectra Acquisition

Fourier transform infrared (FTIR) analysis was carried out using a FTIR spectrometer (Spectrum One, Perkin Elmer Inc.) equipped with a liquid-nitrogen-cooled mercury-cadmium-telluride (MCT) detector. The spectra were averaged over 285 scans at a resolution of 4 cm^{-1} across the 450–4000 cm^{-1} range. Reflection–absorption infrared spectroscopy (RAIRS) of ASPD nanocomposite layer coated silicon wafers was performed using a variable angle reflection–absorption accessory (Specac Ltd.) fitted with mirrors aligned at an angle of 66° to the substrate normal. Attenuated–total–reflection (ATR) spectra of liquid and powder precursors were obtained using a single reflection type II-a diamond brazed into tungsten carbide accessory (Golden Gate, Specac Ltd.).

2.4 Experimental Details of Scanning Electron Microscopy

ASPD coated silicon wafers were mounted onto carbon disks supported by aluminium stubs, and then covered with a 5–10 nm evaporated gold layer (Polaron SEM Coating Unit, Quorum Technologies Ltd.). Surface morphology images were acquired from a scanning electron microscope (model Vega 3LMU, Tescan Orsay Holding, a.s.) operating in secondary electron detection mode at an accelerating voltage of 8 kV, and a working distance of 8–10 mm. For cross-sectional SEM images, the ASPD coated silicon wafers were

fractured by freezing in liquid nitrogen before mounting onto carbon disks supported by aluminium stubs.

2.5 Experimental Details of Film Thickness Measurements

Film thickness measurements were carried out only on smooth ASPD perfluorotributylamine coatings deposited onto silicon wafer substrates using a spectrophotometer (model NKD-6000, Aquila Instruments Ltd.). A monochromated UV-visible light (using a parallel (P) polarised light source at 30° incident angle) source passes through the polymer film of the plasma polymer coated sample over a range of wavelengths (350–1000 nm). Then, the incident light is reflected from the interface between the polymer film and the shiny silicon wafer substrate. The reflectance curve is a function of the wavelength which depends on the film thickness and optical properties—refractive index (n) of the polymer film, and the extinction coefficient (k). The obtained raw reflectance data were fitted to a Cauchy model for dielectric materials[10] using a modified Levenberg–Marquardt algorithm (version 2.2 software, Pro-Optix, Aquila Instruments Ltd.).[11] Given that the transmittance–reflectance measurements are challenging to analyse in transparent substrates due to the optical imperfections (e.g., metallic impurities, birefringence, manufacturing stress), silicon wafer substrates were used as an opaque substrate to obtain the reflectance curves (no transmittance is detected).

2.6 Experimental Details of Contact Angle Analysis

Sessile drop static contact angle measurements were carried out at 20 °C using a video capture apparatus in combination with a motorised syringe (model VCA 2500XE, A.S.T. Products Inc.). 1 µL droplets of ultrahigh-purity water (B.S. 3978 grade 1) and hexadecane (99%, Sigma-Aldrich Ltd.) were employed as probe liquids for hydrophobicity and oleophobicity, respectively. Advancing and receding contact angle values were determined by respectively

increasing the dispensed 1.0 µL liquid drop volume by a further 1.0 µL, and then decreasing the liquid drop volume by 1.0 µL.[12] Contact angle hysteresis was determined by the difference between the advancing and receding contact angle values.

2.7 Microindentation Hardness Test

Microindentation hardness is a technique that provides evidence of the mechanical properties of materials based on their plastic deformation. The plastic deformation is linearly correlated to the material´s tensile strength—indicating the stress-strain deformation measuring the resistance to plastic deformation of materials as a response to an applied force. In other words, microindentation hardness indicates the hardness of the material resistance to localised plastic deformation, for example, small indents or scratches.[13]

The Vickers hardness test is a standard method to measure the hardness of materials.[14] In the Vickers hardness test, a diamond indenter with a square shape is employed to produce a well-defined shape controlled by the applied force and load rate. The diagonals (d_1 and d_2) produced by the microindentation are measured by an optical microscope after load removal, Figure 2.2. The Vickers hardness number is then obtained by dividing the surface area of the Vickers indenter's shape by the applied force, Equation 2.1:[14]

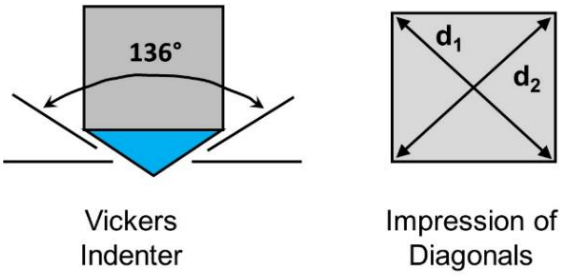

Figure 2.2: Schematic representation of the Vickers indenter and the impression of the indenter on the sample.

$$HV = 0.0018544\, x\, \frac{P}{d_m^2} \qquad \text{Equation 2.1}$$

where HV is given in GPa, force (P) in Newton, and mean diagonal (d_m) in mm. Therefore, this microindentation technique is useful to measure the hardness (scratch resistance) of thin polymer coatings.

Vickers hardness (HV) values were measured using a micro Vickers hardness tester (model MVK-H2, Mitutoyo Inc.) and then converted into GPa. A standard Vickers indenter tip was employed with applied loads of 98, 245, 490, and 980 mN (international standard test ASTM E384-11e1).[14] The tip load was applied for 10 s, at an indentation speed of 3 μm s^{-1} and then unloaded over a period of 10 s. At least 5 different sampling points across the surface were analysed for each applied load value.

2.8 Electrical Barrier Coatings

The dielectric breakdown of an insulating material occurs when the applied electric field surpasses the dielectric strength of the insulating material, and the electrons flow creates conductive channels across the insulating material—resulting in the material failure. The choice of insulating material with sufficiently low dielectric constant and large film thickness can act synergistically to prevent the dielectric breakdown.[15]

During the dielectric breakdown, the electron transport is initiated from the cathode (negative potential) creating conductive channels through the polymer material. These electrons lose their energy through ionisation impact with the polymer molecules and thus damaging the insulating materials. Then, the electrons continue to gain kinetic energy from the applied electric field, and thus, creating an electron avalanche which results in the material damage.[15,16]

On the other hand, the application of the electric field through a polymer material induces a permanent change of the dipole moment resulting in the polarisation of the molecules. The change of polarisability depends on the change of the dipole moment induced by the applied electric field, and it depends on the electrical strength of the molecule.[17] Higher polarisation is found in polar molecules, whereas perfluorocarbon and hydrocarbon display low polarisation and thus lower dielectric constant. Furthermore, polarisation

is related to the refractive index and molar refraction of organic molecules (molar refraction of some chemical bonds,[18] [10^{-6} m^3]: 1.296 for C–C; 1.44 for C–F; 1.676 for C–H; 3.32 for C=O; 4.17 for C=C), and thus, to the dipole moment induced by the applied electric field.[18] Therefore, the low molecular refraction indicates low dielectric constant and this principle can be used in the design of insulating polymer materials (i.e., perfluorinated or alkyl chains functionalised coatings) to encapsulate electronic devices.

2.8.1 Experimental Details of the Electrical Barrier Test

The micro-circuit board consists of two copper contact pads connected to a copper circuit on top of a small epoxy glass laminate substrate. Prior to ASPD deposition, the copper contact pads were covered with a small strip of single-sided adhesive tape (product code 1443170, Henkel Ltd.) so that the copper contact pads are free of plasma polymer coating and cleaned with a cotton bud soaked in acetone (+99.8 wt.%, Fisher Scientific Ltd.) for subsequent electrical barrier tests. Further details of the micro-circuit board preparation have been reported by Fraser et al.[19]

The wet electrical breakdown of the ASPD plasma polymer coated micro-circuit boards was evaluated by immersing the ASPD coated micro-circuit boards in tap water (156 µS cm^{-1} conductivity, Northumbrian Water) and measuring the electrical resistance at a fixed voltage. Tap water was used to test the wet electrical barrier of the ASPD coated micro-circuit boards as it represents the leading cause of electrical failure of the electronic devices, causing either a short circuit or localised corrosion. A multimeter (with a lower detection limit of 10 nA, Keithley 2000, Tektronix UK Ltd.) was used to measure the current flow for each ASPD coated micro-circuit board connected to a variable voltage supply (Model PS-6010, Instek Ltd.). The voltage applied across the circuit was checked using a hand-held multimeter (model 72-770, Tenma Ltd.). Standard wires and connectors were employed (Flexiplast 2 V, 0.75 mm^2 cross-sectional area, 196 strands, 0.07 mm diameter, negligible internal resistance, Multicontact UK Ltd.).

Two small crocodile clips were carefully cleaned with acetone to remove any contaminants and then fed through two holes in a support lid to hold the microcircuit board in place, Figure 2.3. This was lowered into a 50 mL glass beaker filled with 25 mL of equilibrated tap water (20 °C).

A fixed voltage was then applied across the 0.8 mm gap between the microcircuit board copper tracks while immersed in water (e.g., 8 V corresponds to an electric field of 10 V mm^{-1}). Current measurements were taken every 30 s over a 13 min period. At this stage, the final electrical resistance was calculated using Ohm's law.

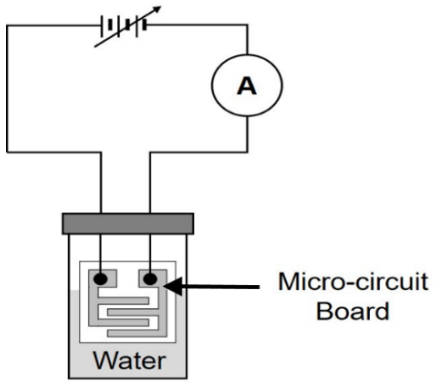

Figure 2.3: Circuit diagram for wet electrical barrier testing of ASPD micro-circuit board. Adapted from reference 19.

2.9 Bacteria–Surface Interaction

Bacteria are found around our environment, within the water, air, food, and living beings maintaining the life balance in our ecosystems. Besides, bacteria may play an essential role in different sectors, such as medicine, food processing, water treatment, bioremediation, insect pest control, and so on.[20] However, there exist a small proportion of pathogenic bacteria that, in a considerable bacterial concentration, may cause diseases to humans or animals and then easily propagated through the environment of any surface exposed to bacteria through ill animals or patients. For instance, in hospitals or health care centres, there is a risk of potential of cross-contamination through the air, contaminated environmental surfaces etc.[21,22] which may be

due to poor hygiene control or improper instrument or food handlings leading to the bacterial infection to other patients.[23] Thus, one proposed approach which may reduce the bacteria propagation is the functionalisation of surfaces with antibacterial agents. Therefore, in the following section, the physiological characteristics of bacteria will be described.

2.9.1 Characteristics of the Bacterial Cell Wall

Bacteria are single-celled microorganisms with different physical appearances such as spherical (coccus), rod-shaped (bacillus), and spiral with a size range from 0.2–2 μm in diameter and from 2–8 μm in length. Bacterial cell walls are mainly composed of a protein complex called peptidoglycan which surrounds the cytoplasmatic membrane acting as a physical barrier to protect the interior of the bacterial cell.[24] A method used to classify bacteria according to their structural difference and bacterial cell wall composition is the Gram stain method.[25]

2.9.2 Gram-Positive Bacterial Cell Wall

Gram-positive bacteria cell wall (e.g., *Staphylococcus aureus*) is composed of two layers: the plasma membrane, and the cell wall (the cell wall is composed of a peptidoglycan layer of 20–80 nm thick), Figure 2.4. Between the peptidoglycan layer and the plasma membrane, there is a cytoplasmic space bonded between the peptidoglycan and the plasma membrane. This cytoplasmic region contains a high concentration of transport proteins and degradative enzymes where important enzymatic reactions occur. The function of the plasma membrane (typically contains phospholipids and proteins) is to transport the nutrients into the bacterial cell but also to protect the cytoplasm. The peptidoglycan is a combination of repeating disaccharide units connected by polypeptides which surround and offer protection to the bacterial cell.[24,25]

2.9.3 Gram-Negative Bacterial Cell Wall

The cell wall of the Gram-negative bacteria (e.g., *Escherichia coli*) consists of three layers: the plasma membrane, and the cell wall, which is composed by a thin layer of peptidoglycan (1–3 nm in thickness), and an extra layer of outer membrane as compared with the Gram-positive bacteria, Figure 2.4. The plasma membrane and the peptidoglycan layers have similar compositions as the Gram-positive bacterial cell wall, and these layers are bonded together by the periplasmic space, i.e. a gel-like liquid found between the plasma membrane and outer membrane. One of the characteristics that distinguish the Gram-negative bacteria from the Gram-positive bacteria is the thin layer of the peptidoglycan located between the plasma membrane and the outer membrane. The thin layer of peptidoglycan makes the Gram-negative bacterial cell wall more flexible, although it makes it more susceptible to cell disruption. On the other hand, the outer membrane, having a strong negative charge, is composed of lipopolysaccharides, lipoproteins, and phospholipids. This extra outer membrane functions as a physical barrier to some antibiotic agents and thus makes the Gram-negative bacteria more antibiotic-resistant than the Gram-positive bacteria.[24,25]

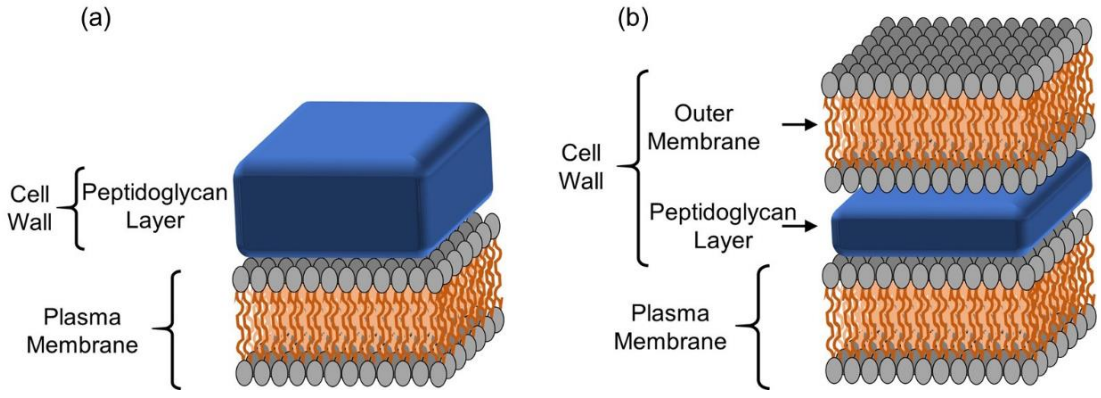

Figure 2.4: Bacterial cell wall structures of: (a) Gram-positive bacteria, and (b) Gram-negative bacteria. Adapted from reference 25.

2.9.4 Bacterial Growth

Bacterial growth is typically carried out in a culture medium, a nutrient material used to sustain the growth of bacteria. Bacteria that are cultivated in the nutrient material to grow and multiply on the culture medium are known as a culture. Typically, the process of bacterial growth implies to prepare the bacterial culture by placing a single colony of bacteria into a sterile liquid nutrient medium (agar), the bacterial culture is then incubated and grown for several hours, following by sampling the broth to inoculate bacteria in a separate sterile cuvette, then incubated for a period of time onto each sample to finally counting the number of bacteria colonies after the incubation of bacteria onto each sample. [24,25]

The bacterial growth comprises 4 phases which describe the kinetics of bacterial growth as a function of the time: lag phase, log phase, stationary phase, and death phase, Figure 2.5. During the lag phase, the bacterial growth has little or no change in the bacterial concentration; instead, they are adjusting to their environment and preparing to metabolise different enzymes and molecules. In the log phase, bacteria undergo the cell division (binary fission), and they are multiplied exponentially. During the log phase, bacteria are metabolically active, and thus, in this step is when bacteria are commonly used to carry out different bacteria analysis, e.g. antibacterial test. In the stationary phase, the bacterial growth rate and the bacterial death rate reach an equilibrium and the nutrient concentration is nearly exhausted. When the bacteria death rate surpasses the bacteria growth rate, the bacteria population decrease and this phase is known as the death phase, Figure 2.5. Therefore, during the performance of the antibacterial test, bacteria are taken when their bacterial concentration reaches the mid-log phase.[24,25]

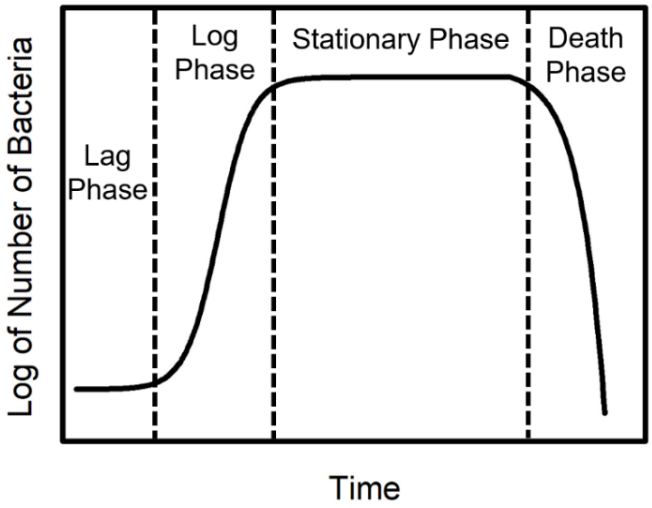

Figure 2.5: Bacterial growth curve following sequential bacterial growth phases: lag phase, log phase, stationary phase, and death phase. It is adapted from reference 25.

2.9.5 Optical Density of Bacterial Culture

An indirect method to estimate the bacterial number of a bacterial culture contained into a polypropylene cuvette is by measuring the absorbance of the bacterial culture through a spectrophotometer. The cuvette containing the bacterial culture is placed inside a spectrophotometer where an incident light (commonly using a light beam with a wavelength of 600 nm) passes through the cuvette and then the absorbance of the transmitted light is registered by the spectrophotometer. The transmitted light is a function of the absorbance, and thus, is proportional to the concentration of substances as described by the Beer-Lambert law stating that the absorbance of a substance is proportional to the concentration of solutions. Therefore, the absorbance of the bacterial culture is called optical density ($OD_{600\ nm}$) and this OD readout can be related to the bacterial plate counts to estimate the number of bacteria in the bacterial culture—in practice, a typical OD600 nm is 0.4 which indicates the number of bacteria in the bacterial culture in the mid-log of the growth phase, the phase at which the bacteria are grown to carry out the antibacterial test.[24,25,26]

2.9.6 Antibacterial Test: Dilution Method

2.9.6.1 Materials

For antibacterial testing, the polypropylene cloth (0.41 mm thick, 22.7 ± 4.4 µm fibre diameter, and dimpled structure 0.68 ± 0.16 mm separation, Spunbond, 70 g m^{-2}, Avoca Technical Ltd., UK[27]) samples were cut into pieces of 5 mm x 5 mm size. Bacteria used were: Gram-positive *Staphylococcus aureus* (FDA209P, an MSSA strain; ATCC 6538P); and Gram-negative wild-type *Escherichia coli* BW25113 (CGSC 7636; rrnB3 ΔlacZ4787 hsdR514 Δ(araBAD)567 Δ(rhaBAD)568 rph–1).

2.9.6.2 Preparation of Bacterial Cultures

For each bacteria species, bacterial cultures were prepared using 5 mL of sterile (121 °C for 15 min in an autoclave (model Vario 1528, Dixons Ltd.)) Lysogeny Broth (LB) media (L3022, Sigma-Aldrich, Inc.) at 2% w/v in Milli-Q® water, starting with a single bacterial colony, and grown for 16 h at 37 °C in a shaking incubator (model Stuart Incubator SI500, Cole-Parmer Instrument Company LLC.) set at 120 rpm. Then, 50 µL of the overnight bacterial culture was used to separately inoculate bacteria in a sterile polystyrene cuvette (10 mmm model 67.742, Sarstedt AG) containing 1 mL of 2% w/v LB media. The cuvette was covered with plastic film (Parafilm, Cole-Parmer Instrument Company LLC.) and bacteria grown as before at 37 °C in a shaking incubator set at 120 rpm. Optical densities $OD_{600\ nm}$ = 0.400 (0.407 ± 0.006 for *S. aureus*), and 0.404 ± 0.007 for *E. coli*) were measured using a spectrophotometer (model DS-11, DeNovix Inc.) to provide bacterial cultures in the mid-log phase of growth.[28]

2.9.6.3 Antibacterial Test

Antibacterial tests for Gram-positive *Staphylococcus aureus* and Gram-negative *Escherichia coli* were undertaken by loading 96 well plates (Sarstedt

AG) with either control or ASPD metallosurfactant-polymer-coated non-woven polypropylene cloth (a 5 mm x 5 mm piece loaded to each well plate). Then, 10 µL of the prepared bacterial culture was dispersed onto each cloth to allow the microorganisms to interact with the cloth surface for a fixed period and temperature (1 min, 2 min, 5 min, and 10 min at room temperature; 4 h, and 16 h at 30 °C, model Bacterial incubator 250, LMS Ltd.). Next, after the interacting time between the bacteria and treated cloth, 90 µL of sterile 2% w/v LB media was pipetted into each well and mixed with the bacteria present, to recover a ten-fold dilution (10^{-1}) of bacteria. Further, ten-fold serial dilutions were performed to give 10^{-2}, 10^{-3}, 10^{-4}, 10^{-5}, 10^{-6}, diluted bacterial concentrations. Colony-forming unit (CFU) plate counting was then carried out by pipetting 10 µL diluted bacterial solution from each sample onto sterile semi-log LB agar plates (EZMix™ powder, dust free, fast-dissolving fermentation medium, Sigma-Aldrich Inc.) followed by incubating for 16 h at 30 °C to form visible bacterial colonies. Finally, the number of bacterial colonies visible at each dilution were counted (if present) to calculate the corresponding CFU mL^{-1}. The measurements reported are the mean and standard deviation of at least three independent experiments.

For recycling experiments, 10 µL of the prepared bacterial culture was dispersed onto each cloth to allow the microorganisms to interact with the surface for 4 h at 30 °C (model Bacterial Incubator 250, LMS Ltd.). The tested samples were taken out from the $x10^{-1}$ solution, rinsed with Milli-Q® water for 1 min, and thoroughly dried in preparation for the next test cycle. CFU plate counting carried out as described previously.

2.10 References

(1) Castaneda-Montes, I.; Ritchie, A. W.; Badyal, J. P. S. Atomised Spray Plasma Deposition of Hierarchical Superhydrophobic Nanocomposite Surfaces. *Colloid Surf.* **2018**, *558*, 192–199.

(2) Ehrlich, C. D.; Basford, J. A. Recommended Practices for the Calibration and Use of Leaks. *J. Vac. Sci. Technol. A* **1992**, *10*, 1–17.

(3) Berger, H. L.; Mowbray, D. F.; Copeman, R. A.; Russell, R. J. Ultrasonic Atomizing Nozzle and Method. U.S. Patent US 7,712,680 B2, May 11, 2010.

(4) Sono-Tek, http://www.sono-tek.com/drop-size-and-distribution/ (accessed Mar 08, 2018).

(5) Briggs, D. XPS: Basic Principles, Spectral Features and Qualitative Analysis. In *Surface Analysis by Auger and X-ray Photoelectron Spectroscopy*; Briggs, D., Grant, J. T., Eds.; IM Publications and Surface Spectra Limited: England, 2003: pp 52–54.

(6) Friedman, R. M.; Hudis, J.; Perlam, M. L. Chemical Effects on Linewidths Observed in Photoelectron Spectroscopy. *Phys. Rev. Lett.* **1972**, *29*, 692–695.

(7) Evans, J. F.; Gibson, J. F.; Moulder, J. H.; Hammond, J. S.; Goretzki, H. Angle resolved ESCA Analysis of Plasma Modified Polystyrene. Fresenius *J. Anal. Chem.* **1984**, *319*, 841–844.

(8) Clark, D. T.; Shuttleworth, D. Plasma Polymerization. II. An ESCA Investigation of Polymers Synthesized by Excitation of Inductively Coupled RF Plasma in Perfluorobenzene and Perfluorocyclohexane. *J. Polym. Sci., Polym. Chem. Ed.* **1980**, *18*, 27–46.

(9) Hynes, A. M.; Shenton, M. J.; Badyal, J. P. S. Pulsed Plasma Polymerization of Perfluorocyclohexane. *Macromolecules* **1996**, *29*, 4220–4225.

(10) Dieblod, A. C.; Chism, W. W. Characterisation and Metrology of Medium Dielectric Constant Gate Dielectric Films. *In High Dielectric Constant Materials: VSLI MOSFET Applications;* Huff, H. R., Gilmer, D. C., Eds.; Springer-Verlag: Berlin, 2005; p 486.

(11) Lovering, D. NKD-6000 Technical Manual; Aquila Instruments: Cambridge, U.K., 1999.

(12) Johnson, R. E.; Dettre, R. H. Wetting of Low-Energy Surfaces. In *Wettability*; Berg, J. C., Ed.; Marcel Dekker Inc. New York, 1993, p 13.

(13) Callister, W. D. Fundamentals of Materials Science and Engineering. John Wiley & Sons, Inc.: New York, 2001, pp 176–181.

(14) ASTM, ASTM Standard E 384–11e1, Standard Test Method for Knoop and Vickers Hardness of Materials, ASTM, International, West Conshohocken, PA, 2011.

(15) Ahmad, Z. Polymeric Dielectric Materials. In *Dielectric Materials.* IntechOpen: London, UK; pp. 3–23.

(16) Zakrevskii, V. A.; Sudar, N. T.; Zaopo, A.; Dubitsky, Y. A. Mechanism of Electrical Degradation and Breakdown of Insulating Polymers. *J. Appl. Phys.* **2003**, *93*, 2135–2139.

(17) Carey, F. A.; Sundberg, R. J. Advanced Organic Chemistry Part A: Structure and Mechanisms. Springer: New York, 2007; pp 1–24.

(18) Blythe, T.; Bloor, D. Electrical Properties of Polymers. Cambridge University Press: Cambridge, 2005; pp 27–58, 186–195.

(19) Fraser, R. C.; Carletto, A.; Wilson, M.; Badyal, J. P. S. Plasmachemical Double Click Thiol–ene for Wet Electrical Barrier. *ACS Appl. Mater. Interfaces* **2016**, *8*, 21832–21838.

(20) Pascual-Diez, A. Antibacterial Activity of Nanomaterials. *Nanomaterial* **2018**, *8*, 359–364.

(21) Lejeune, P. Contamination of Abiotic Surfaces: What a Colonizing Bacterium Sees and How to Blur it. *Trend Microbiol.* **2003,** *11*, 179–184.

(22) Hedin, G.; Rynback, J.; Lore, B. Reduction of Bacterial Surface Contamination in the Hospital Environment by Application of a New Product with Persistent Effect. *J. Hosp. Infect.* **2010**, *75*, 112–115.

(23) Russotto, V; Cortegiani, A.; Raineri, S. M.; Giarratano, A. Bacterial Contamination of Inanimate Surfaces and Equipment in the Intensive Care Unit. *J. Intensive Care* **2015**, *3*, 1–8.

(24) Talaro, K. P.; Chess, D. Foundations in Microbiology. McGraw Hill Education: U.S.A., pp 1–242.

(25) Tortora. G. J.; Funke, B. R.; Case, C. L. Microbiology: An Introduction. Pearson: United States of America, pp 1–176.

(26) Meyers, A.; Furtmann, C.; Jose, J. Direct Optical Determination of Bacterial Cultures in Microplates for High-Troughput Screening Applications. *Enzyme Microbiol. Technol.* **2018**, *118*, 1–5.

(27) Gürsoy, M.; Harris, M. T.; Downing, J. O.; Barrientos-Palomo, S. N.; Carletto, A.; Yaprak, A. E.; Karaman, M.; Badyal, J. P. S. Bioinspired Fog Capture and Channel Mechanism Based on the Arid Climate Plant Salsola crassa. *Colloids Surf., A* **2017**, *529*, 195–202.

(28) Bot, C. T.; Prodan, C. Quantifying the Membrane Potential During *E. coli* Growth Stages. *Biophys. Chem.* **2010**, *146*, 133–137.

3. Atomised Spray Plasma Deposition of Bioinspired Hierarchical Superhydrophobic Nanocomposite Surfaces

3.1 Background and Introduction

Liquid repellent surfaces have attracted significant interest for societal and industrial applications, including: self-cleaning,[1] anti-icing,[2] anti-fogging,[3] building materials,[4] electronic devices,[5] antifouling,[6] anti-corrosion,[7] antibacterial,[8] drag reduction,[9] oil–water separation,[10,11] and anti-thrombotic surfaces.[12] One approach for attaining hydrophobicity is inspired by the water repellency properties of the lotus leaf (*Nelumbo nucifera*)—which contains microscale surface bumps (papillose epidermal cells) covered by nanoscale epicuticular waxes.[13] This hierarchical roughness reduces the solid–liquid contact line by increasing the liquid–air contact line due to entrapped air pockets at the composite solid–liquid–air interface, thereby facilitating the movement of droplets along the plant leaf surface leading to self-cleaning.[14]

A combination of such hierarchical roughness with low surface energy materials for the preparation of superhydrophobic surfaces has been reported in the past by fabrication methods such as: photopolymerisation,[1] electrodeposition,[15] hydrothermal process,[9] chemical vapour deposition,[16] plasma polymerisation,[17] sol-gel,[18] electrowetting,[19] layer-by-layer,[20,21] dip coating,[22] lithography,[23] fluorination,[24] and etching.[25] However, many of these techniques suffer from limitations, including: multi-step,[16,18,26] lengthy,[3] requiring high vapour pressure precursors,[27] post-heat treatments,[4] poor adhesion,[28] etc. Similarly, the superhydrophobic surfaces have been obtained by the atomisation of a hydrophobic-precursor–nanoparticle mixture into the plasma zone at atmospheric pressure.[29,30] However, it requires the use of carrier gas (e.g., helium, oxygen) to ignite the plasma and likely contamination of the internal electrodes. A summary of the previous superhydrophobic surfaces obtained by using the atomised spray plasma deposition technique is shown in Table 3.1.

In this chapter, we describe the single-step low-pressure atomised spray plasma deposition (ASPD) of liquid-repellent nanocomposite coatings obtained by using a low surface energy precursor–nanoparticle slurry

comprising perfluorotributylamine mixed with methacryloyl functionalised silica, zinc oxide, or graphene nanoparticles (which impart hierarchical roughness and mechanical hardness), Scheme 3.1.

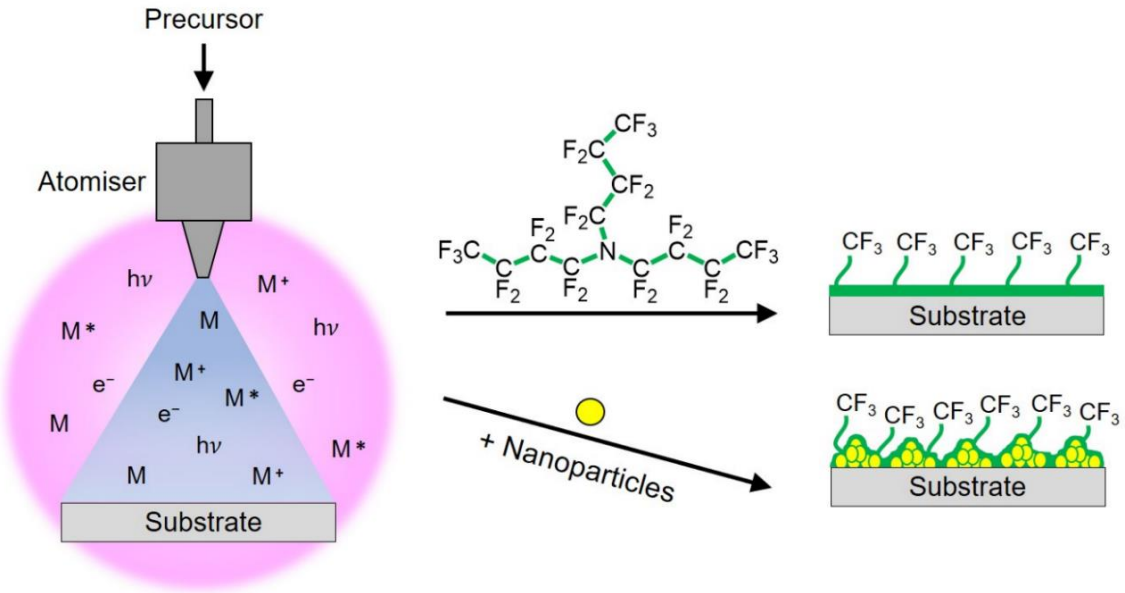

Scheme 3.1: Atomised spray plasma deposition (ASPD) of perfluorotributylamine–nanoparticle nanocomposite layer.

Table 3.1: State of the art of plasma polymer deposited by atomised spray plasma deposition (ASPD) indicating the water contact angle (WCA).

Precursors	ASPD Conditions	Applications	Ref.
Octane, octadiene, and ZnO nanoparticles	Atmospheric pressure	• Superhydrophobicity (WCA = 170°)	30
Octane and ZnO nanoparticles	Atmospheric pressure	• Superhydrophobicity • (WCA = 170°)	29
1H,1H,2H,2H-Perfluorooctyl acrylate	Low pressure	• Hydrophobicity (WCA = 128°) • Oleophobicity	31
Heptadecafluorodecyl acrylate	Atmospheric pressure	• Hydrophobicity • (WCA = 125°)	32
Dodecyl acrylate, 1,6-Hexanediol diacrylate, and 1,6-hexanediol Dimethacrylate	Atmospheric pressure	• Hydrophobicity • (WCA = 110°)	33
Perfluoroheptane	Atmospheric pressure	• Hydrophobicity • Oleophobicity	34

3.2 Results and Discussion

3.2.1 Atomised Spray Plasma Deposition

The atomised spray plasma deposition technique was used to deposit low-vapour-pressure precursors or slurries, as an alternative to gas-phase plasma polymerisation.[35–42] Perfluorotributylamine (+99.9%, Fluorinert FC-43, 3M Inc.) was mixed separately with a variety of nanoparticles: methacryloyl functionalised silica nanoparticles (12 nm primary particle size and 100–200 nm average aggregate size, Aerosil R711®, Evonik Industries AG); zinc oxide nanoparticles (<100 nm particle size, Sigma-Aldrich Ltd.); and graphene nanoplatelets (2–10 nm thickness and <2 µm particle diameter, Strem Chemicals UK Ltd.). Unfunctionalised silica nanoparticles display hydrophilic

behaviour due to surface hydroxyl groups and were found not to readily disperse in low surface tension liquids (e.g., perfluorotributylamine). Instead, methacryloyl functionalised SiO_2 nanoparticles (methacryloyl-SiO_2) were used due to their ease of dispersion in non-polar liquids.[43] Atomised spray plasma deposition was carried out using a 30 W continuous-wave plasma in conjunction with the atomisation at an optimum flow rate of 16 ± 4 x 10^{-4} mL s^{-1} (controlled by the delivery tube using a solid–liquid slurry) and 5.4 ± 0.02 x 10^{-4} mL s^{-1} (controlled by a high precision metering valve (Part No. 1335G2Y, Milli-Mite 1300 Series, HOKE Inc.) for perfluorotributylamine liquid precursor alone).

During the atomisation of the monomer precursor into the electrical discharge, the reactive species within the plasma (electrons, ions, vacuum UV photons) react with precursor molecule. Energetic electrons are responsible for the ionisation and fragmentation of the precursor molecule (bond energies: 3.1 eV for C–N, 3.6 eV for C–C, and 5.5 eV for C–F).[44,45,46] They activate the precursor–nanoparticle slurry droplets during impact onto the plasma-activated substrate leading to nanocomposite film growth. The polymer growth mechanism can be attributed to the ion bombardment leading to defluorination and activation of the perfluorocarbon plasma polymer growth. Therefore, it is suggested that the nanoparticles remained embedded within the plasma polymer matrix, improving the mechanical properties of the ASPD nanocomposite coatings.

3.2.2 Deposition Rate

Atomised spray deposition using perfluorotributylamine in the absence of plasma ignition resulted in negligible film growth rate (below 0.1 ± 0.1 nm min^{-1}), which means that the liquid precursor is effectively pumped away from the system. The optimal atomised spray plasma deposition (ASPD) rate for the perfluorotributylamine precursor was measured to be 49 ± 4 nm min^{-1} at a liquid flow rate of 5.4 ± 0.02 x 10^{-4} mL s^{-1} (using a high precision metering valve), Figure 3.1. This value is an order of magnitude greater than that reported for conventional vapour phase perfluorotributylamine plasma

deposition (5.9 nm min^{-1} growth rate[47])—which can be attributed to the higher precursor flow rate for atomised liquid droplets. The deposition rate of smooth ASPD perfluorotributylamine layers was measured by dividing the plasma polymer film thickness by the corresponding deposition time. The deposition rate varies with the flow rate whilst keeping the applied power constant during the atomised spray plasma deposition. At lower flow rates, there is a deficiency of monomer leading to significant fragmentation of the precursor molecules due to a higher proportion of energy per molecule. In contrast, at higher flow rates there is insufficient energy input leading to incomplete polymerisation.[48] This transition from the monomer-deficient regime to the energy-deficient regime for the deposition rate corresponds to the most favourable power to flow-rate ratio, W/F.[49]

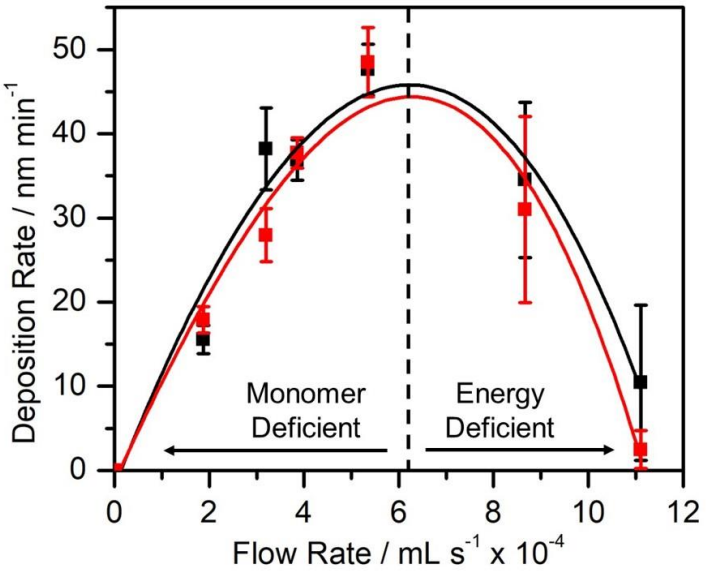

Figure 3.1: Deposition rate as a function of the flow rate of the ASPD of perfluorotributylamine layers deposited at a fixed power of 30 W: As-deposited (■); and rinsed with propan-2-ol/cyclohexane solvent mixture for 1 min (■). The dashed line indicates the transition from the monomer-deficient regime to the energy-deficient regime. 1:1 v/v propan-2-ol/cyclohexane solvent mixtures were used.

3.2.3 Contact Angle

The wettability of the optimal deposition rate of the ASPD perfluorotributylamine layer (water contact angle = 114 ± 1°) was found to be

comparable to its conventional vapour phase plasma deposited counterpart (water contact angle = 111° for coated flat substrate[50]), Figure 3.2. A level of oleophobicity was also measured (hexadecane contact angle = 65 ± 1°) which is consistent with the reported hexadecane contact angle value of 68° for C8-perfluoroalkyl chain (perfluorooctyl-trichlorosilane) self-assembled monolayers on flat silicon surfaces.[51] The low wettability of the ASPD perfluorotributylamine layer is attributed to its low surface energy, and thus, low polarisability of the C–F bonds within the perfluorinated polymer surface.[52] This lower wettability of the ASPD perfluorotributylamine layers can be achieved by introducing nanoparticles of different sizes and reinforcing the mechanical properties of the plasma polymer films.[53,54]

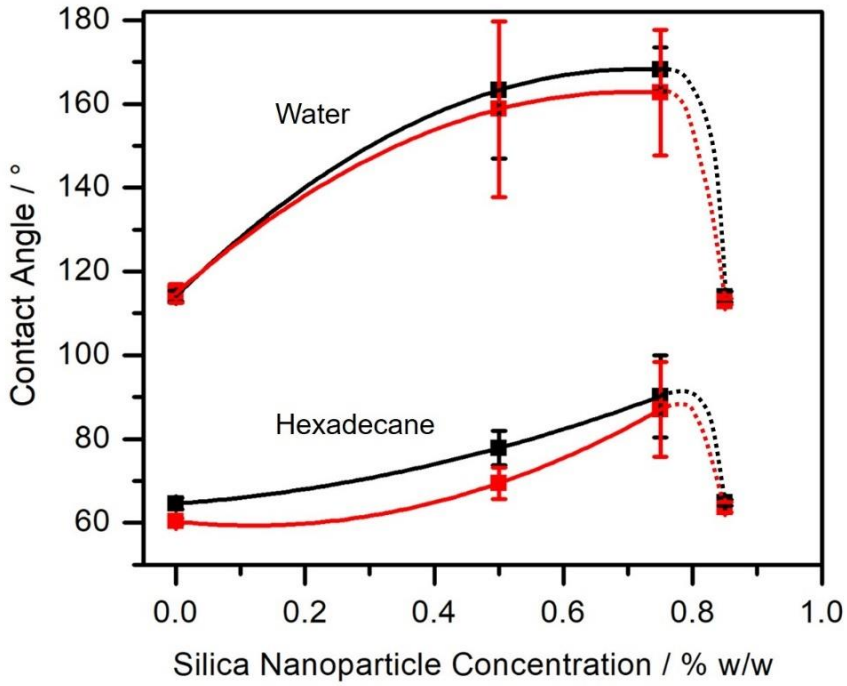

Figure 3.2: Water and hexadecane contact angles for ASPD perfluorotributylamine–methacryloyl-SiO_2 nanocomposite coatings: as-deposited (■); and following rinsing with 1:1 v/v propan-2-ol/cyclohexane solvent mixture for 1 min (■). The uncoated glass substrate has water and hexadecane contact angles of 21 ± 3° and 8 ± 3° respectively. Dashed lines indicate that slurry solution with nanoparticle concentration higher than 0.75% w/w become too viscous and make it unable for homogeneous atomisation.

Incorporation of methacryloyl-SiO_2 nanoparticles into the ASPD perfluorotributylamine layer led to a significant enhancement in liquid repellency yielding water and hexadecane contact angles as high as 168 ± 5° and 90 ± 10° respectively for an optimal precursor slurry loading of 0.75% w/w silica nanoparticles, Figure 3.2. This enhanced liquid repellency, of both water and hexadecane, may be attributed to the formation of air pockets trapped within the cavities of the polymer surface roughness increasing the air–solid interface—thus, reducing the liquid–solid interface—as described by the Cassie–Baxter Model.[14] On the other hand, nanoparticle concentrations exceeding 0.75% w/w, form a viscous nanoparticle slurry mixture, and thus it is unable to sustain homogeneous atomisation. By utilising reactive (methacryloyl) functionalised silica nanoparticles, greater bonding is promoted within the growing fluorocarbon polymer host matrix via plasma excitation. These liquid-repellent nanocoatings were stable towards washing with a 1:1 v/v propan-2-ol/cyclohexane polar/non-polar solvent mixture.

A variety of other nanoparticles was evaluated using this optimum nanoparticle concentration (0.75% w/w total). ASPD of perfluorotributylamine–(methacryloyl-SiO_2 + ZnO nanoparticles) significantly enhanced oil repellency further, achieving water and hexadecane contact angle values of 168 ± 1° and 110 ± 4°, respectively, Figure 3.3. These ASPD nanocomposite layers were stable towards polar/non-polar solvent rinsing. ASPD perfluorotributylamine–graphene layers displayed water contact angle values of 170 ± 1°, and 165 ± 13° for as-deposited and solvent-rinsed layers respectively. In the case of ASPD perfluorotributylamine–(methacryloyl-SiO_2 + graphene) nanocomposite layers, the water contact angle dropped from 170° to ~130° following solvent rinsing, Figure 3.3. The hexadecane contact angle values reported in this work are low in comparison with other works reporting superoleophobic surfaces.[55] This is because the ASPD depositions using the solution in question are limited to precursor slurry loadings up to 0.75% w/w, and thus, limiting the roughness degree induced on the surface. Overall, the ASPD perfluorotributylamine–(methacryloyl-SiO_2 + ZnO) nanocomposite layers displayed the highest liquid repellency towards water and oil (hexadecane). This may be attributed to a better dispersion of perfluotributylamine with the

(methacryloyl-SiO_2 + ZnO) nanoparticle slurry mixture using the trifluoracetic acid fluorosurfactant yielding a more homogeneous hierarchical roughness.

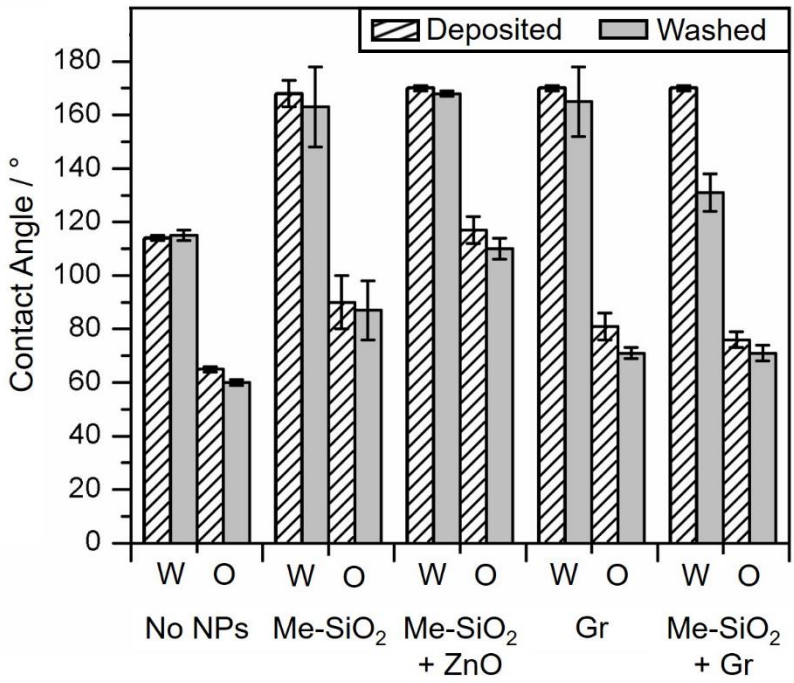

Figure 3.3: Water (W) and hexadecane (O) contact angle values for ASPD perfluorotributylamine–nanoparticle composite layers: as-deposited, and rinsed for 1 min with 1:1 v/v propan-2-ol/cyclohexane solvent mixture. Using 0.75% w/w total nanoparticle slurry loading: methacryloyl-SiO_2 nanoparticles; methacryloyl-SiO_2 + ZnO nanoparticles (1:1 w/w); graphene; and methacryloyl-SiO_2 + graphene nanoparticles (1:1 w/w).

3.2.4 X-ray Photoelectron Spectroscopy

XPS analysis of the ASPD perfluorotributylamine layer detected the presence of only carbon, fluorine, and nitrogen, Table 3.2. The absence of any Si(2p) and O(1s) XPS signals confirmed pin-hole free coverage of the deposited layer over the underlying silicon substrate. For the case of ASPD perfluorotributylamine–methacryloyl-SiO_2 nanocomposite and perfluorotributylamine–(methacryloyl-SiO_2 + ZnO) nanocomposite layers, less than 0.2 at.% of nanoparticles (silicon or zinc XPS signal) and a small amount of oxygen were detected, which confirms that the nanoparticles remain encapsulated within perfluorotributylamine–nanoparticle slurry droplets during atomised spray plasma deposition (0.2–5 nm XPS sampling depth[56]).

Table 3.2: XPS compositions for precursor (theoretical) and ASPD perfluorotributylamine–nanoparticle layers.

ASPD Perfluorotributylamine Layer System	Atomic Composition / %						F:C Ratio	C(1s) Component / %				
	C	F	N	O	Si	Zn		–<u>C</u>–CF_n	–<u>C</u>F–	–<u>C</u>F–CF_n	–<u>C</u>F_2–	–<u>C</u>F_3
Theoretical	30	67.5	2.5	NA	NA	NA	2.25	NA	NA	NA	75	25
No Nanoparticle	34.9 ± 0.2	58.2 ± 0.0	6.9 ± 0.2	0.0 ± 0.0	NA	NA	1.7 ± 0.0	7.3 ± 1.8	11.0 ± 0.0	16.7 ± 0.2	36.9 ± 1.1	28.1 ± 0.9
SiO_2	33.8 ± 0.1	58.5 ± 0.3	6.9 ± 0.1	0.6 ± 0.1	0.1 ± 0.2	NA	1.7 ± 0.1	7.6 ± 0.4	13.4 ± 0.1	14.9 ± 0.5	35.9 ± 1.6	28.2 ± 1.4
SiO_2 + ZnO	34.4 ± 0.2	57.1 ± 0.3	7.1 ± 0.1	1.2 ± 0.4	0.0 ± 0.0	0.2 ± 0.0	1.7 ± 0.0	8.4 ± 1.0	11.1 ± 1.1	15.0 ± 0.8	37.1 ± 2.7	28.3 ± 1.5

The C(1s) XPS spectra of ASPD perfluorotributylamine (and nanocomposite) layers were fitted to five Gaussian Mg $K\alpha_{1,2}$ components in conjunction with their corresponding Mg $K\alpha_3$, and Mg $K\alpha_4$ satellite peaks shifted towards lower binding energies by ~8.4 and ~10.2 eV respectively, Figure 3.4.[57] The C(1s) Mg $K\alpha_{1,2}$ components being: –<u>C</u>–CF_n at 286.1 eV, –<u>C</u>F– at 287.5 eV, –<u>C</u>F–CF_n at 289.2 eV, –<u>C</u>F_2– at 291.2 eV, and –<u>C</u>F_3 at 293.1 eV.[8,9,58] Unsaturated and crosslinked carbon centres (defined as %[–<u>C</u>F–CF_n] + %[–<u>C</u>F–] + %[–<u>C</u>–CF_n]) account for ~35% of the total atomic carbon composition in all of the ASPD perfluorotributylamine–nanocomposite layers (which is consistent with the measured decrease in F:C ratio compared to the precursor theoretical value), Table 3.2. Therefore, there was no significant variability in the chemical composition or F:C ratio between the various ASPD perfluorotributylamine–nanocomposite layers.

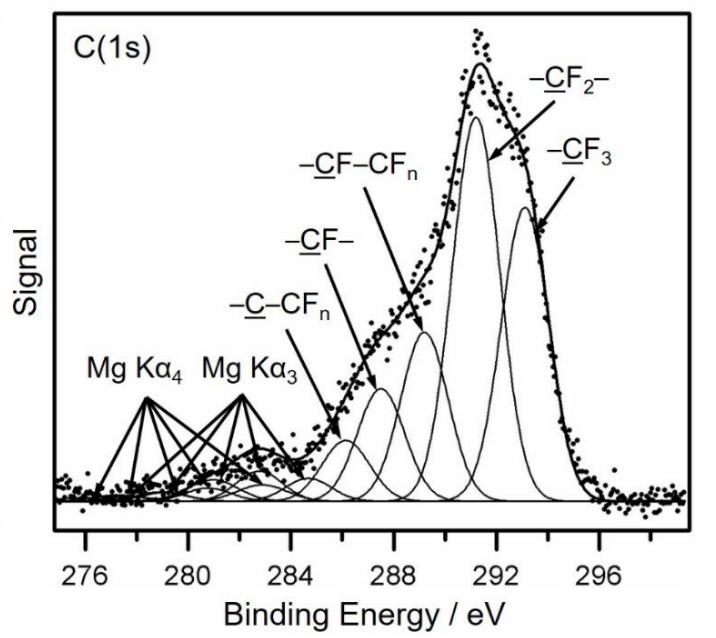

Figure 3.4: C(1s) XPS spectrum of ASPD perfluorotributylamine layer. Mg $K\alpha_3$ and Mg $K\alpha_4$ satellite components are also shown.[59]

The single N(1s) and F(1s) Mg $K\alpha_{1,2}$ peaks measured at 400.8 eV and 687.9 eV correspond to covalently bonded nitrogen and fluorine atoms respectively,[58,60] Figure 3.5.

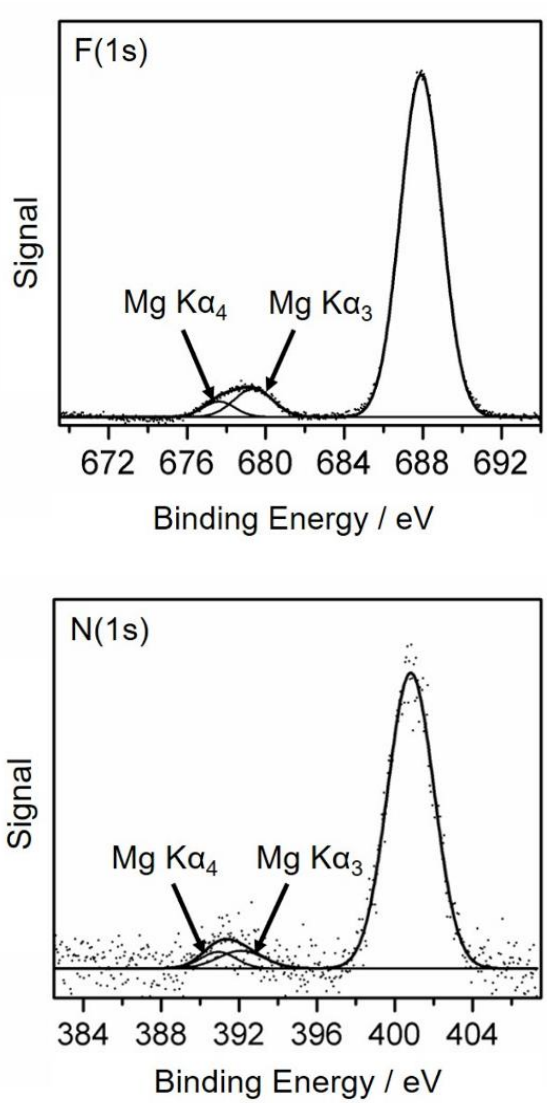

Figure 3.5: Top: F(1s); and bottom: N(1s) XPS spectra of ASPD perfluorotributylamine layer. No significant variability of XPS spectra for the ASPD perfluorotributylamine–nanocomposite layers were found.

The XPS elemental composition N:C:F ratio of 1.0:5.1:8.4 for the ASPD perfluorotributylamine layer can be correlated to the characteristic low energy electron-impact fragmentation molecular ion formed from perfluorotributylamine in the gas phase: $C_5F_{10}N^+$ (m/z of 264) with a molecular structure of $CF_3CF_2CF_2CF{=}N^+{=}CF_2$ (N:C:F ratio of 1:5:10), Table 3.2.[61,62] This is consistent with the high level of nitrogen atom incorporation measured by XPS (6.9 at.% compared to the precursor theoretical value of 2.5 at.%, Table 3.2).

3.2.5 Infrared Spectroscopy

The infrared spectrum obtained for the ASPD perfluorotributylamine layer displayed a broad band comprising perfluorinated chain $–CF_2–CF_3$ (1365–1325 cm^{-1}), $–CF_3$ (1350–1120 cm^{-1}), and $–CF_2–$ (1280–1120 cm^{-1}) absorbances, as well as –C–N (1250–1020 cm^{-1}), Figure 3.6 and Table 3.3.[50,68] The observed shift of this broad peak (1365–1120 cm^{-1}) towards higher wavenumber with respect to the perfluorotributylamine precursor can be attributed to defluorination and crosslinking of the perfluoroalkyl chains during plasma-assisted deposition[63]—which is consistent with the decrease of F:C XPS ratio measured for the ASPD perfluorotributylamine layer, Table 3.2. The band at 1731 cm^{-1} can be attributed to –CF=CF– stretching (not carbonyl stretching given the absence of any oxygen detected by XPS, Table 3.2[64]).[65,66] The characteristic perfluoroalkyl chain and the –CF=CF– infrared bands are also evident in the infrared spectra of the ASPD perfluorotributylamine–methacryloyl-SiO_2 nanocomposite and perfluorotributylamine–(methacryloyl-SiO_2 + ZnO) nanocomposite layers, Figure 3.6.

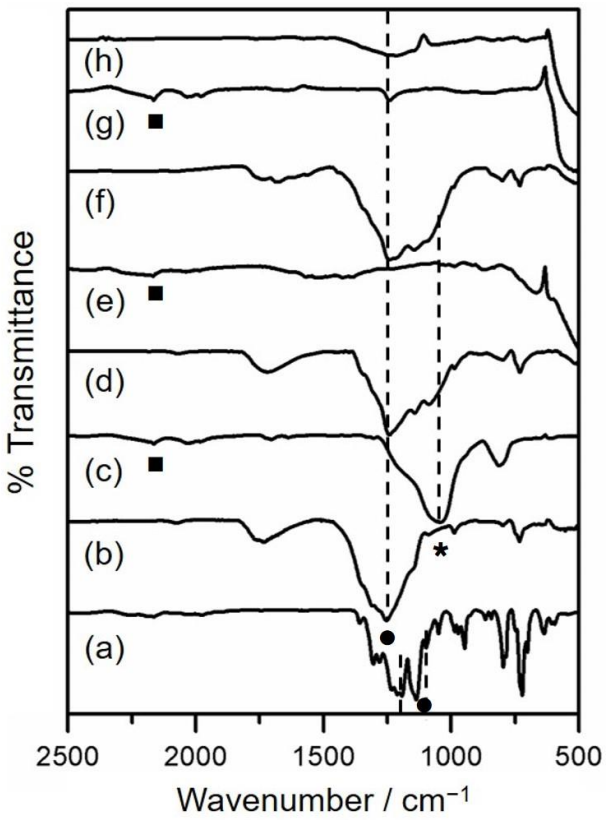

Figure 3.6: Infrared spectra: (a) ATR perfluorotributylamine precursor; (b) RAIRS ASPD perfluorotributylamine layer; (c) ATR methacryloyl-SiO_2 nanoparticles; (d) RAIRS ASPD perfluorotributylamine–methacryloyl-SiO_2 nanocomposite layer (0.75% w/w nanoparticle concentration); (e) ATR ZnO nanoparticles; (f) RAIRS ASPD perfluorotributylamine–(methacryloyl-SiO_2 + ZnO) nanocomposite layer (0.75% w/w total nanoparticle concentration); (g) ATR graphene nanoplatelets; and (h) RAIRS ASPD perfluorotributylamine–graphene nanocomposite layer (0.75% w/w graphene concentration). ● indicates perfluorinated chain (1365–1120 cm^{-1}), and ✱ indicates Si–O–Si (1049 cm^{-1}) absorbances. ■ indicates weak features in the 2160–2030 cm^{-1} range originated from the diamond substrate in the ATR cell.[67]

Table 3.3: Infrared assignments for perfluorotributylamine precursor and ASPD nanocomposite layers.[68,69,70,71]

Absorption Frequency / cm^{-1}	**Assignment**
1731	–CF=CF– stretching
1365–1325	$–CF_2–CF_3$ stretching
1350–1120	$–CF_3$ antisymmetric stretching
1280–1120	$–CF_2–$ stretching
1250–1020	C–N antisymmetric stretching
1100–1000	Si–O–Si stretching
1100–900	C–F stretching
980	$–CF_3$ symmetric stretching
815	Si–O–Si bending
605–505	Zn–O stretching

Overall, it is evident that there is nanoparticle incorporation within the bulk of all the ASPD perfluorotributylamine–nanocomposite layers (sampling depth of 0.5–20 μm for RAIRS[72]). Infrared spectra of methacryloyl-SiO_2 nanoparticles display a band shoulder in the 1100–1000 cm^{-1} region associated with Si–O–Si stretching.[73,74] The presence of this feature confirmed the incorporation of methacryloyl-SiO_2 nanoparticles into the ASPD perfluorotributylamine nanocomposite layers.[75,76]

ZnO nanoparticles exhibit a strong infrared band at 605–505 cm^{-1} assigned to the stretching mode of Zn–O.[71] This was also observed for the ASPD perfluorotributylamine–(methacryloyl-SiO_2 + ZnO) nanocomposite layer in combination with the aforementioned methacryloyl-SiO_2 nanoparticle band shoulder feature at 1100–1000 cm^{-1}.

The ASPD perfluorotributylamine–graphene nanocomposite layer displayed a strong characteristic graphene infrared absorbance feature in the 600–450 cm^{-1} region.

3.2.6 Scanning Electron Microscopy

Scanning electron microscopy (SEM) images of ASPD perfluorotributylamine layers showed a flat surface morphology indicating the deposition of a smooth nanocoating, Figure 3.7.

Incorporation of the various types of nanoparticles gave rise to hierarchical topographical structures. ASPD perfluorotributylamine–methacryloyl-SiO_2 nanocomposite layers present dispersed 3-level hierarchical roughness islands comprising a background nanoscale roughness superimposed onto microscale, spherical asperities and larger cavities (ca. 12 μm diameter)—which correlate to the enhancement in water and hexadecane contact angle values, Figure 3.2. A mixture of methacryloyl-SiO_2 and ZnO nanoparticles in the ASPD nanocomposite layers also resulted in hierarchical roughness but yielded a more evenly distributed hierarchical surface structure (no large-scale cavities which manifest in higher hexadecane contact angle values)—this may arise due to a better-dispersed perfluorotributylamine / (methacryloyl-SiO_2 + ZnO) nanoparticle slurry mixture through the use of trifluoroacetic acid fluorosurfactant, Figure 3.3. Such hierarchical roughness lowers liquid–solid interaction due to air pockets in accordance with the Cassie–Baxter model for surface wetting.[14]

ASPD nanocomposite layers containing graphene lacked significant nanoscale structure. They presented a more globular microscale roughness (presumably due to the larger platelet size of graphene), and consequently displays the lowest hexadecane contact angle values among the range of ASPD nanocomposite layers, Figure 3.3.

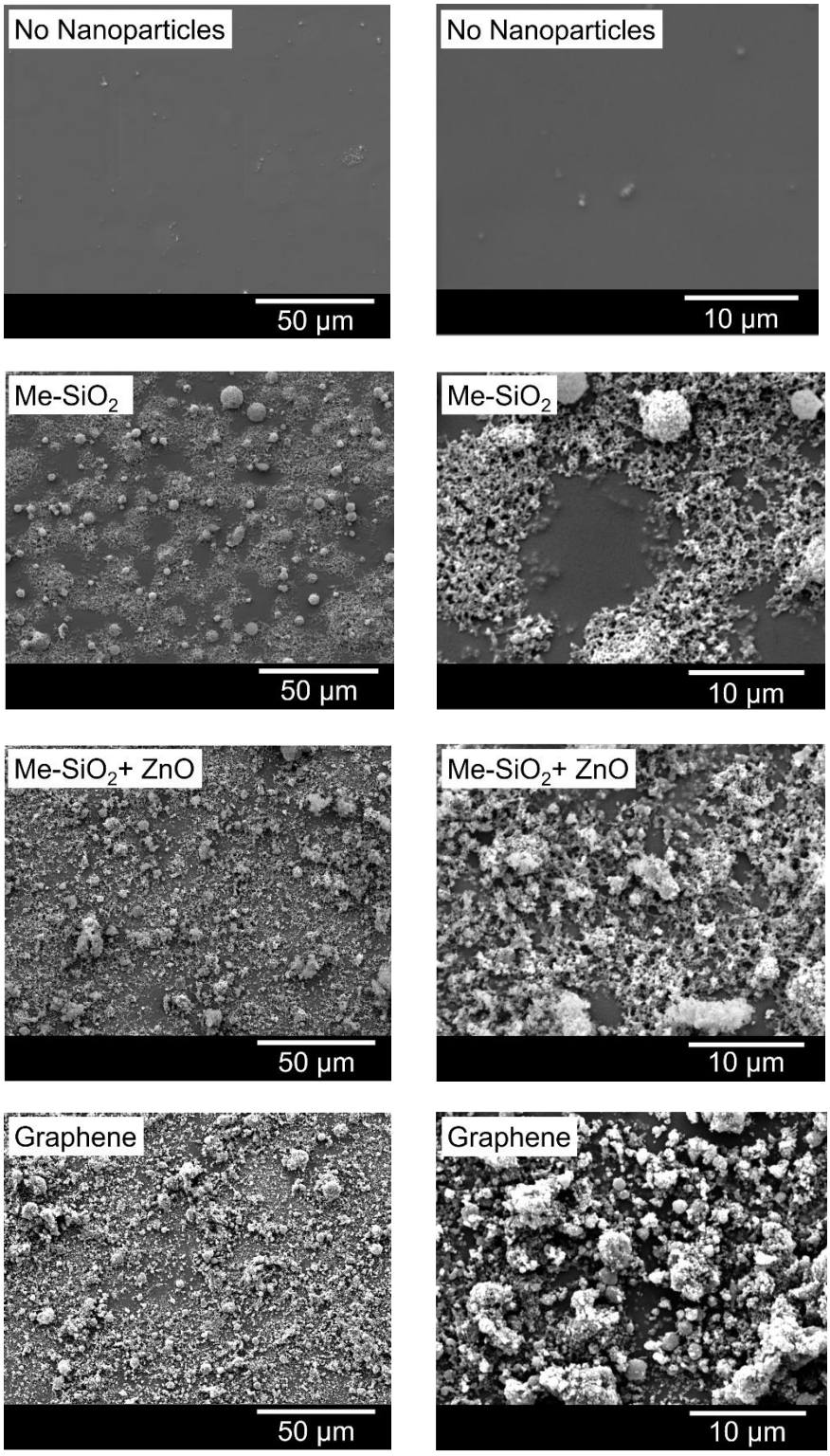

Figure 3.7: SEM images of ASPD perfluorotributylamine nanocomposite layers containing different types of nanoparticles.

3.2.7 Microindentation

Microindentation measurements showed that nanoparticle incorporation significantly improves the hardness of ASPD nanocomposite layers. Also, they displayed scratch-resistance (no microindentation) at applied loads below 245 mN, Figure 3.8. In all cases, the hardness improved by at least two-fold. Microindentation Vickers hardness of the ASPD perfluorotributylamine–(methacryloyl-SiO_2 + ZnO) nanocomposite layers was found to be as hard as the layers containing just methacryloyl-SiO_2 nanoparticles. ASPD perfluorotributylamine–graphene nanocomposite layers further enhanced the hardness value (10.7 ± 0.8 GPa at an applied force of 980 mN). ASPD perfluorotributylamine–(methacryloyl-SiO_2 + graphene) nanocomposite layers presented the highest hardness values that may be attributed to the mechanical properties of graphene (elastic module of ~1 TPa),[77] which are reported to reinforce the mechanical properties of polymer nanocomposites.[78]

For comparable applied loads (980 mN), the ASPD perfluorotributylamine–graphene nanocomposite layer displays hardness values exceeding stainless steel (10.7 GPa versus 1–2 GPa, respectively).[79]

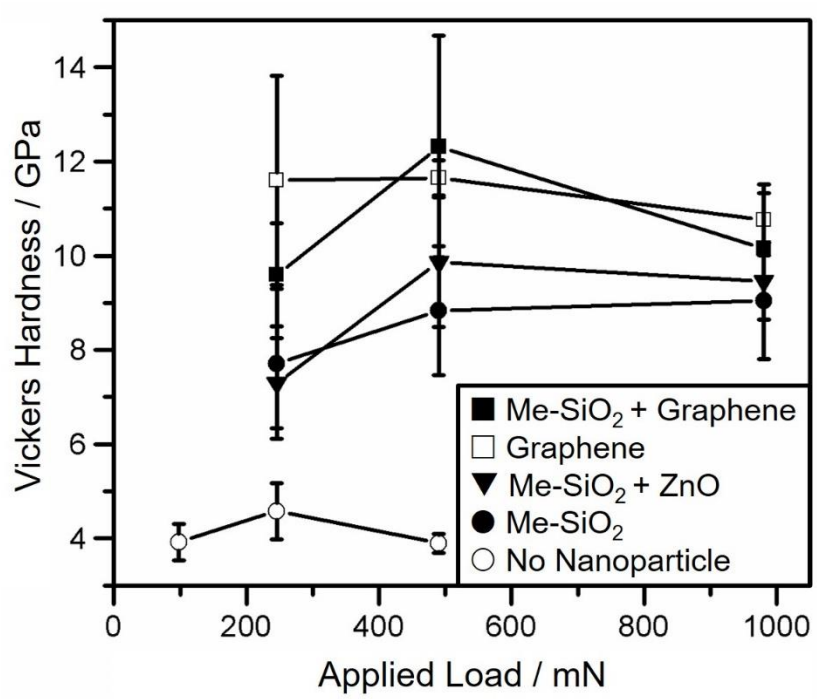

Figure 3.8: Microindentation Vickers hardness as a function of applied loads for ASPD nanocomposite layers (0.75% w/w total nanoparticle concentration) for: (methacryloyl-SiO_2 + graphene), graphene, (methacryloyl-SiO_2 + ZnO), and methacryloyl-SiO_2 nanoparticle slurry mixtures. Microindentation below 245 mN load for the nanocomposite coatings resulted in no visible indentation (scratch-resistance). The Vickers hardness of reference 316 stainless steel was measured to be 1.9 ± 0.3 GPa.

3.3 Conclusions

Atomisation of fluorocarbon precursor-nanoparticle slurries into a low temperature non-equilbrium electric discharge leads to the deposition to liquid repellent nanocomposite coatings. All nanocomposite coatings displayed high water repellency of ~168°, whereas the ASPD perfluorotributylamine–(methacryloyl-SiO_2 + ZnO) nanocomposite layers displayed the highest oil repellency of ~110°, However, in this work, the oil repellency of the ASPD nanocomposite coatings is limited by their roughness degree, and consequently, to the maximum precursor slurry concentration which is a key parameter to increase surface roughness and oil repellency, as compared to other works reporting oil contact angle values greater than 150°. SEM images showed that the ASPD perfluorotributylamine–(methacryloyl-SiO_2 + ZnO) nanocomposite layers are more homogeneous due to the effect of the perfluorosurfactant which enhances the dispersion of the

perfluorotributylamine–nanoparticle slurry mixture during the atomisation. Additionally, the incorporation of nanoparticles for the ASPD nanocomposite coatings enhanced their mechanical properties, Figure 3.8. The ASPD nanocomposite coatings, reinforced with graphene, displayed the highest Vickers hardness values or plastic deformation resistance which is attributed to the excellent mechanical properties of graphene.

Overall, ASPD perfluorotributylamine–(methacryloyl-SiO_2 + ZnO) nanocomposite layers displayed the highest contact angle values against water and oil. Therefore, these substrate-independent ASPD nanocomposite coatings may find use in water-repellent and self-cleaning applications on different material surfaces.

3.4 References

(1) Liu, Y.; Wang, Q.; Zhu, X.; Yang, F.; Akram, M. Y.; Nie, J. Preparation of Superhydrophobic Surface via One-Step Photopolymerization. *Mater. Lett.* **2017**, *190*, 48–51.

(2) Chu, F.; Wu, X.; Wang, L. Meltwater Evolution during Defrosting on Superhydrophobic Surfaces. *ACS Appl. Mater. Interfaces* **2018**, *10*, 1415–1421.

(3) Ruiz-Cabello, F. J. M.; Ibáñez-Ibáñez, P. F.; Gómez-Lopera, J. F.; Martínez-Aroza, J.; Cabrerizo-Vílchez, M.; Rodríguez-Valverde, M. A. Testing the Performance of Superhydrophobic Aluminum Surfaces. *J. Colloid Interf. Sci.* **2017**, *508*, 129–136.

(4) Zulfiqar, U.; Awais, M.; Hussain, S. Z.; Hussain, I.; Husain, S. W.; Subhani, T. Durable and Self-Healing Superhydrophobic Surfaces for Building Materials. *Mater. Lett.* **2017**, *192*, 56–59.

(5) Li, B.; Wang, X.; Jung, H. Y.; Kim, Y. L.; Robinson, J. T.; Zalalutdinov, M.; Hong, S.; Hao, J.; Ajayan, P. M.; Wan, K.-T.; Jung, Y.-J. Printing Highly Controlled Suspended Carbon Nanotube Network on Micro-Patterned Superhydrophobic Flexible Surface. *Sci. Rep.* **2015**, *5*, 1–9.

(6) Li, H.; Yu, S. A Robust Superhydrophobic Surface and Origins of Its Self-Cleaning Properties. *Appl. Surf. Sci.* **2017**, *420*, 336–345.

(7) Qian, H.; Li, M.; Li, Z.; Lou, Y.; Huang, L.; Zhang, D.; Xu, D.; Du, C.; Lu, L.; Gao, J. Mussel-Inspired Superhydrophobic Surfaces with Enhanced Corrosion Resistance and Dual-Action Antibacterial Properties. *Mater. Sci. Eng.* **2017**, *80*, 566–577.

(8) Werb, M.; García, C. F.; Bach, N. C.; Grumbein, S.; Sieber, S. A.; Opitz, M.; Lieleg, O. Surface Topology Affects Wetting Behavior of *Bacillus subtilis* Biofilms. *NPJ Biofilms Microbiomes* **2017**, *3*, 1–11.

(9) Cheng, M.; Zhang, S.; Dong, H.; Han, S.; Wei, H.; Shi, F. Improving the Durability of a Drag-Reducing Nanocoating by Enhancing Its Mechanical Stability. *ACS Appl. Mater. Interfaces* **2015**, *7*, 4275–4282.

(10) Su, X.; Li, H.; Lai, X.; Zhang, L.; Liang, T.; Feng, Y.; Zeng, X. Polydimethylsiloxane-Based Superhydrophobic Surfaces on Steel Substrate: Fabrication, Reversibly Extreme Wettability and Oil–Water Separation. *ACS Appl. Mater. Interfaces* **2017**, *9*, 3131–3141.

(11) Brown, P. S.; Atkinson, O. D. L. A.; Badyal, J. P. S. Ultrafast Oleophobic–Hydrophilic Switching Surfaces for Antifogging, Self-Cleaning, and Oil–Water Separation. *ACS Appl. Mater. Interfaces* **2014**, *6*, 7504–7511.

(12) Hoshian, S.; Kankuri, E.; Ras, R. H. A.; Franssila, S.; Jokinen, V. Water and Blood Repellent Flexible Tubes. *Sci. Rep.* **2017**, *7*, 1–8.

(13) Barthlott, W.; Neinhuis, C. Purity of the Sacred Lotus, or Escape from Contamination in Biological Surfaces. *Planta* **1997**, *202*, 1–8.

(14) Cassie, A. B. D.; Baxter, S. Wettability of Porous Surfaces. *T. Faraday Soc.* **1944**, *40*, 546–551.

(15) Liu, Q.; Chen, D.; Kang, Z. One-Step Electrodeposition Process to Fabricate Corrosion-Resistant Superhydrophobic Surface on Magnesium Alloy. *ACS Appl. Mater. Interfaces* **2015**, *7*, 1859–1867.

(16) Yokoi, N.; Manabe, K.; Tenjimbayashi, M.; Shiratori, S. Optically Transparent Superhydrophobic Surfaces with Enhanced Mechanical Abrasion Resistance Enabled by Mesh Structure. *ACS Appl. Mater. Interfaces* **2015**, *7*, 4809–4816.

(17) Chen, W.; Fadeev, A. Y.; Hsieh, M. C.; Öner, D.; Youngblood, J.; McCarthy, T. J. Ultrahydrophobic and Ultralyophobic Surfaces: Some Comments and Examples. *Langmuir* **1999**, *15*, 3395–3399.

(18) Järn, M.; Heikkilä, M.; Lindén, M. Bioinspired Synthesis of Superhydrophobic Coatings. *Langmuir* **2008**, *24*, 10625–10628.

(19) Lapierre, F.; Coffinier, Y.; Boukherroub, R.; Thomy, V. Electro-(de)wetting on Superhydrophobic Surfaces. *Langmuir* **2013**, *29*, 13346–13351.

(20) Brown, P. S.; Bhushan, B. Mechanically Durable, Superomniphobic Coatings Prepared by Layer-by-Layer Technique for Self-Cleaning and Anti-Smudge. *J. Colloid Interf. Sci.* **2015**, *456*, 210–218.

(21) Syed, J. A.; Tang, S.; Meng, X. Super-Hydrophobic Multilayer Coatings with Layer Number Tuned Swapping in Surface Wettability and Redox Catalytic Anti-Corrosion Application. *Sci. Rep.* **2017**, *7,* 1–17.

(22) Wang, Y.; Shi, Y.; Pan, L.; Yang, M.; Peng, L.; Zong, S.; Shi, Y.; Yu, G. Multifunctional Superhydrophobic Surfaces Templated from Innately Microstructured Hydrogel Matrix. *Nano Lett.* **2014**, *14*, 4803–4809.

(23) Wu, D.; Wu, S.-Z.; Chen, Q.-D.; Zhang, Y.-L.; Yao, J.; Yao, X.; Niu, L.-G.; Wang, J.-N.; Jiang, L.; Sun, H.-B. Curvature-Driven Reversible in Situ Switching Between Pinned and Roll-Down Superhydrophobic States for Water Droplet Transportation. *Adv. Mater.* **2011**, *23*, 545–549.

(24) Brown, P. S.; Talbot, E. L.; Wood, T. J.; Bain, C. D.; Badyal, J. P. S. Superhydrophobic Hierarchical Honeycomb Surfaces. *Langmuir* **2012**, *28*, 13712–13719.

(25) Ryu, J.; Kim, K.; Park, J.; Hwang, B. G.; Ko, Y.; Kim, H.; Han, J.; Seo, E.; Park, Y.; Lee, S. J. Nearly Perfect Durable Superhydrophobic Surfaces Fabricated by a Simple One-Step Plasma Treatment. *Sci. Rep.* **2017**, *7*, 1–8.

(26) Abolghasemibizaki, M.; Mohammadi, R. Droplet Impact on Superhydrophobic Surfaces Fully Decorated with Cylindrical Macrotextures. *J. Colloid Interf. Sci.* **2018**, *509*, 422–431.

(27) Bonnar, M. P.; Burnside, B. M.; Christie, J.; Sceal, E. J.; Troupe, C. E.; Wilson, J. I. Hydrophobic Coatings from Plasma Polymerized Vinyltrimethylsilane. *Chem. Vap. Deposition* **1999**, *5*, 117–125.

(28) Li, Y.; Shao, H.; Lv, P.; Tang, C.; He, Z.; Zhou, Y.; Shuai, M.; Mei, J.; Lau, W.-M. Fast Preparation of Mechanically Stable Superhydrophobic Surface by UV Cross-Linking of Coating onto Oxygen-Inhibited Layer of Substrate. *Chem. Eng. J.* **2018**, *338*, 440–449.

(29) Fanelli, F.; Mastrangelo, A. M.; Fracassi, F. Aerosol-Assisted Atmospheric Cold Plasma Deposition and Characterization of Superhydrophobic Organic-Inorganic Nanocomposite Thin Films. *Langmuir* **2014**, *30*, 857–865.

(30) Fanelli, F.; Mastrangelo, A. M. Caputo, G.; Fracassi, F. Tuning the Structure and Wetting Properties of Organic-Inorganic Nanocomposite Coatings Prepared by Aerosol-Assisted Atmospheric Pressure Cold Plasma Deposition. *Surf. Sci. Technol.* **2019**, *358*, 67–75.

(31) Ward, L. Application of a Coating Forming Material onto at Least One Substrate. U.S. patent WO 2003101621 A2, Dec 11, 2003.

(32) O'Neill, L.; O'Sullivan, C. Polymeric Coating Deposited from an Aerosol-Assisted Non-Thermal Plasma Jet. *Chem. Vap. Depos.* **2009**, *15*, 21–26.

(33) Bardon, J.; Martin, A.; Fioux, P.; Amari, T.; Mertz, G.; Delmee, M.; Roucoules, V.; Reinforcement of a Dodecylacrylate Plasma Polymer by Admixture of a Diacrylate or a Dimethacrylate Cross-Linker. *Plasma Process Polym.* **2018**, *15*, e1800031.

(34) Jiang, X.; Chen, G.; Rui, Y.; Liu, K. Modification of Silk Fabric via Atmospheric Pressure Plasma Liquid Deposition. *J. Text. Res.*, **2009**, *11*, 020.

(35) Ward, L. J.; Schofield, W. C. E.; Badyal, J. P. S. Atmospheric Pressure Plasma Deposition of Structurally Well-Defined Polyacrylic Acid Films. *Chem. Mater.* **2003**, 15, 1466–1469.

(36) Wood, T. J.; Brown, P. S.; Badyal, J. P. S. Atomized Spray Plasma Deposition of Structurally Well-Defined Bioactive Coatings. *Plasma Chem. Plasma Process*. **2014**, *34*, 1019–1031.

(37) Vangeneugden, D.; Paulussen, S.; Goosens, O.; Rego, R.; Rose, K. Aerosol-Assisted Plasma Deposition of Barrier Coatings Using Organic-Inorganic Sol-Gel Precursor Systems. *Chem. Vap. Deposition* **2005**, *11*, 491–496.

(38) Fanelli, F.; Mastrangelo, A. M.; Fracassi, F. Aerosol-Assisted Atmospheric Cold Plasma Deposition and Characterization of Superhydrophobic Organic-Inorganic Nanocomposite Thin Films. *Langmuir* **2014**, *30*, 857–865.

(39) Jiang, X.; Chen, G.; Rui, Y.; Liu, K. Modification of Silk Fabric via Atmospheric Pressure Plasma Liquid Deposition. *J. Text. Res.*, **2009**, *11*, 020.

(40) Badyal, J. P. S.; Ward, L.; York, D. W.; Brooker, A. T.; Summers, S.; Crowther, M.; Roberts, N. P. S.; Yates, A. T.; Datta, S. Fibrous Products and Methods of Making and Using Them. World Patent WO2005028741 A1, May 31, 2005.

(41) Fanelli, F.; Mastrangelo, A. M. Caputo, G.; Fracassi, F. Tuning the Structure and Wetting Properties of Organic-Inorganic Nanocomposite Coatings Prepared by Aerosol-Assisted Atmospheric Pressure Cold Plasma Deposition. *Surf. Sci. Technol.* **2019**, *358*, 67–75.

(42) Bardon, J.; Martin, A.; Fioux, P.; Amari, T.; Mertz, G.; Delmee, M.; Roucoules, V.; Reinforcement of a Dodecylacrylate Plasma Polymer by Admixture of a Diacrylate or a Dimethacrylate Cross-Linker. *Plasma Process Polym.* **2018**, *15*, e1800031.

(43) Sadej, M.; Gojzewski, H.; Andrzejewska, E. Photocurable Polymethacrylate-Silica Nanocomposites: Correlation Between Dispersion Stability, Curing Kinetics, Morphology and Properties. *J. Polym. Res.* **2016**, *23*, 116–127.

(44) d' Agostino R. Plasma Deposition, Treatment, and Etching of Polymers. Academic Press, Inc.: San Diego CA, 1990.

(45) Biederman, H. *Plasma Polymer Films*; Imperial College Press: London, 2004; pp 13–52.

(46) Kita, H.; Shigekuni, M.; Tanaka, Okamoto, K.-I.; Kawafune, I. Plasma Polymerization of Perfluoroalkanes over Zeolite Membrane and the Gas Permeability of the Membrane. *J. Photopolym. Sci. Technol.* **1995**, *8*, 385–392.

(47) Yang, M. R.; Chen, K. S.; He, J. L. The Interaction Between Blood and the Surface Characteristics of Plasma Polymerized Films. *Mater. Chem. Phys.* **1997**, *48*, 71–75.

(48) Gilliam, M. A.; Yu, Q.; Yasuda, H. Plasma Polymerization Behavior of Fluorocarbon Monomers in Low-Pressure AF and RF Discharges. *Plasma Process Polym.* **2007**, *4*, 165-172.

(49) Yasuda, H. K. *Plasma Polymerization*; Academic Press: London, U.K., 1985.

(50) Reniers, F.; Vandencasteele, N.; Bury, O. Method for Depositing a Fluorinated Layer from a Precursor Monomer. U.S. Patent US2011/0014395 A1, Jan 20, 2011.

(51) Aulin, C.; Yun, S. H.; Wagberg, L.; Lindstrom, T. Design of Highly Oleophobic Cellulose Surfaces from Structured Silicon Templates. *ACS Appl. Mater. Interfaces* **2009**, *1*, 2443–2452.

(52) Posner, S. Perfluorinated Compounds: Occurrence and Uses in Products. In *Polyfluorinated Chemicals and Transformation Products*; Knepper, T. P.; Lange, F. T., Eds.; Springer: Heidelberg, 2012, pp 25–41.

(53) Yang, J.; Zhao, J. Preparation and Mechanical Properties of Silica Nanoparticles Reinforced Composite Hydrogels. *Mater. Lett.* **2014**, *120*, 36–38.

(54) Rodríguez-Tobías, H.; Morales, G.; Rodríguez-Fernández, O.; Acuña, P. Effect of Zinc Oxide Nanoparticles Concentration on the Mechanical Properties and UV Protection of In Situ Synthesized ABS Based Nanocomposites. *Macromol. Sy.* **2013**, *325–326* (1), 147–155.

(55) Brown, P. S:; Bhushan, B. Designing Bioinspired Superoleophobic Surfaces. *Appl. Mater.* **2016**, *4*, 015703.

(56) Briggs D. *Surface Analysis of Polymers by XPS and Static SIMS*, Cambridge University Press, 1998; pp 34–39.

(57) Hofmann, S. Instrumentation. *Auger- and X-Ray Photoelectron Spectroscopy in Materials Science. A User-Oriented Guide*; Springer Series in Surface Science 49; Springer-Verlag: Berlin, 2013; pp 18–19.

(58) Beamson, G.; Briggs, D. *High-Resolution XPS of Organic Polymers. The Scienta ESCA300 Database*; John Wiley and Sons: Chichester, England, 1992; pp 278.

(59) Moulder, J. F.; Stickle, W. F.; Sobol, P. E.; Bomben, K. D. Data Interpretation. In *Handbook of X-Ray Photoelectron Spectroscopy*; Perkin-Elmer Corporation: Minnesota, USA, 1992; pp 18.

(60) Clark, D. T. The Modification, Degradation, and Synthesis of Polymer Surfaces Studied by ESCA. In *Photon, Electron, and Ion Probes of Polymer Structure and Properties,* Dwight, D. W., Fabish, T. J., Thomas, H. R., Eds.; ACS Symposium Series 162; American Chemical Society: Washington, DC, 1981; pp 247–291.

(61) Perfluorotributylamine. National Institute of Standards and Technology. http://webbook.nist.gov/cgi/cbook.cgi?ID=C311897&Mask=200#Mass-Spec (accessed Mar 06, 2018).

(62) Smith, M. *Understanding Mass Spectra: A Basis Approach*; John Wiley & Sons, Inc.: New Jersey, 2004; pp 287–288.

(63) Agraharam, S.; Hess, D. W.; Kohl, P. A.; Bidstrup Allen, S. A. Plasma Chemistry in Fluorocarbon Film Deposition from Pentafluoroethane/Argon Mixtures. *J. Vac. Sci. Technol. A* **1999**, *17*, 3265–3271.

(64) Chen, K. S.; Chang, Y. N.; Her, J. L. Surface Characteristics and Blood Compatibility of Plasma Polymerized Perfluorotributylamine Films. *ISPC-8 Tokyo*, **1987**, 1340–1346.

(65) Yang, M. R.; Chen, K. S.; He, J. L. The Interaction Between Blood and the Surface Characteristics of Plasma Polymerized Films. *Mater. Chem. Phys*. **1997**, *48*, 71–75.

(66) Lungu, C. P.; Lungu, A. M.; Akazawa, M.; Sakai, Y.; Sugawara, H.; Tabata, M. Fluorinated Carbon Films with Low Dielectric Constant Made from Novel Fluorocarbon Source Materials by RF Plasma Enhanced Chemical Vapour Deposition. *Jpn. J. Appl. Phys.* **1999**, *38*, L 1544–L 1546.

(67) Wada K. Shimadzu Corporation. International Marketing Division. *FTIR Talk Letter* **2009**, *11*, 1–10.

(68) Lin-Vien, D.; Colthup, N. B.; Fateley, W. G.; Grasselli, J. G. *The Handbook of Infrared and Raman Characteristic Frequencies of Organic Molecules*; Academic Press, Inc.: San Diego, 1991.

(69) Bellamy, L. J. *The Infra-Red Spectra of Complex Molecules*; Vol. 2; Chapman and Hall Ltd.: London, 1975.

(70) Pretsch, E.; Buhlmann, P.; Badertscher, M. *Structure Determination of Organic Compounds: Tables of Spectral Data*; Springer-Verlag: Berlin, 2009.

(71) Khalil, M. I.; Al-Qunaibit, M. M.; Al-zahem, A. M.; Labis, J. P. Synthesis and Characterization of ZnO Nanoparticles by Thermal Decomposition of a Curcumin Zinc Complex. *Arab. J. Chem.* **2014**, *7*, 1178–1184.

(72) Chakrabarti, C. L.; Akh, G.; Hutton, J. C. ATR and Reflectance IR Spectroscopy, Applications. *Spectrochim. Acta B* **1999**, *33*, 153–193.

(73) Goswami, D.; Medda, S. K.; De, G. Superhydrophobic Films on Glass Surface Derived from Trimethylsilanized Silica Gel Nanoparticles. *ACS Appl. Mater. Interfaces* **2011**, *3*, 3440–3447.

(74) Hong, J.-K.; Kim, H.-R.; Park, H.-H. The Effect of Sol on the Sol–Gel Derived Low Density SiO_2 Xerogel Film for Intermetal Dielectric Application. *Thin Film Solid* **1998**, *332*, 449–454.

(75) Li, Y.; Yerian, J. A.; Khan, S. A.; Fedkiw, P. S. Crosslinkable Fumed Silica-Based Nanocomposite Electrolytes for Rechargeable Lithium Batteries. *J. Power Sources* **2006**, *161*, 1288–1296.

(76) Stojanović, D. B.; Brajović, L.; Orlović, A.; Dramlić, D.; Radmilović, V.; Uskoković, P. S.; Aleksić, R. Transparent PMMA/Silica Nanocomposites Containing Silica Nanoparticles Coating under Supercritical Conditions. *Prog. Org. Coat.* **2013**, *76*, 626–631.

(77) Papageorgiou, D. G.; Kinloch, I. A.; Young, R. J. Mechanical Properties of Graphene and Graphene-Based Nanocomposites. *Prog. Mat Sci.*, **2017**, *90*, 75–127.

(78) Young, R. J.; Liu, M.; Kinloch, I. A.; Li, S.; Zhao, X.; Valles, C. The Mechanics of Reinforcement of Polymers by Grapheene Nanoplatelets. *Compos. Sci. Technol,*, **2018**, *154*, 110–116.

(79) Qu, S.; Huang, C. X.; Gao, Y. L.; Yang, G.; Wu, S. D.; Zang, Q. S.; Zhang, Z. F. Tensile and Compressive Properties of AISI 304L Stainless Steel Subjected to Equal Channel Angular Pressing. *Mater. Sci. Eng.* **2008**, *475*, 207–216.

4. Atomised Spray Plasma Deposition of Poly (Alkyl Acrylate) Coatings for Wet Electrical Protection Barrier

4.1 Background and Introduction

Surface modification with functional polymer coatings offers the possibility to improve specific physicochemical properties of material surfaces such as mechanical and electrical properties,[1] biocompatibility,[2] and wettability without the modification of their bulk properties. Specific applications of functionalised thin coatings are, for example, anti-fouling surfaces,[3] antibacterial,[4] oil–water separation,[5] adhesion properties,[6] membranes for fuel cells,[7] drug delivery,[8] tissue engineering,[9] biosensors,[10] organic electronic devices,[11] conducting thin films,[12] and so forth. Particularly, the surface modification with low-dielectric polymer thin films can be used as a wet electrical barrier to prevent short circuit of electronic devices which may occur when they are in contact with water.

Insulating materials are characterised for presenting low dielectric constant and low polarisation. These characteristics make the insulating materials to show no response in their polarisation and dipole moment under the influence of an applied electric field due to the absence of positive electron transport affinity by the molecules of the insulating materials.[13] The polarisation of the organic molecules is related to the refractive index and molar refraction. The lower the refractive index, the lower the polarisation and the greater the electron affinity, and thus, the higher the dielectric strength (molar refractions expressed in 10^{-6} m^3: 1.296 for C–C; 1.44 for C–F; 1.676 for C–H).[14] Therefore, insulating materials with sufficiently large film thickness can prevent the electron transport, water diffusion, corrosion, and dielectric breakdown at the polymer–electrode interface under an applied electric field; otherwise, the electron transport could cause polymer degradation and electrode corrosion, leading to the failure of electronic devices from any water spillage or moisture (e.g., smartphones, hearing aids, tablets, etc.).

Electrical barrier polymer coatings exposed to a high applied electric field have been prepared by using different insulating materials with high dielectric strength, low permeability to moisture which consequently prevents the

corrosion of the metal surface, for example: parylene,[15] polysilazane,[16] perfluoroalkyl acrylates,[17] alkyl acrylates,[17] alkanes,[18] tetraethylorthosilicate,[19] and a polyisoprene/allyl mercaptan multilayer coating.[20] Various surface functionalisation techniques have been used for deposition of these electrical barriers or anticorrosive coatings: chemical vapour jet deposition,[15] UV polymerisation,[16] nanocasting,[21] pulsed plasma polymerisation,[17,18] spin coating, [22] chemical vapor deposition,[19] and plasma polymerisation.[20]

Plasma polymerisation technique has been used for the deposition of functional thin polymer films with a regular structure where the precursor is activated by the reactive species created in the plasma (electrons, ions, radicals, vacuum UV photons).[23] In precursors containing the reactive acrylate group, the reactive plasma species activate the carbon–carbon double bond to follow the conventional radical polymerisation and polymer growth on the substrate surface. Therefore, in this work, plasma polymerisation was coupled with a spray coating method to increase the deposition rate and able to deposit precursors with low vapour pressure, which is a limitation in the vapour-phase plasma polymerisation.

Recently, there is a higher interest in using hydrocarbon polymers as environmentally friendly alternatives to fluorocarbon polymers; several groups have reported the plasma polymerisation of hydrocarbon polymers for different applications, for instance: Wood & Badyal[24] reported the atomised spray plasma deposition of isodecyl acrylate to manufacture functional thin films (3300 ± 500 nm min^{-1} of deposition rate) with a water contact angle value (WCA) of ~80°, which is similar to the WCA values for the thin oily functional coatings (tacky to the touch) reported in this work which were prepared following the same methodology and further compared with the non-oily solid functional coatings with WCA values of ~110° reported in this work employing a proposed methodology of plasma post-treatment–atomised spray plasma deposition. Furthermore, Mertz et al.[25] carried out the atmospheric plasma copolymerisation of perfluorododecyl acrylate and dodecyl acrylate at different concentration ratio to obtain superhydrophobic coatings. The plasma polymerisation of dodecyl acrylate resulted in coatings with WCA of ~80°. Legein et al.[26] reported the use of plasma pre-treatment step before carrying out the plasma polymerisation of perfluoroalkyl acrylates and alkyl acrylates at

moderate applied power as a strategy to improve crosslinking degree and the wet electrical barrier performance. Coulson et al.[18] reported the plasma polymerisation of alkanes of different chain lengths (e.g., tetradecane) to fabricate wet electrical barrier coatings to protect electronic devices. They heated both the delivering monomer and the plasma chamber and ignited the plasma at 30 W for 45 min to obtain a protective coating of ~1.1 μm with an electrical barrier performance of ~4.7 x 10^7 Ω at 8 V. Moreover, Coulson et al.[27,28] found that the plasma polymerisation of perfluorooctyl acrylate carried out at low power (continuous wave plasma at 50 W) resulted in oily/sticky coatings. Thus, they overcame this problem by (i) increasing the applied power up to 200 W in continuous wave plasma or (ii) mixing the precursor with a crosslinking agent (pulsed plasma polymerisation was carried out at 50 W); the electrical barrier coatings of ~1.5 μm showed an electrical barrier performance of ~9.2 x 10^9 Ω at 8 V. Therefore, some of these investigations used different approaches in conjunction with the plasma polymerisation to overcome the oiliness of the plasma polymer coatings such as: the employment of the two-step process,[18] high temperature,[15] or the use of crosslinking agents.[28] However, these experimental procedures may lead to lengthy processes.[18,26,27,28]

In this work, the atomised spray plasma deposition technique was used to prepare hydrophobic electrical barrier coated microcircuit boards in conjunction with a plasma post-treatment step as a strategy to overcome the oiliness of the plasma polymer—polymer oiliness is caused by the low-energy excited plasma species (e.g., radicals) leading to the oligomer formation and low polymerization degree[47]—and to control the crosslinking degree, electrical and mechanical properties and thus reducing the lengthy process as compared to previous reports.[18,20,26,27] Isodecyl acrylate was chosen due to the long hydrophobic alkyl chain which possesses high dielectric resistance due to the low polarisation and migration of electrical charges within the alkyl chains, and the acrylate functional group suitable to initiate a radical polymerization mechanism as compared to other hydrophobic alkyl chain precursors without any polymerizable functional group.[18] Surface modification was carried out by injecting the monomer precursor in the form of droplets into a low-pressure electrical discharge, where the reactive plasma species

activate the droplet surface forming oligomeric species, so they get deposited onto the reactive surface.[29] Furthermore, plasma post-treatment was proposed to provide more energy and promote more radicals onto the oligomer surface—oily coating—leading to a complete polymerization and higher crosslinking degrees due to the continual reactive plasma species exposure during the post-atomisation step, Scheme 4.1. To this date, there are not reports about using plasma post-treatment during a low-pressure plasma polymerization process to improve the polymerization or crosslinking degrees or to overcome the coating oiliness as mentioned above. Therefore, the electrical barrier coatings deposited by the APSD technique in conjunction with the plasma post-treatment step displayed high wet electrical barrier performance which are comparable to electrical barrier coatings with the same film thickness already reported.[18,27,28]

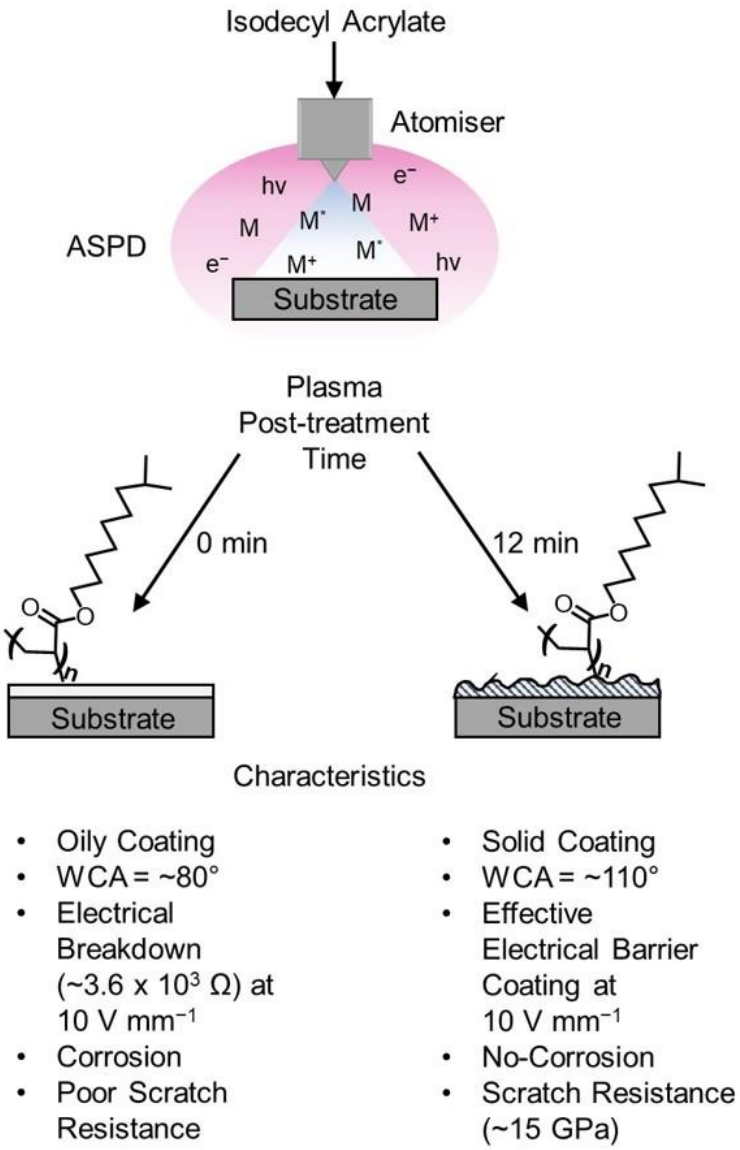

Scheme 4.1: Schematic illustration and characteristics of the ASPD poly (isodecyl acrylate) coatings at different plasma post-treatment times.

4.2 Results and Discussion

4.2.1 Atomised Spray Plasma Deposition

Plasma polymerisation of isodecyl acrylate (+99.9% Sigma-Aldrich Ltd.) was carried out by using the atomised spray plasma deposition technique in conjunction with a plasma post-treatment in a single step to control the mechanical properties and wet electrical-barrier performance of the plasma polymer coated micro-circuit boards (power: 50 W; flow rate: 8 ± 3 x 10^{-4} mL s^{-1}; plasma post-treatment: 0–12 min). In contrast, the absence of the plasma

post-treatment step led to poor polymerisation of the ASPD poly (isodecyl acrylate) coatings resulting in oily surfaces and electrical breakdown of the plasma polymer coated micro-circuit boards.

During the atomisation of the monomer precursor into the electrical discharge, the reactive species within the plasma (electrons, ions, vacuum UV photons, and radicals) activate the droplet surface forming oligomers within the plasma phase, subsequently, the polymer propagation continues upon striking onto the activated surface,[30,31] then during the plasma post-treatment, the reactive plasma species further transfer energy to the surface molecules, and then, promote the polymerisation of the unreacted molecules trapped within the plasma polymer coating and enhancing the crosslinking density and mechanical properties as confirmed by XPS and infrared analysis, and electrical and microindentation measurements.

4.2.2 X-ray Photoelectron Spectroscopy

XPS analysis of the plasma post-treated ASPD poly (isodecyl acrylate) coatings showed evidence of carbon and oxygen as the elemental composition of the precursor monomer. The absence of any Si(2p) XPS signal confirmed that the ASPD poly (isodecyl acrylate) coated silicon substrate is conformal and pin-hole free, Table 4.1 and Figure 4.1. In contrast, in the absence of the plasma post-treatment, the ASPD poly (isodecyl acrylate) coatings resulted in oily coatings due to the deficiency of energy provided by the reactive plasma species leading to incomplete polymerisation. Therefore, XPS analysis was not carried out as the entrapped volatile monomer, contained into the ASPD poly (isodecyl acrylate) coatings, could contaminate the vacuum chamber of the XPS instrument.

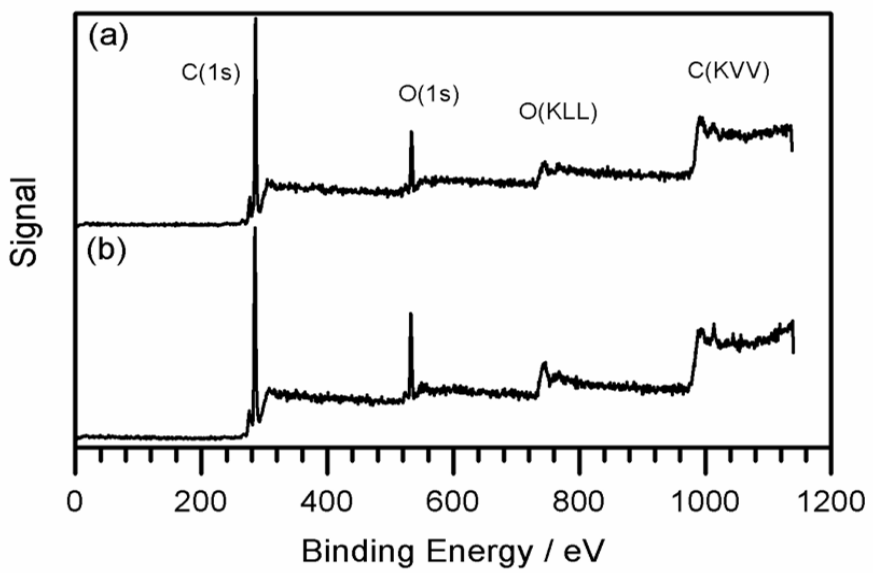

Figure 4.1: Wide scan XPS spectra of ASPD poly (isodecyl acrylate) coatings at different plasma post-treatment times: (a) 6 min, and (b) 12 min.

Table 4.1: XPS compositions for theoretical isodecyl acrylate monomer and ASPD poly (isodecyl acrylate) coatings at different plasma post-treatment times. There is no XPS spectrum for ASPD poly (isodecyl acrylate) coating without plasma post-treatment because of the entrapment of volatile monomer within the coatings.

System / Plasma Post-treatment Time	**Atomic Composition / %**		**C:O Ratio**	**C(1s) Component / %**			**O(1s) Component / %**	
	C	**O**		**$\underline{C}_xH_y$**	**<u>C</u>–O**	**O–<u>C</u>=O**	**C=<u>O</u>**	**C–<u>O</u>**
Theoretical	86.7	13.3	6.5	84.6	7.7	7.7	50	50
ASPD poly (isodecyl acrylate) coating, 6 min	88.4 ± 0.8	11.6 ± 0.8	7.7 ± 0.6	83.8 ± 0.5	11.8 ± 1.3	4.3 ± 1.0	56.7 ± 3.3	43.3 ± 3.3
ASPD poly (isodecyl acrylate) coating, 12 min	86.7 ± 1.3	13.3 ± 1.3	6.6 ± 0	79.5 ± 5.3	15.5 ± 4.3	5.0 ± 1.4	79.7 ± 4.6	20.3 ± 4.6

The C(1s) XPS spectrum of each ASPD poly (isodecyl acrylate) coating was fitted to three Gaussian Mg $K\alpha_{1,2}$ components in conjunction with their corresponding Mg $K\alpha_{3,}$ and Mg $K\alpha_{4}$ satellite peaks shifted towards lower binding energies by ~8.4 and ~10.2 eV respectively, Figure 4.2.[32] The C(1s) Mg $K\alpha_{1,2}$ components being: hydrocarbon carbon $\underline{C}_xH_y$ at 285.0 eV, alkoxy $\underline{C}$–O at 286.7 eV, and ester O–$\underline{C}$=O at 289.0 eV.[33] The carbon component compositions changed as a function of the plasma post-treatment time: the alkoxy, $\underline{C}$–O, increased from 7.7% (theoretical) to ~15.5% at 12 min of plasma post-treatment while the carbonyl, C=O, decreased slightly from 7.7% to ~5.5%, Table 4.1. which is likely attributed to the molecular fragmentation and rearrangement / polymerisation on the polymer surface and deposition of low-weight molecular fragments during the plasma post-treatment of the ASPD poly (isodecyl acrylate) coatings. This change of the carbon component composition may be attributed to the molecular fragmentation and rearrangement/polymerisation on the polymer surface during the plasma post-treatment of the ASPD poly (isodecyl acrylate) coatings—the incidence of vacuum UV photons on the plasma polymer causes further polymerisation and photochemical reactions through the oxygen-containing functionalities as denoted by the Norrish Mechanisms. [23,34,35]

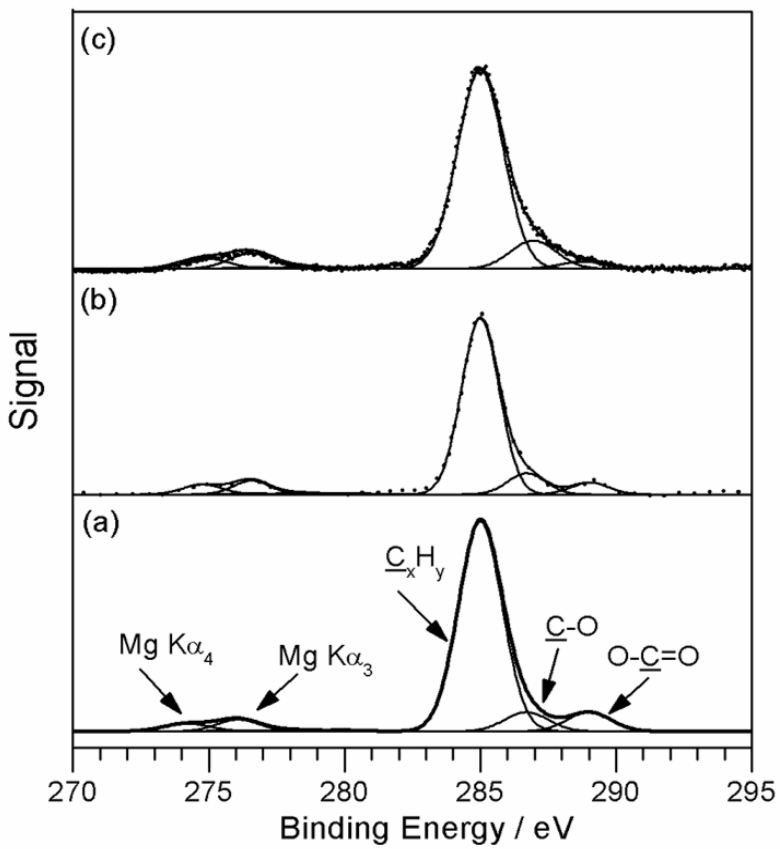

Figure 4.2: C(1s) XPS spectra of (a) theoretical isodecyl acrylate monomer, and ASPD poly (isodecyl acrylate) coatings at different plasma post-treatment times: (b) 6 min; and (c) 12 min. XPS analysis of ASPD poly (isodecyl acrylate) coating without plasma post-treatment was not carried out due to its oily/sticky characteristics and the entrapment of volatile monomer within the coatings.

The O(1s) XPS spectrum of the ASPD poly (isodecyl acrylate) coating was fitted to two main Mg Kα$_{1,2}$ components: C=O at 532.5 eV, and C–O at 533.9 eV.[33] At 12 min of plasma post-treatment, the composition of the carbonyl, C=O, increased up to ~80% at the expense of the alkoxy component, C–O. The overall atomic concentration indicated that the oxygen concentration did not change significantly. Thus, the increase of oxygen concentration in the carbonyl group may be attributed to further fragmentation rather than the reaction of trapped radicals within the polymer coatings with oxygen-containing functionalities after exposing the coatings to the environment, Table 4.1, Figure 4.3. Moreover, the XPS carbon and oxygen elemental composition obtained from the ASPD poly (isodecyl acrylate) coatings are comparable to

those already reported in the literature by Wood et al.[24] and Loyer et al.[36] using a similar plasma deposition system.

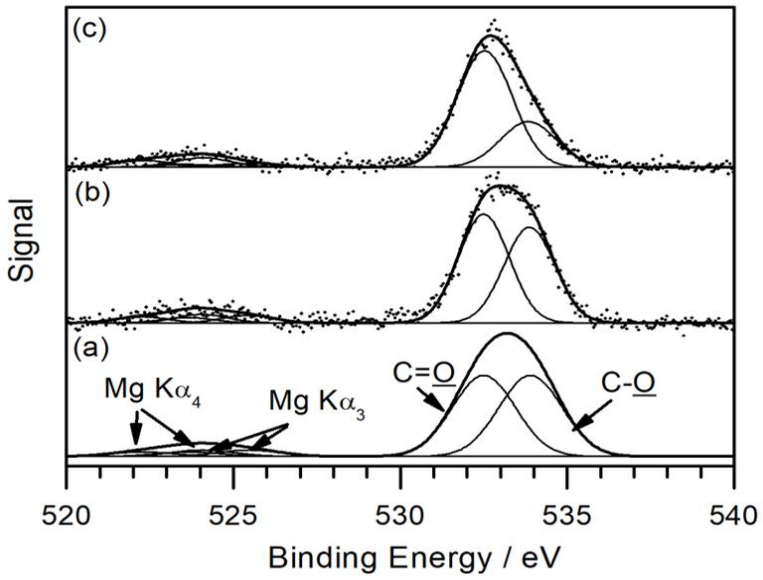

Figure 4.3: O (1s) XPS spectrum of (a) theoretical isodecyl acrylate monomer, and ASPD poly (isodecyl acrylate) coating at different plasma post-treatment times: (b) 6 min; and (c) 12 min. XPS analysis of ASPD poly (isodecyl acrylate) coating without plasma post-treatment was not carried out due to its oily/sticky characteristics because of the entrapment of volatile monomer within the coatings.

4.2.3 Infrared Spectroscopy

The infrared spectra of ASPD poly (isodecyl acrylate) coatings at different plasma post-treatment times indicate the disappearance of the vinyl group of the acrylate suggesting that the polymerisation was carried out mainly by the conventional free radical polymerisation through the vinyl group; there is not significant difference among the infrared spectra of the plasma post-treated ASPD poly (isodecyl acrylate) coatings, except for the observed carbonyl group distortion at 12 min of plasma post-treatment time, Figure 4.4 and Figure 4.5. The ASPD poly (isodecyl acrylate) coating, after different plasma post-treatment times, showed the retention of functional groups associated with the monomer precursor with characteristic infrared bands comprising the alkyl chain (2963–2868 cm^{-1}), carbonyl ester C=O (1731 cm^{-1}) and alkoxy C–O (1269 cm^{-1} and 1176 cm^{-1}) absorbances. [24,37] The disappearance of the vinyl

group C=C (1636 cm^{-1}),[24] and $=CH_2$ (981 cm^{-1}, and 808 cm^{-1}) absorbances indicates that conventional polymerisation was carried out during the plasma deposition process—The retention of the carbonyl ester C=O, and alkoxy C–O absorbances, and the disappearance of the vinyl group are in accordance with previously reported plasma deposition of alkyl acrylates.[17,24] After plasma post-treatment of the plasma polymer coatings, the carbonyl C=O functional group presented a shift toward higher wavenumber from 1726 ± 0.2 cm^{-1} to 1738 ± 1.6 cm^{-1} and a reduction of intensity and slight distortion of the infrared peak, which may indicate the formation of an amorphous phase[38] or an electronic change in the carbonyl group,[42] Figure 4.5 and Table 4.2. Overall, the relative disappearance of the vinyl group started at 0 min of plasma post-treatment, however, this led to low polymerization degree of the ASPD poly (isodecyl acrylate) coatings due to the low energy-per-molecule ratio. Further improvement of the polymerization degree was achieved at >6 min of plasma post-treatment which related to the carbonyl group modification but also to a higher polymerization degree leading to the improvement of the mechanical properties of the ASPD poly (isodecyl acrylate) coatings.

Alternatively, argon plasma ignited at 50 W for 12 min was used in the post-treatment step of the ASPD poly(isodecyl acrylate) coatings, Figure 4.4 and Figure 4.5. In the corresponding infrared spectrum of the argon plasma post-treated ASPD poly(isodecyl acrylate) coatings, the carbonyl C=O absorbance presented the similar peak distortion as described before for the 12 min plasma post-treatment of the APSD poly(isodecyl acrylate) coatings—no argon plasma post-treatment. This is because argon plasma produces mainly ions (Ar^+) and energetic UV photons which have enough energy to activate the vinyl group of the precursor to initiate the radical polymerisation,[1,23,39] but also UV photons (λ > 200 nm),[23] which can penetrate up to few microns into the polymer bulk, can produce radicals in the oxygen-containing functionalities of the acrylate group and then participate in the photochemical reactions described by the Norrish Mechanism for oxygen-containing functional groups,[23,35,40,41]contributing to further polymerisation and increasing the crosslinking of the plasma polymer coatings as observed by the XPS analysis, and mechanical measurements.

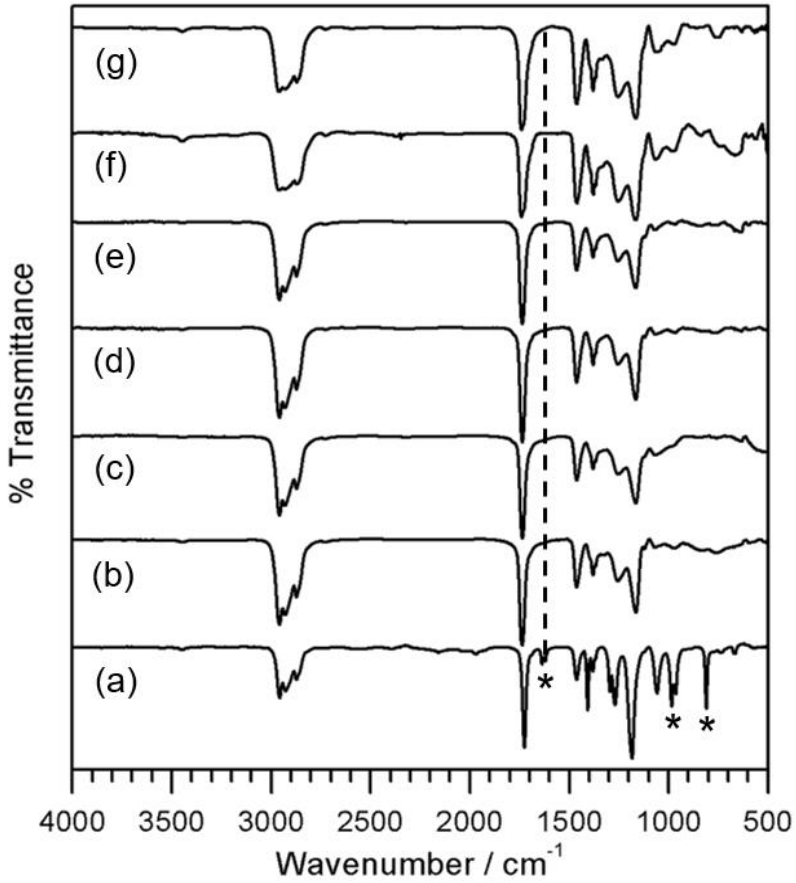

Figure 4.4: Infrared spectra of (a) ATR isodecyl acrylate precursor. RAIRS of ASPD poly (isodecyl acrylate) coating at different plasma post-treatment times: (b) 0 min; (c) 2 min; (d) 3 min; (e) 6 min; (f) 12 min; and (g) 12 min of argon plasma post-treatment of ASPD poly (isodecyl acrylate) coating. ✶ indicates $C=CH_2$ absorbance at 1634 cm^{-1}, 981 cm^{-1}, and 808 cm^{-1}.[24,37]

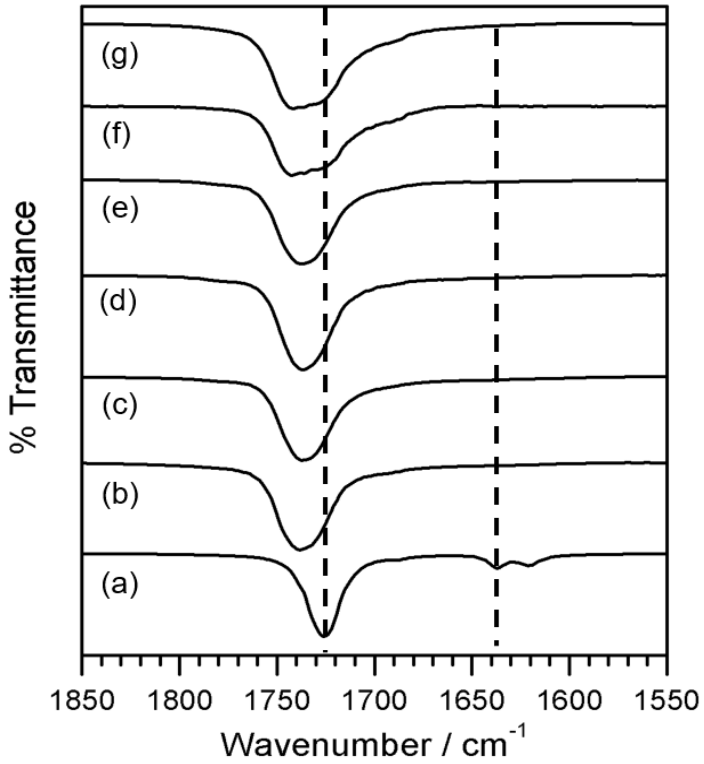

Figure 4.5: Infrared spectra of the carbonyl functional group region: (a) ATR isodecyl acrylate precursor. RAIRS of ASPD poly (isodecyl acrylate) coatings at different plasma post-treatment times: (b) 0 min; (c) 2 min; (d) 3 min; (e) 6 min; (f) 12 min; and (g) 12 min of argon plasma post-treatment of ASPD poly (isodecyl acrylate) coating. Dashed line indicates C=O stretch (1726 cm^{-1}), and C=C stretch (1636 cm^{-1}).[37]

Table 4.2: Infrared assignments for isodecyl acrylate and ASPD poly (isodecyl acrylate) coatings.[42,43]

Absorption Frequency / cm^{-1}	**Assignment**
2963	CH_3 antisymmetric stretching
2927	CH_2 antisymmetric stretching
2868	CH_3 symmetric stretching
1731	C=O stretching
1634	C=C stretching
1462	$–CH_2–$ stretching
1402	$=CH_2$ bending
1373	$–CH(CH_3)_2$ symmetric bending
1305–1295	$–CH_2–$ bending
1300–1000 (1269, 1179)	C–O stretching
1175–1140, 1060–1040	$–CH(CH_3)_2$ stretching
981, 808	$=CH_2$ bending

4.2.4 Scanning Electron Microscopy

Plasma post-treatment time affects the surface topography of the ASPD poly (isodecyl acrylate) coatings as observed in SEM images, Figure 4.6. The absence of the plasma post-treatment on the ASPD poly (isodecyl acrylate) coatings resulted in oily/sticky coatings, and thus, they were unsuitable for SEM analysis. The effect of the plasma post-treatment on the ASPD poly (isodecyl acrylate) coating led to the formation of wrinkling pattern, and it is clear that the higher the plasma post-treatment time, the denser the wrinkling pattern. It is suggested that this wrinkling formation is due to the compressive stress generated by the polymerization rate gradient between top and bulk layers under the incident of UV photons generated during the plasma post-treatment to the ASPD poly (isodecyl acrylate) coatings. The plasma polymer coatings absorbed more energy supplied by the plasma in the post-treatment step causing further polymerisation through photochemical reactions,

enhancing the mechanical properties in accordance with the XPS, infrared, and microindentation analyses.

Other authors have reported the formation of the wrinkling pattern of acrylate-based polymer coatings fabricated by using UV photo-polymerisation[44] or plasma polymerisation,[45,46] and found correlation between the wrinkling formation and crosslinking densities. Comparative to the plasma post-treatment process reported in this work, previous works[18,24,25,28] have reported several strategies with the aim to increase the crosslinking density and to overcome the oiliness of the alkyl-acrylate-based plasma polymer coatings, such as crosslinking agents,[28] heating of the monomer precursor,[17,19] plasma co-polymerisation of alkyl and perfluoroalkyl acylates,[25] and higher applied power.[27]

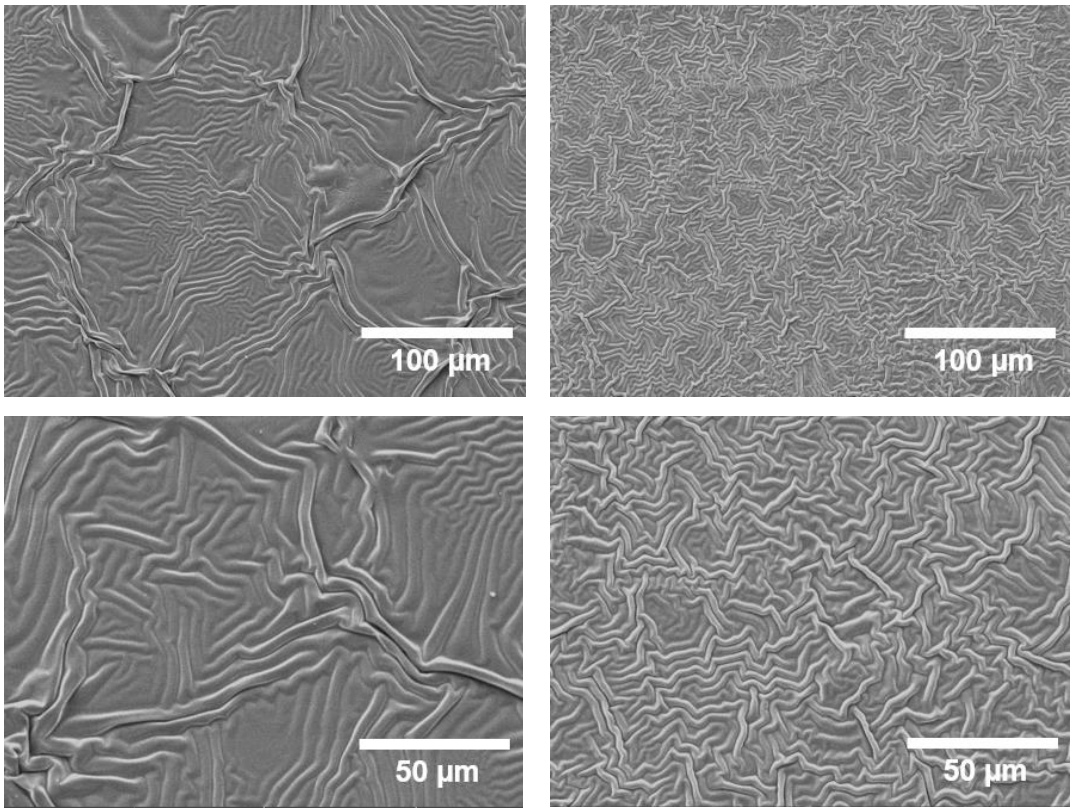

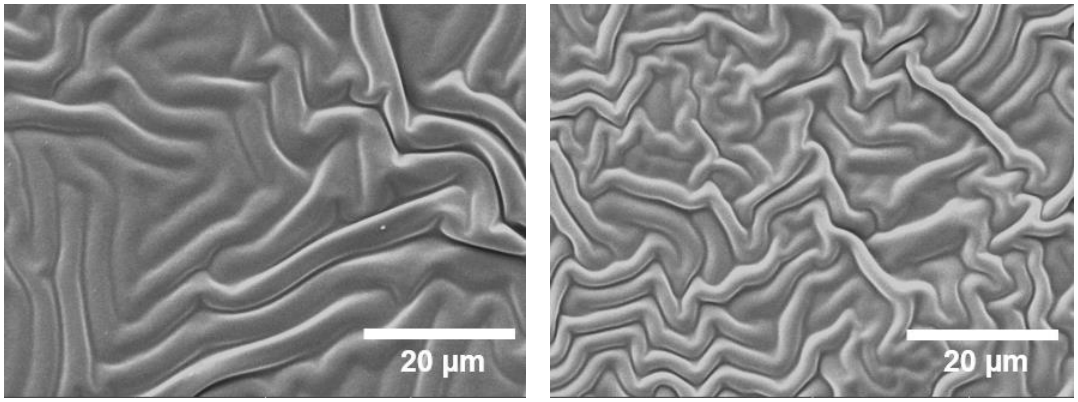

Figure 4.6: SEM images of ASPD poly(isodecyl acrylate) coatings treated at different plasma post-treatment times: (left column) 6 min (thickness: 6.9 ± 0.9 µm); and (right column) 12 min (thickness: 3.5 ± 2.4 µm).

4.2.5 Contact Angle

The water contact angle (WCA) values of the ASPD poly (isodecyl acrylate) coatings employing 6 and 12 min of plasma post-treatment were 89 ± 5° and 110 ± 5°, respectively. These results suggest that the denser wrinkling pattern is associated with higher WCA values, which strongly depends on the plasma post-treatment time. Similarly, Wood et al.[24] fabricated poly(isodecyl acrylate) coatings employing both ASPD and its counterpart gas-phase plasma deposition methods—with no plasma post-treatment—and they produced coatings with WCA values of ~80° and ~66°, respectively, which were lower than those reported in this work. On the other hand, Bardon et al.[47] deposited dodecyl acrylate with a diacrylate (crosslinking agent) by atmospheric atomised spray plasma deposition to enhance the polymerisation of the alkyl acrylate, and thus, to improve the mechanical properties and wettability. They obtained wrinkling-patterned plasma polymer coatings with WCA of ~110°—similar WCA values as reported in this work using plasma post-treatment, which provide enough energy to enhance the polymerisation of the alkyl acrylate.

4.2.6 Electrical Barrier

The wet electrical barrier performance of the ASPD poly (isodecyl acrylate) coated micro-circuit boards were evaluated as a function of the plasma post-

treatment time for an applied electric field of 10 V mm^{-1} when the samples were immersed in water for 13 min, Figure 4.7. The wet electrical barrier performance of the ASPD polymer coated micro-circuit boards increased ~6 orders of magnitude when the plasma post-treatment time increased from 0 to 6 min, and thus, protecting the ASPD polymer coated micro-circuit boards from electrical failure by dielectric breakdown. At plasma post-treatment time higher than 6 min, these ASPD coated micro-circuit boards reached a plateau on the wet electrical barrier performance. Therefore, plasma post-treatment is able to tune the crosslinking density of the plasma polymer coatings and prevent the electrical breakdown of the ASPD coated micro-circuit boards tested under the applied electric field in water. Otherwise, the formation of conductive channels could lead to polymer degradation, water diffusion, corrosion, and thus, failure of the micro-circuit boards.

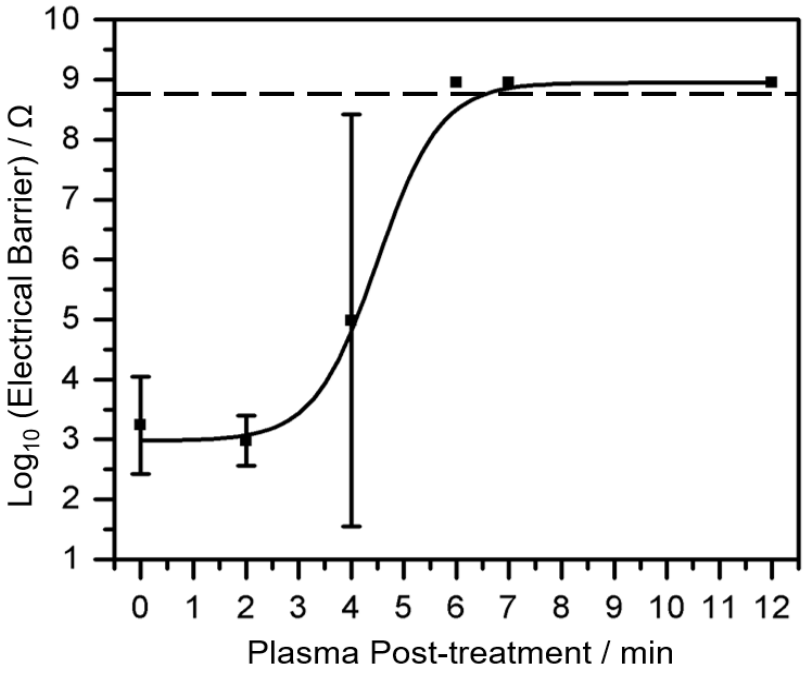

Figure 4.7: Wet electrical barrier after immersion in water for 13 min under an applied electric field of 10 V mm^{-1} (8 V), for ASPD poly (isodecyl acrylate) coatings exposed to different plasma post-treatment times. The samples above the dashed line reached the instrument detection limit of 8 x 10^8 Ω, and their standard deviation is Log_{10} < 0.04 Ω.

The electrical barrier performance of the optimum 12 min plasma post-treatment was evaluated as a function of the film thickness under the applied electric field of 10 V mm^{-1} to determine the effective minimum film thickness, Figure 4.8. The electric current transport on the 12 min plasma post-treated ASPD poly (isodecyl acrylate) coatings was absence at a plasma polymer film thicker than 1.2 ± 0.3 µm. Overall, this result confirms that not only the plasma post-treatment plays a role in the prevention of the electrical breakdown but also the film thickness of the plasma polymer. Similarly, Coulson et al[27,28] and Fraser et al.[20] reported an effective electrical barrier coatings of 1.1–1.5 µm under the same applied electric field of 10 V mm^{-1}. They used different approaches such as a multilayer plasma polymer,[20] or longer plasma deposition times.[18]

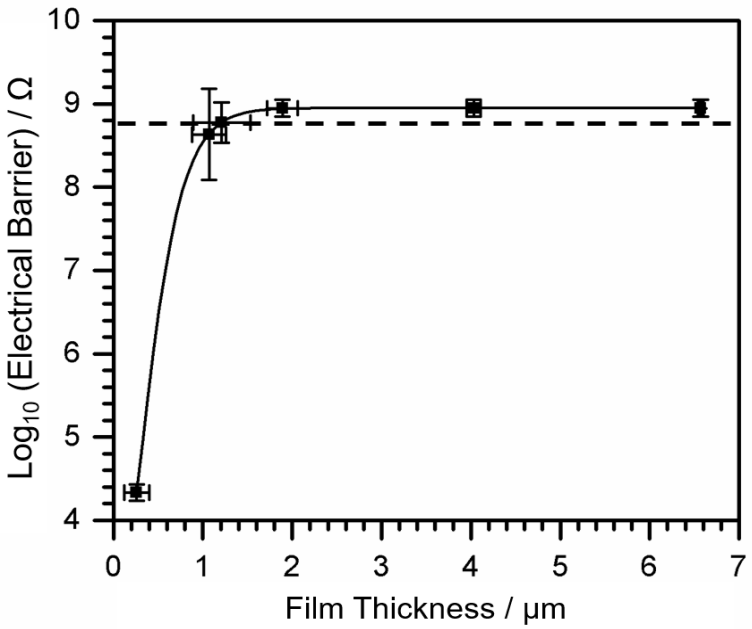

Figure 4.8: Wet electrical barrier as a function of the film thickness of the optimum 12 min plasma post-treatment of ASPD poly (isodecyl acrylate) coatings. Samples were immersed in water under an applied electric field of 10 V mm^{-1} (8 V). Samples above the dashed line reached the instrument detection limit of 8 x 10^8 Ω.

4.2.7 Microindentation

Microindentation Vickers hardness was carried out on the plasma post-treated ASPD poly (isodecyl acrylate) coatings as a function of the applied load, Figure

4.9. The mechanical properties were enhanced upon longer plasma post-treatment time, showing an increase of > 4 GPa when increasing the plasma post-treatment time from 6 to 12 min. On the contrary, ASPD poly (isodecyl acrylate) coatings with plasma post-treatment time lower than 6 min resulted in sticky surfaces which also presented poor electrical barrier values, Figure 4.7. Therefore, the plasma post-treatment allows to tune the crosslinking density which in turn enhances mechanical resistance to plastic deformation and electrical barrier performance of the ASPD poly (isodecyl acrylate) coatings.

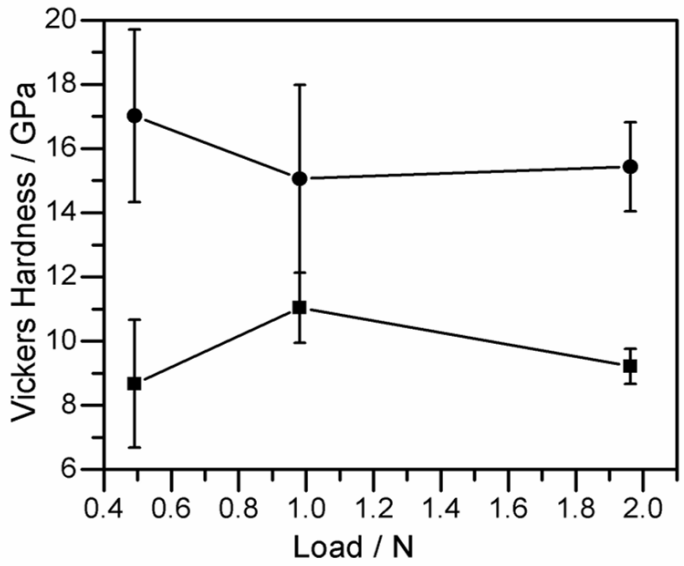

Figure 4.9: Microindentation Vickers hardness of ASPD poly (isodecyl acrylate) coatings as a function of the plasma post-treatment time: (■) 6 min (thickness: 6.5 ± 0.6 µm) and (●) 12 min (thickness: 3.3 ± 2.5 µm).

4.3 Conclusions

Wet electrical barrier coatings were prepared through the single-step ASPD technique. The resulting plasma polymer coatings were further cured by employing a modified ASPD process—plasma post-treatment was used to reduce the oiliness of the plasma polymers due to the trapped liquid monomer precursor into the plasma polymer coating, and to increase the crosslinking density of the plasma polymer coatings. Moreover, the hydrophobicity, wet

electrical barrier performance, and mechanical properties increased as a function of the plasma post-treatment time. The increment of the crosslinking density in the plasma post-treatment step is mainly attributed to the vacuum UV radiation and ion bombardment through the C=C double bond of the acrylate group as confirmed by infrared analysis obtained from the argon plasma post-treatment—argon plasma only produces Ar^+ and UV photons—which may follow the same photochemical reaction pathways. The chemical reaction pathway is mainly attributed to the opening of the π-bond of the reactive acrylate group leading to a conventional radical polymerisation. However, the crosslinking through the carbon–oxygen bond may play a minor role during the plasma post-treatment step. Therefore, these hydrophobic insulating plasma polymer coatings exceed the electrical barrier performance of an applied electric field of 10 V mm^{-1}, which make it suitable for a range of electronic devices operating up to 8 V, to prevent the electrical breakdown when in contact with moisture or water.

4.4 References

(1) Yasuda, H. Plasma Polymerization*;* Academic Press, Inc.; Orlando Florida; 1985.

(2) Wong, E. H. H.; Khin, M. M.; Ravikumar, V.; Si, Z.; Rice, S. A.; Chan-Park, M. B. Modulating Antimicrobial Activity and Mammalian Cell Biocompatibility with Glucosamine-Functionalised Star Polymers. *Biomacromolecules* **2016**, *17*, 1170–1178.

(3) Kim, S. H.; Kim, M.; Lee, J, H.; Lee, S.-J. Self-Cleaning Transparent Heat Mirror with a Plasma Polymer Fluorocarbon Thin Film Fabricated by a Continuous Roll-to-Roll Sputtering Process. *ACS Appl. Mater. Interfaces* **2018**, *10*, 10454–10460.

(4) Vasilev, K.; Griesser, S. S.; Griesser, H, J. Antibacterial Surfaces and Coatings Produced by Plasma Techniques. *Plasma Process. Polym.* **2011**, *8*, 1010–1023.

(5) Zhang, L.; Zhang, Z.; Wang, P. Smart Surfaces with Switchable Superoleophilicity and Superolephobicity in Aqueous Media: Toward Controllable Oil / Water Separation. *NPG Asia Materials* **2012**, *4*, 1–8.

(6) Forooshani, P. K.; Lee, B. P. Recent Approaches in Designing Bioadhesive Materials Inspired by Mussel Adhesive Protein. *J. Polym. Sci*. **2017**, *55*, 9–33.

(7) Walker, M.; Baumgartner, K. M.; Feichtinger, J.; Kaiser, M.; Rauchle, E. Barrier Properties of Plasma-Polymerized Thin Films. *Surf. Coat. Technol.* **1999**, *116–119*, 996–1000.

(8) Bhatt, S.; Pulpytel, J.; Mirshahi, M.; Arefi-Khonsari, F. Plasma co-Polymerized Nano Coatings — As a Biodegradable Solid Carrier for Tunable Drug Delivery Applications. *Polymer,* **2013**, *54*, 4820–4829.

(9) Girard-Lauriault, P.; Mwale, F.; Iordanova, M.; Demers, C.; Desjardins, P.; Wertheimer, M. R. Atmospheric Pressure Deposition of Micropatterned Nitrogen-Rich Plasma-Polymer Films for Tissue Engineering. *Plasma Process. Polym.* **2005**, *2*, 263–270.

(10) Basarir, F.; Cuong, N.; Song, W.-K.; Yoon, T.-H. Surface Modification via Plasma Polymerization of Allylamine for Antibody Immobilization*. Macromol. Symp.* **2007***, 249*, 61–66.

(11) Bazaka, K.; Ahmad, J.; Oelgemoller, M.; Uddin, A. Photostability of Plasma Polymerized γ-terpinene Thin Films for Encapsulation of OPV. *Sci. Rep.* **2017**, *7*, 45599.

(12) Schmittgens, M. W. R.; Nocke, A.; Hecker, D.; Liepelt, M.; Schultheib, M. L. E. Plasma Deposition of Conductive Polymer Composites for Strain Sensor Applications. *Procedia Chem.* **2009**, *1*, 879–882.

(13) Zakrevskii, V. A.; Sudar, N. T.; Zaopo, A., Dubitsky, Y. A. Mechanism of Electrical Degradation and Breakdown of Insulating Polymers. *J. Appl. Phys.* **2003**, *93*, 2135–2139.

(14) Blythe, T.; Bloor, D. Electrical Properties of Polymers. Cambridge University Press: Cambridge, 2005; pp 27–58, 186–195.

(15) Biswas, S.; Shalev, O.; Pipe, K. P.; Shtein, M. Chemical Vapor Jet Deposition of Parylene Polymer Films in Air. *Macromolecules* **2015**, *48*, 5550–5556.

(16) Kazutoshi, M. Manufacture of Moisture-Barrier Films for Use in Electronic Devices. Patent JP 2013086501, May 13, 2013.

(17) Coulson, S. R.; Evans, D.; Hellwing, T.; Hopper, F.; Poulter, N.; Siokou, A.; Telford, C. Method for Forming a Coating on an Electric or Electrical Device. Patent WO 2016/198855 A1, Dec 15, 2016.

(18) Coulson, S. R.; Evans, D.; Siokou, A.; Telford, C. Coating. Patent WO 2016/198856, Dec 15, 2016.

(19) Baisl, R.; Popp, M.; Schlenker, T.; Lang, E.; Trummer-Sailer, E. Electronic Component with Moisture Barrier Layer. Patent US 2015/0027541 A1, Jan 29, 2015.

(20) Fraser, R. C.; Carletto, A.; Wilson, M.; Badyal, J. P. S. Plasmachemical Double Click Thiol–ene for Wet Electrical Barrier. *ACS Appl. Mater. Interfaces* **2016**, *8*, 21832–21838.

(21) Chang, K.-C.; Ji, W.-F.; Lai, M.-C.; Hsiao, Y.-R.; Hsu, C.-H.; Chuang, T.-L.; Wei, Y.; Yeh, J.-M.; Liu, W.-R. Synergistic Effects of Hydrophobicity and Gas Barrier Properties on the Anticorrosion Property of PMMA Nanocomposite Coatings Embedded with Graphene Nanosheets. *Polym. Chem.* **2014**, *5*, 1049–1056.

(22) Wang, J.; Pan, T.; Zhang, J.; Xu, X.; Yin, Q.; Han, J.; Wei, M. Hybrid Films with Excellent Oxygen and Water Vapor Barrier Properties as Efficient Anticorrosive Coatings. *RSC Adv.* **2018**, *8*, 21651–21657.

(23) Friedrich, J. The Plasma Chemistry of Polymer Surfaces: Advanced Techniques for Surface Design; Wiley-VCH: Germany, 2012.

(24) Wood, T. J.; Badyal, J. P. S. Atomized Spray Plasma Deposition (ASPD) of Structurally Well-Defined Alkyl Functionalized Layers. *Surf. Coat. Tech.* **2013**, *227*, 28–31.

(25) Mertz, G.; Delmee, M.; Bardon, J.; Martin, A.; Ruch, D.; Fouquet, T.; Garreau,, S.; Airoudj, A.; Marguier, A.; Ploux, L.; Roucoules, V. Atmospheric Pressure Plasma Co-Polymerization of Two Acrylate Precursors: Toward the Control of Wetting Properties. *Plasma Process Polym.* **2018**, *15*, 1–11.

(26) Legein, F.; Martens, P.; Rogge, E. Surface Coatings. Patent WO 2014/026967 A2, Feb 20, 2014.

(27) Coulson, S. R.; Evans, D.; Siokou, A.; Telford, C. Coatings. Patent US 2018/0171171 A1, Jun 21, 2018.

(28) Coulson, S.; Evans, D.; Siokou, A.; Telford, C. Coatings. Patent BE1024652B1, May 16, 2018.

(29) Ward, L. Application of a Coating Forming Material onto at Least one Substrate. Patent WO 2003101621 A2, Dec 11, 2003.

(30) Morosoff, N.; Patel, D. L. Crosslink Density of Plasma Polymer Deposited on the Inside Surface Tubing. *ACS Polym. Prepr.* **1986**, 27, p. 82–84.

(31) Hollander, A.; Thome, J. in *Plasma Polymer Films*; Biederman, H., Ed.; Imperial College Press, London, 2004; p 260–275.

(32) Hofmann, S. Instrumentation. In *Auger- and X-Ray Photoelectron Spectroscopy in Materials* Science*. A User-Oriented Guide*; Springer Series in Surface Science 49; Springer-Verlag: Berlin, 2013; pp 18–19.

(33) Bemson, G.; Briggs, D. *High Resolution XPS of Organic Polymers: The Scienta ESCA300 Database*; John Wiley and Sons: Chichester, England, 1992.

(34) Smith, M. B.; March, J. March's Advanced Organic Chemistry: Reactions, Mechanisms, and Structure; Wiley & Sons, Inc.: Canada.

(35) Carey, F. A.; Sundberg, R. J. Photochemistry. In *Advanced Organic Chemistry Part A: Structure and Mechanisms*, 5th Ed.; Springer: New York, 2007.

(36) Loyer, F.; Bengasi, G.; Franche, G.; Choquet, P.; Boscher, N. Insights in the Initiation and Termination of Poly (Alkyl Acrylates) Synthetized by Atmospheric Pressure Plasma-Initiated Chemical Vapor Deposition (AP-PiCVD). *Plasma Process. Polym.* **2018**, *15*, e1800027.

(37) Bellamy, L. J. *The Infra-Red Spectra of Complex Molecules*; Vol. 2; Chapman and Hall Ltd.: London, 1975.

(38) Phillipson, K.; Jenkins, M, J.; Hay, J. N. The Kinetics of Crystallization of Poly(ε-Caprolactone) Measured by FTIR Spectroscopy. *J. Therm. Anal. Calorim.* **2016**, *123*, 1491–1500.

(39) Morosoff, N. An Introduction to Plasma Polymerization. In *Plasma Deposition, Treatment, and Etching of Polymers*; d'Agostino, R. Ed.; Academic Press, Inc.; United States of America, 1990.

(40) Hudis, M. Surface Crosslinking of Polyethylene Using a Hydrogen Glow Discharge. *J. Appl. Polym. Sci.* **1972**, *16*, 2397–2415.

(41)Tajima, S.; Komvopoulos, K. Effect of Reactive Species on Surface Crosslinking of Plasma-Treated Polymers Investigated by Surface Force Microscopy. *Appl. Phys. Lett.* **2006**, *89*, 124102.

(42)Lin-Vien, D.; Colthup, N. B.; Fateley, W. G.; Grasselli, J. G. *The Handbook of Infrared and Raman Characteristic Frequencies of Organic Molecules*; Academic Press, Inc.: San Diego, 1991.

(43) Bellamy, L. J. *The Infra-Red Spectra of Complex Molecules*; Vol. 2; Chapman and Hall Ltd.: London, 1975.

(44) Gan, Y.; Yin, J.; Jiang, X. Self-Wrinkling Induced by the Photopolymerization and Self-Assembly of Fluorinated Polymer at Air / Liquid Interface. *J. Mater. Chem. A* **2014**, *2*, 18574–18582.

(45) Samyn, P.; Laborie, M.-P.; Mathew, A. P.; Airoudj, A.; Haidara, H.; Roucoules, V. Metastable Pattering of Plasma Nanocomposite Films by Incorporating Cellulose Nanowhiskers. *Langmuir* **2012**, *28*, 1427–1438.

(46) Thirty, D.; Vinx, N.; Damman, P.; Aparicio, F. J.; Tiesser, P.-Y.; Moerman, D.; Leclere, P.; Godfroid, T.; Deprez, S.; Snyders, R. The Wrinkling Concept Applied to Plasma-Deposited Polymer-Like Thin Films: A Promising Method for the Fabrication of Flexible Electrodes. *Plasma Polym. Process.* **2020**, e2000119.

(47) Bardon, J.; Martin, A.; Fioux, P.; Amari, T.; Mertz, G.; Delmee, M.; Ruch, D.; Roucoules, V. Reinforcement of a Docecylacrylate Plasma Polymer by Admixture of a Diacrylate or a Dimethacrylate Cross-Linker. *Plasma Process. Polym.* **2018**, *15*, e1800031.

5. Atomised Spray Plasma Deposition of Superhydrophobic and Wet Electrical Barrier Coatings

5.1 Background and Introduction

The synergetic effect of superhydrophobic and insulating thin films can extend the life of electronic devices (e.g., smartphones, hearing aids, tablets, and so forth) from any damage caused by any contact with moisture or water that can lead to short circuit or corrosion within the circuit boards of electronic devices.[1–5]

Superhydrophobicity was discussed in Chapter 3. There are two mathematical models used to describe the wettability of superhydrophobic surfaces which depend on different criteria: The Cassie–Baxter and the Wenzel models.[6,7,8] The Cassie–Baxter model suggests the reduction of the surface contact area within the liquid–solid interface due to the air pockets trapped into the cavities of the rough surface and the probe liquid and therefore, resulting in lower adhesion and contact angle hysteresis of <10°.[6] On the contrary, the Wenzel model proposes an increase of the surface contact area in the liquid–solid interface and thus resulting in higher adhesion to water.[8] One approach to reduce the surface energy is to employ fluorinated polymeric materials, the low surface energy of fluoro-polymers is ascribed to the closed packed terminal groups $–CF_3$ (6 mN m^{-1}), and $–CF_2–$ (18 mN m^{-1}). Flat surfaces modified with fluorinated materials possess water contact angle values of ~120°.[9] The second approach is by inducing roughness through plasma etching,[10] chemical etching,[11] lithography,[12] surface patterning,[13] or inorganic nanoparticles.[14]

Superhydrophobic coatings can repel water from the surface, and thus preventing the water or oxygen diffusion through the polymeric coatings which may prevent the electrical breakdown of the protective polymer coating or the corrosion of the underlying metal electrode.[15] Additionally, due to the high dielectric strength of the fluoropolymers, [16] they also prevent the electron transport, and thus polymer damage, as discussed in chapter 4.

Different methods have been reported for the deposition of long-chain perfluoroalkyl acrylates (e.g., C_6–C_8 perfluoroalkyl chain length), such as

initiated chemical vapour deposition (iCVD),[17] plasma-enhanced chemical vapour deposition,[18] and pulsed plasma deposition.[19] For instance: Gleason et al.[17] fabricated the preparation of hydrophobic surfaces by depositing perfluorodecyl acrylate using initiated chemical vapour deposition where the filament and the substrate have to be heated to initiate the free radical polymerisation.

Kumar et al.[18,20] prepared liquid-repellent coatings through plasma polymerisation of perfluorodecyl acrylate at low pressure using argon as a carrier gas which also participated in the generation of excited plasma species. In contrast, Mertz et al.[21] introduced the same precursor in the form of droplets into an atmospheric-pressure plasma reactor to fabricate superhydrophobic coatings. Ollgaard et al.[22] deposited perfluorodecyl acrylate using plasma polymerisation at low pressure and variable applied power (i.e., from 1 W/L to 0.1 W/L of applied power) to fabricate hydrophobic surfaces on textiles and electronic devices.

Coulson et al. deposited perfluorodecyl acrylate by gas-phase plasma polymerisation to obtain hydrophobic surfaces in cotton fabrics,[19] footwear,[23] and microfluidic devices,[24] or to obtain wet electrical barrier coatings for electronic devices.[1] Alternatively, Coulson et al.[5,25] deposited shorter perfluoroalkyl chain precursor (perfluorooctyl acrylate) using gas-phase plasma polymerisation to protect electronic devices from the dielectric breakdown in contact with water. Although they observed some drawbacks when obtaining the plasma polymer coatings due to their oiliness, hence, they reported different strategies to overcome this problem, such as using high power and a crosslinking agent—similarly, Legein et al.[26] deposited perfluorooctyl acrylate using gas-phase plasma polymerisation at low pressure to fabricate hydrophobic surfaces on textile materials.

Therefore, in this work, a 20% w/w *1H,1H,2H,2H*-perfluorododecyl acrylate–perfluorotributylamine precursor mixture was atomised into an electricla discharge in combination with a subsequent plasma post-treatment time to yield plasma polymers with high crosslinking degree, and enhanced mechanical and electrical barrier properties, Scheme 5.1.

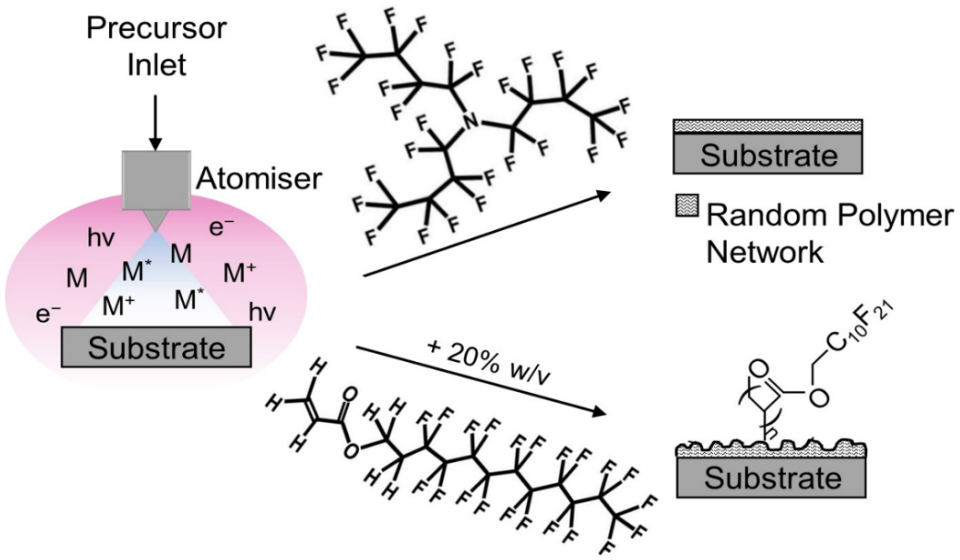

Scheme 5.1: Schematic representation of ASPD 20% w/v *1H,1H,2H,2H*-perfluorododecyl acrylate–perfluorotributylamine coatings.

5.2 Results and Discussion

5.2.1 Atomised Spray Plasma Deposition

Plasma copolymerisation of a mixture of perfluorotributylamine (+99.9%, Fluorinert FC-43, 3M Inc.) and *1H,1H,2H,2H*-perfluorododecyl acrylate (solid at ambient temperature, +98%, Fluorochem Ltd.) was carried out by using the ASPD. These two perfluorinated precursors were chosen because perfluorinated precursors have the lowest surface tension, and the number of —CF_3 present in the perfluorotributylamine precursor. Additionally, *1H,1H,2H,2H*-perfluorododecyl acrylate has a polymerizable functional group which is expected to give rise to the deposition rate. The ASPD was carried out at the optimum condition of 20% w/v *1H,1H,2H,2H*-perfluorododecyl acrylate–perfluorotributylamine slurry solution[27] (30 W, flow rate of 14 ± 2 x 10^{-4} mL s^{-1}). The resulting plasma polymer coatings showed superhydrophobic and oleophobic behaviour with enhanced mechanical and wet electrical barrier properties for the plasma post-treated polymer coatings.

It is likely that the plasma polymerization mechanism depends on the radical and ion formation from both precursors. It is suggested that during the ASPD, the radical polymerization starts with the *1H,1H,2H,2H*-

perfluorododecyl acrylate monomer due to the unsaturated vinyl group. There are also electron impacts within the plasma resulting in the fragmentation and radical formation of the perfluorotributylamine. These radicals can then initiate polymerisation of the *1H,1H,2H,2H*-perfluorododecyl acrylate monomer leading to the conventional free radical polymerisation through the vinyl group. As the reactive plasma species, mainly vacuum UV photons, promote the radical formation, fragmentation, and crosslinking of the plasma polymers,[28] plasma post-treatment was proposed to carry out on the ASPD 20% w/v *1H,1H,2H,2H*-perfluorododecyl acrylate–perfluorotributylamine coatings due to the continuous plasma polymerisation and crosslinking of the polymer and the monomer molecule reduction in the gas phase. Therefore, this increases the applied energy (W) per molecule as described by the Yasuda parameter (W/FM: where F is the flow rate, and M the molecular weight of the precursor)[29] in both, the plasma phase and the polymer surface. Alternatively, it has been reported that to achieve a higher crosslinking degree of plasma polymers or to avoid the oiliness of the plasma polymer coatings, high applied power either in continuous or pulsed mode plasmas,[1,5] or crosslinking agents[30] are required.

5.2.2 Deposition rate

The deposition rate of ASPD perfluorotributylamine layer was 49 ± 4 nm min^{-1} as reported in Chapter 3.

Dissolving solid *1H,1H,2H,2H*-perfluorododecyl acrylate into perfluorotributylamine to form a 20% w/v solution mixture enhanced the ASPD deposition rate by a factor of 13, up to 640 ± 315 nm min^{-1} (precursor flow rate = 14 ± 2 x 10^{-4} mL s^{-1}) which can be attributed to the reactivity of the acrylate functional group. Therefore, the deposition rate and deposition time can be adjusted to obtain the optimum ASPD coating thickness. Similarly, other studies deposited shorter perfluoroalkyl chain poly(*1H,1H,2H,2H*-perfluorodecyl acrylate, PFAC-8) films, where they reported deposition rate values of: 275 nm min^{-1} by initiated chemical vapour deposition (iCVD),[17] ~15

nm min^{-1} by plasma-enhanced chemical vapour deposition,[18] and ~10 nm min^{-1} by pulsed plasma polymerisation.[19]

5.2.3 X-ray Photoelectron Spectroscopy

XPS analysis of the ASPD perfluorotributylamine coating showed evidence of only carbon, fluorine, and nitrogen as reported in Chapter 3. On the other hand, carbon, fluorine, nitrogen, and oxygen were detected for the ASPD 20% w/v *1H,1H,2H,2H*-perfluorododecyl acrylate–perfluorotributylamine coatings, Figure 5.1, and Table 5.1. In this case, the elemental atomic composition of the ASPD 20% w/v *1H,1H,2H,2H*-perfluorododecyl acrylate–perfluorotributylamine coatings did not change at any condition of plasma post-treatment which suggests that no defluorination/material removal via etching/ablation process occurs by exposing the ASPD plasma polymer directly to the reactive plasma species during plasma post-treatment, Table 5.1.

The C(1s) XPS spectra of ASPD perfluorotributylamine coating were fitted to five Gaussian Mg $K\alpha_{1,2}$ components in conjunction with their corresponding Mg $K\alpha_3$ and Mg $K\alpha_4$ satellite peaks towards lower binding energy by ~8.4 and ~10.2 eV respectively, Figure 5.2.[31] The C(1s) Mg $K\alpha_{1,2}$ components being: –<u>C</u>–CF_n at 286.1 eV, –<u>C</u>F– at 287.5 eV, –<u>C</u>F–CF_n at 289.2 eV, –<u>C</u>F_2– at 291.2 eV, and –<u>C</u>F_3 at 293.1 eV.[32] At 12 min of plasma post-treatment of the ASPD perfluorotributylamine coating, the unsaturated and crosslinked carbon centre (%[–<u>C</u>–CF_n] + %[–<u>C</u>F–] + %[–<u>C</u>F–CF_n]) increased from ~35% to ~55% of the total atomic carbon composition indicating a higher crosslinking degree of the ASPD perfluorotributylamine coating.

The C(1s) XPS spectra of ASPD 20% w/v *1H,1H,2H,2H*-perfluorododecyl acrylate–perfluorotributylamine coating were fitted to six Gaussian Mg $K\alpha_{1,2}$ components in conjunction with their corresponding Mg $K\alpha_3$ and Mg $K\alpha_4$ satellite peaks towards lower binding energies by ~8.4 and ~10.2 eV respectively, Figure 5.2.[31] The C(1s) Mg $K\alpha_{1,2}$ components being: –<u>C</u>–C– / <u>C</u>$_x$H$_y$ at 285.0 eV, –<u>C</u>–CF_n / –<u>C</u>–O at 286.3 eV, –<u>C</u>F– at 287.8 eV, –<u>C</u>F–CF_n / O–<u>C</u>=O at 289.5 eV, –<u>C</u>F_2– at 291.2 eV, and –<u>C</u>F_3 at 293.2 eV.[32]

The oxygenated or hydrogenated carbon functionalities are originated from the acrylate group within the *1H,1H,2H,2H*-perfluorododecyl acrylate. Upon optimum 12 min of plasma post-treatment of the ASPD 20% w/v *1H,1H,2H,2H*-perfluorododecyl acrylate–perfluorotributylamine coatings, the retention of the [–$\underline{C}F_2$–] component is reduced by ~10 at.%. Consequently, the unsaturated and crosslinked carbon centres ([–$\underline{C}$–CF_n / –$\underline{C}$–O] + [–$\underline{C}$F–] + [–$\underline{C}$F–CF_n / O–$\underline{C}$=O]) increased from ~25% to ~39% of the total atomic carbon composition attributed to a higher crosslinking of the ASPD plasma polymers which were longer exposed to the excited species after ceasing the atomised spray plasma deposition. This higher crosslinked degree confirmed the effect of the interaction among the reactive plasma species during the plasma post-treatment of the plasma polymer coatings.

The single F(1s) XPS Mg $K\alpha_{1,2}$ peak at 687.9 eV corresponds to a covalently bonded fluorine atoms, Figure 5.3. The fluorine elemental atom composition and the F:C ratio remained stable upon plasma post-treatment, which means that defluorination via etching process did not take place, Table 5.1.

The O(1s) Mg $K\alpha_{1,2}$ components being: C=$\underline{O}$ at 531.3 eV, and C–$\underline{O}$–C at 533.0 eV were shifted to 532.4 eV and 533.8 eV upon 12 min of plasma post-treatment, respectively and represent ca. 3 at.% of the total atomic composition, Table 5.1 and Figure 5.3. This shift of the O(1s) levels towards higher binding energies indicates a change in the chemical and electronic bonding environment.[33]

Therefore, the plasma post-treatment did not affect the elemental composition of the ASPD 20% w/v *1H,1H,2H,2H*-perfluorododecyl acrylate–perfluorotributylamine coatings. Instead, an increase of the unsaturated and crosslinked carbon centre was observed as a function of the plasma post-treatment time.

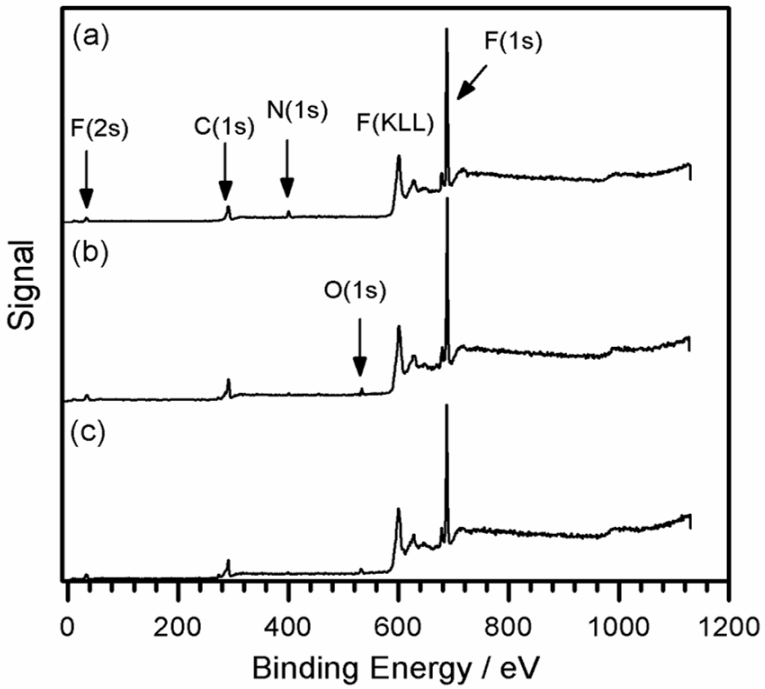

Figure 5.1: Wide scan XPS spectra of: (a) ASPD perfluorotributylamine coating, and ASPD 20% w/v *1H,1H,2H,2H*-perfluorododecyl acrylate–perfluorotributylamine coatings at (b) 0 min and (c) 12 min plasma post-treatment times.

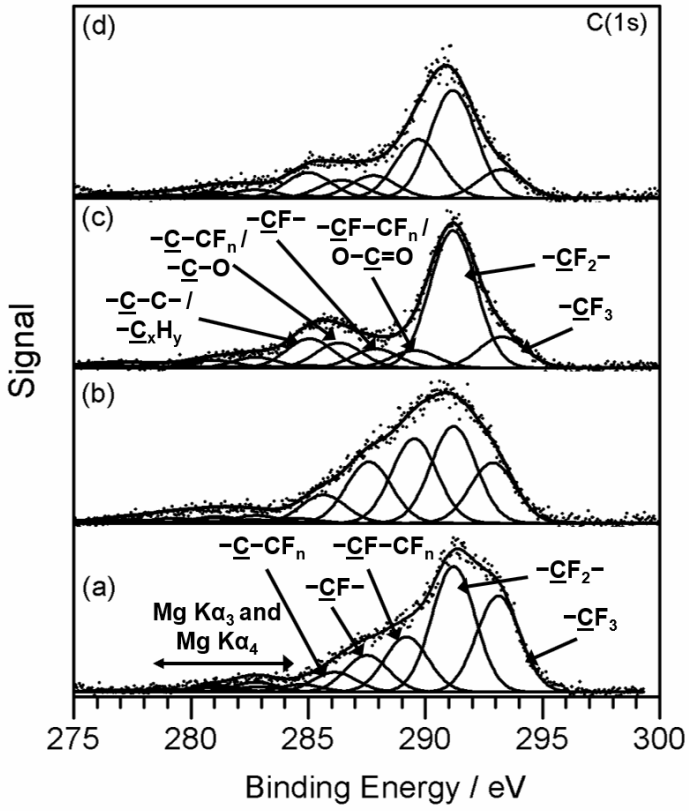

Figure 5.2: C(1s) XPS spectra of: ASPD perfluorotributylamine coating at different plasma post-treatment times: (a) 0 min and (b) 12 min; and ASPD 20% w/v *1H,1H,2H,2H*-perfluorododecyl acrylate–perfluorotributylamine coatings at different plasma post-treatment times: (c) 0 min and (d) 12 min.

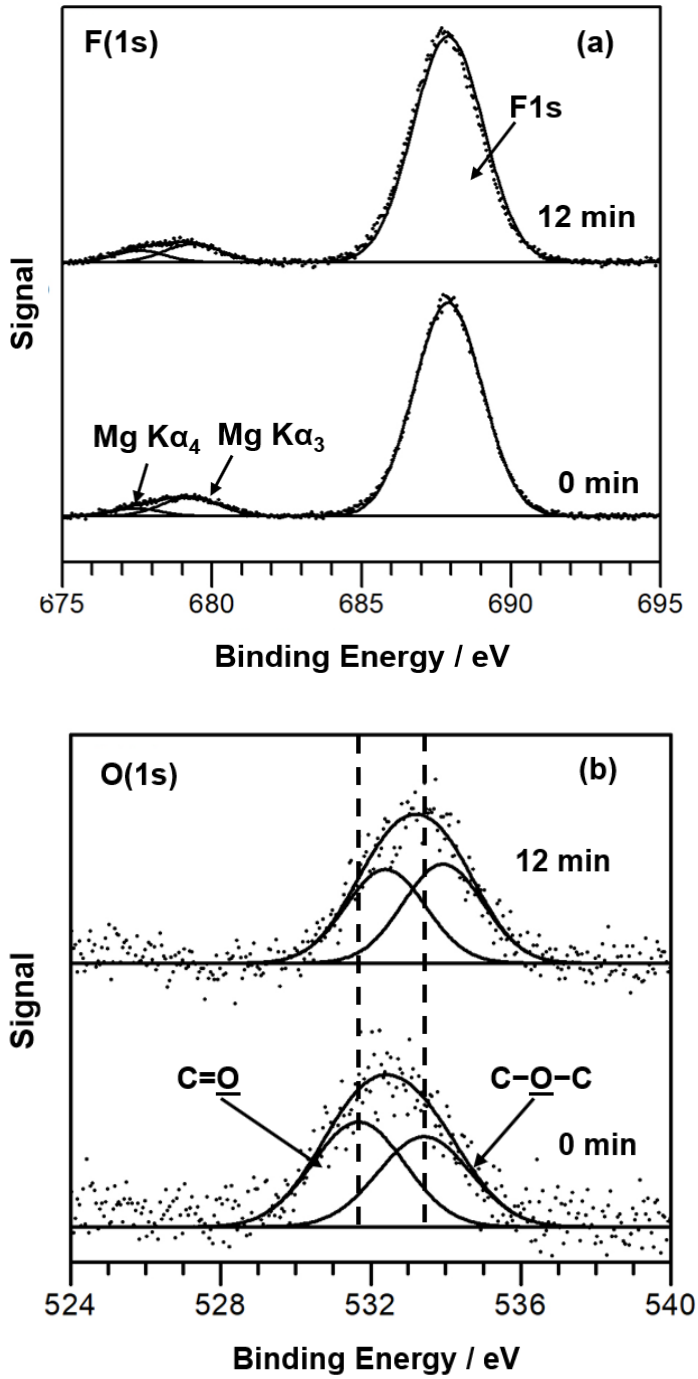

Figure 5.3: (a) F(1s) and (b) O(1s) XPS spectra of ASPD 20% w/v *1H,1H,2H,2H*-perfluorododecyl acrylate–perfluorotributylamine coatings at different plasma post-treatment times. Oxygen component is absent in the ASPD perflurotributylamine coatings, Table 5.1.

Table 5.1: XPS compositions for precursors (theoretical) and ASPD 20% w/v *1H,1H,2H,2H*-perfluorododecyl acrylate–perfluorotributylamine coatings treated at different plasma post-treatment times.

System / Plasma Post-treatment Time	Atomic Composition / %				F:C Ratio	C(1s) Component / %					
	C	F	N	O		C–C / C_xH_y	–C–CF_n / C–O	–CF–	–CF–CF_n–O–C=O	–CF_2–	–CF_3
Perfluorotributylamine precursor	30	67.5	2.5	NA	2.25	NA	NA	NA	NA	75	25
1H,1H,2H,2H-perfluorododecyl acrylate precursor	39.5	55.3	NA	5.3	1.4	33.3	NA	NA	NA	60	6.7
ASPD perfluorotributylamine / 0 min	34.9 ± 0.2	58.2 ± 0.0	6.9 ± 0.2	0.0 ± 0.0	1.7 ± 0.0	NA	7.3 ± 1.8	11.0 ± 0.0	16.7 ± 0.2	36.9 ± 1.1	28.1 ± 0.9
ASPD perfluorotributylamine / 12 min	36.2 ± 0.7	58.4 ± 0.6	5.4 ± 0.3	0.0 ± 0.0	1.6 ± 0.0	NA	10.3 ± 1.5	18.8 ± 1.6	26.1 ± 3.4	25.2 ± 4.4	19.6 ± 2.8
ASPD 20% w/v *1H,1H,2H,2H*-perfluorododecyl acrylate–perfluorotributylamine coating / 0 min	39.0 ± 0.6	56.4 ± 0.5	1.3 ± 0.5	3.3 ± 0.1	1.4 ± 0.1	11.6 ± 1.5	9.8 ± 0.4	6.9 ± 0.5	8.5 ± 2.0	51.7 ± 0.9	11.6 ± 1.0
ASPD 20% w/v *1H,1H,2H,2H*-perfluorododecyl acrylate–perfluorotributylamine coating / 12 min	40.1 ± 1.8	56.0 ± 2.3	0.9 ± 0.6	3.0 ± 0.5	1.4 ± 0.1	8.8 ± 2.4	8.5 ± 2.1	8.9 ± 1.7	22.0 ± 3.6	39.0 ± 4.7	12.8 ± 2.9

5.2.4 Infrared Spectroscopy

The infrared spectrum obtained for the ASPD perfluorotributylamine coating showed characteristic absorbances of perfluorinated chain groups $–CF_2–CF_3$ (1365–1325 cm^{-1}), $–CF_3$ (1350–1120 cm^{-1}) and $–CF_2–$ (1280–1120 cm^{-1}) as indicated in Chapter 3, Figure 5.4 and Table 5.2.[34]

The infrared spectrum for the ASPD 20% w/v *1H,1H,2H,2H*-perfluorododecyl acrylate–perfluorotributylamine coating exhibits a weak absorbance peak at 2965–2895 cm^{-1} associated CH_2 stretching found in polymer backbones[35] (this is absent in the infrared spectrum of *1H,1H,2H,2H*-perfluorododecyl acrylate monomer and can be attributed to the polymerisation of acrylate carbon–carbon double bonds to form saturated carbons), Figure 5.4 and Table 5.2, which is in accordance with the appearance or increase of infrared peak intensity of this saturated carbon after plasma polymerisation reported for other acrylate precursors.[36,37] Characteristic broad bands corresponding to perfluorinated chain groups include $–CF_2–CF_3$ (1365–1325 cm^{-1}), $–CF_3$ (1350–1120 cm^{-1}), and $–CF_2–$ (1280–1020 cm^{-1}) indicating the retention of the perfluorocarbon chains. The infrared band associated with the C–O stretching (1300–1000 cm^{-1}) overlaps with the C–F stretching (1000–900 cm^{-1}) band which limits the interpretation of the infrared spectra. The characteristic acrylate carbonyl C=O absorption at 1731 cm^{-1} is still visible after atomised spray plasma deposition.

The characteristic acrylate C=C double bond absorbance at 1640 cm^{-1} following ASPD, is indistinguishable due to the broadening of acrylate carbonyl group C=O band as well as overlap with the –CF=CF– stretching from the ASPD perfluorotributylamine, Figure 5.5. However, it may be that some non-polymerised *1H,1H,2H,2H*-perfluorododecyl acrylate C=C double bonds are retained in the ASPD of 20% w/v *1H,1H,2H,2H*-perfluorododecyl acrylate–perfluorotributylamine coating.

Upon plasma post-treatment, the characteristic acrylate carbonyl C=O absorption was slightly shifted from 1731 cm^{-1} to 1736 cm^{-1}, Figure 5.5, which may be due to the changes in the neighbouring carbon.[39] This infrared band also reduces in intensity and broadens as a consequence of plasma excited species creating crosslinking and plasma polymer structural rearrangement due to ion bombardment and vacuum–UV irradiation[38] which is also consistent with the higher unsaturated and crosslinked carbon centres and the shift to higher binding energies of the O(1s) XPS components due to a change of the electronic bonding environment, (Chapter 4: Figure 4.3; XPS O(1s) of ASPD IDA), and the infrared absorption shift of the C=O group of the plasma post-

treatment of ASPD poly (isodecyl acrylate) coatings, (Chapter 4: Figure 4.5: IR spectra of C=O).

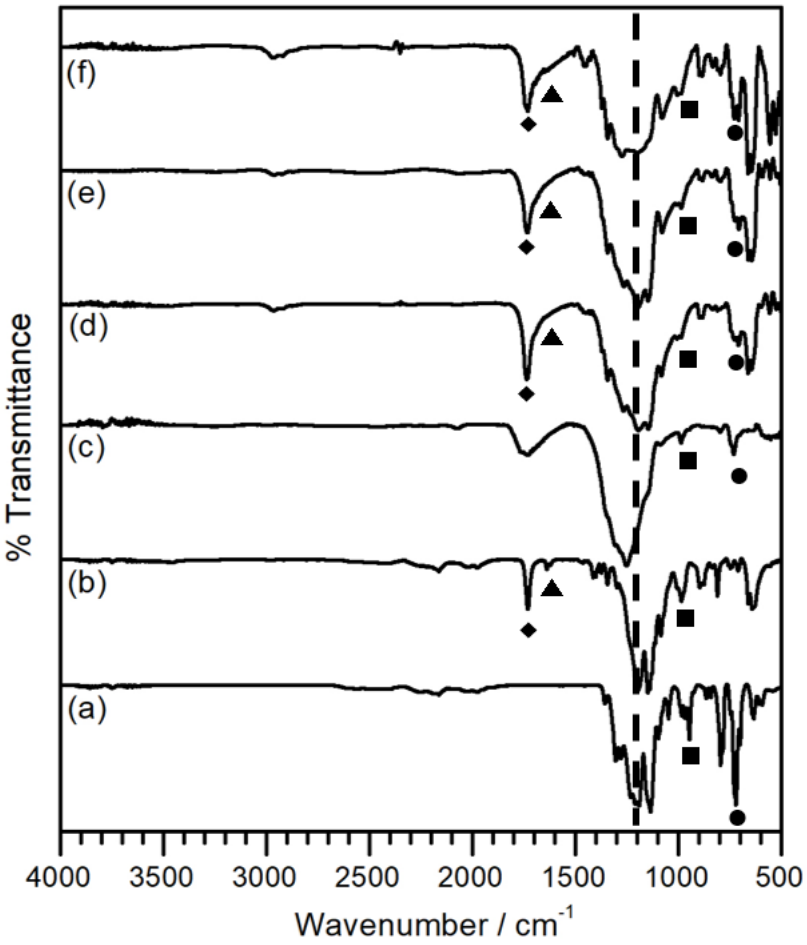

Figure 5.4: Infrared spectra: (a) ATR perfluorotributylamine; (b) ATR *1H,1H,2H,2H*-perfluorododecyl acrylate; (c) RAIRS ASPD perfluorotributylamine coating; (d) RAIRS ASPD 20% w/v *1H,1H,2H,2H*-perfluorododecyl acrylate–perfluorotributylamine coating (no plasma post-treatment); (e) RAIRS ASPD 20% w/v *1H,1H,2H,2H*-perfluorododecyl acrylate–perfluorotributylamine coating (2 min plasma post-treatment); and (f) RAIRS ASPD 20% w/v *1H,1H,2H,2H*-perfluorododecyl acrylate–perfluorotributylamine coating (12 min plasma post-treatment). ◆ C=O stretch (1731 cm^{-1}), ▲ C=C stretch (1640 cm^{-1}), dashed line indicates perfluorinated chain region (1365–1120 cm^{-1}), ■ CF_3 stretch (980 cm^{-1}), ● C–F stretch (720 cm^{-1}).

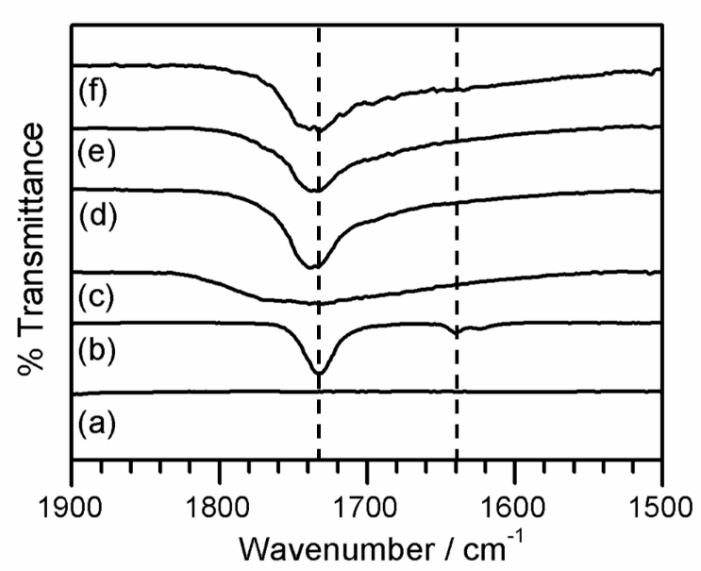

Figure 5.5: Infrared spectra of the carbonyl functional group region: (a) ATR perfluorotributylamine; (b) ATR *1H,1H,2H,2H*-perfluorododecyl acrylate; (c) RAIRS ASPD perfluorotributylamine coating; (d) RAIRS ASPD 20% w/v *1H,1H,2H,2H*-perfluorododecyl acrylate–perfluorotributylamine coating (no plasma post-treatment); (e) RAIRS ASPD 20% w/v *1H,1H,2H,2H*-perfluorododecyl acrylate–perfluorotributylamine coating (2 min plasma post-treatment); and (f) RAIRS ASPD 20% w/v *1H,1H,2H,2H*-perfluorododecyl acrylate–perfluorotributylamine coating (12 min plasma post-treatment). Dashed lines indicate C=O stretch (1731 cm^{-1}), and C=C stretch (1640 cm^{-1}).

Table 5.2: Infrared assignments for perfluorotributylamine precursor and ASPD polymer coatings.[39–41]

Absorption frequency / cm^{-1}	**Assignment**
2965–2895	CH_2 stretching
1731	C=O stretching
1730	–CF=CF– stretching
1640	C=C stretching
1470–1340	CH_2 bending
1420–1410	$=CH_2$ stretching
1365–1325	CF_2–CF_3 stretching
1350–1120	$–CF_3$ antisymmetric stretching
1280–1120	$–CF_2–$ stretching
1250–1020	C–N antisymmetric stretching
1100–900	C–F stretching
1300–1000	C–O acrylate stretching
995–985	$=CH_2$ bending
980	$–CF_3$ symmetric stretching
915–590	$=CH_2$ bending
720	C–F stretching

5.2.5 Scanning Electron Microscopy

SEM images of the surface topography of the ASPD perfluorotributylamine coatings showed a smooth nanocoating, Figure 5.6. The mixing of 20% w/v *1H,1H,2H,2H*-perfluorododecyl acrylate into the ASPD perfluorotributylamine coatings resulted in a roughened surface containing microsphere-like features which can be attributed to: (i) either phase separation of the liquid droplets during the polymerisation or enhanced viscosity (change of the physicochemical properties) due to the optimum 20% w/v *1H,1H,2H,2H*-perfluorododecyl acrylate component during atomisation into the plasma, and (ii) formation of oligomers on the droplet surface during the atomisation before striking the sample surface. For comparison, Mertz et al.[21] used plasma

copolymerisation to fabricate superhydrophobic polymer coatings using two different acrylate precursors which resulted in in similar roughness—particle-like polymer coatings. In contrast, the ASPD poly (isodecyl acrylate) coatings reported in Section 4.2.4 formed a smooth polymer surface prior to the plasma post-treatment, and showed denser wrinkling formation as a function of the plasma post-treatment time—a single precursor—instead of microsphere-like features reported in this Section—two perfluorinated precursors were used with different relative polymerization rate.

The plasma post-treatment of the ASPD 20% w/v *1H,1H,2H,2H*-perfluorododecyl acrylate–perfluorotributylamine coatings led to the shrinkage of the microsphere-like plasma polymer which can be associated to a further plasma exposition (mainly, vacuum UV, radicals, and ion bombardment) generating plasma polymer coatings with a higher crosslinking degree, Figure 5.6. Consequently, after plasma post-treatment, the ASPD plasma polymer shows a change of surface morphology which can be correlated to the increase of crosslinked carbon centre detected by XPS and the broadening of the acrylate carbonyl group showed by IR analysis, Table 5.1, Figure 5.2, and Figure 5.4.

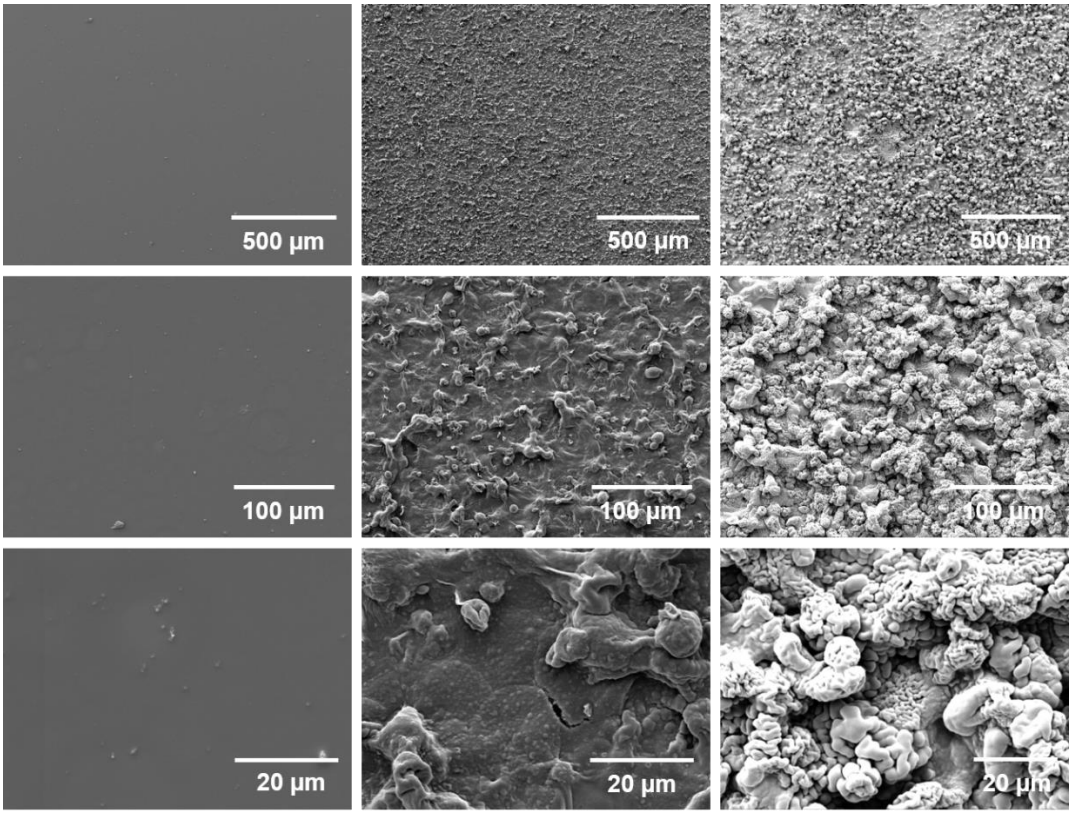

Figure 5.6: SEM images of: ASPD perfluorotributylamine coatings (left column); 0 min plasma post-treated ASPD 20% w/v *1H,1H,2H,2H*-perfluorododecyl acrylate–perfluorotributylamine coatings (middle column); 12 min plasma post-treated ASPD 20% w/v *1H,1H,2H,2H*-perfluorododecyl acrylate–perfluorotributylamine coatings (right column).

5.2.6 Contact Angle

The water contact angle of ASPD perfluorotributylamine coatings is 112 ± 1° as reported in Chapter 3. The wettability of the ASPD perfluorotributylamine coatings did not change either with the effect of the plasma post-treatment time or with the concentration of the $–CF_2–$ and $–CF_3$ functionalities, as indicated by the XPS analysis, Table 5.1, even though the contact angle technique is very susceptible to changes of chemical composition and morphology at the monolayer order.[42]

Incorporation of optimum 20% w/v *1H,1H,2H,2H*-perfluorododecyl acrylate into the ASPD perfluorotributylamine coatings resulted in a roughened surface which can be attributed to the phase separation during the atomisation, Figure 5.6. Consequently, this leads to an increment in liquid repellency with water and hexadecane contact angle values (169° ± 3° and 104° ± 5° for as-deposited, respectively). Similarly, 12 min plasma post-

treatment time of the ASPD 20% w/v *1H,1H,2H,2H*-perfluorododecyl acrylate–perfluorotributylamine coatings did not show any significant change in the water and hexadecane contact angle values and were stable towards polar / non-polar solvent rising, Figure 5.7. Comparatively, other studies[19,20,21] also showed water contact angle values between 120°–160° unlike the ~170° reported in this work, Figure 5.7.

The combination of the micro-scale roughness and the chemical composition led to reduction of surface free energy giving a rise of water and oil contact angle values which can be attributed to the entrapped air pockets reducing the interaction of contact lines between the liquid droplet and the solid surface which is in accordance with the Cassie–Baxter model.[6] Typically, in this model, it is considered a water contact angle hysteresis of <10°. However, for higher contact angle hysteresis values, a transition to the Wenzel model is suggested. Then, in this work, the water contact angle hysteresis for the optimum plasma post-treated ASPD 20% w/v *1H,1H,2H,2H*-perfluorododecyl acrylate–perfluorotributylamine coatings is 11° ± 5° after rinsing with polar / non-polar solvents; thus, it may be possible that this transition to the Wenzel model is potentially present on the surface of the optimised ASPD polymer coatings.

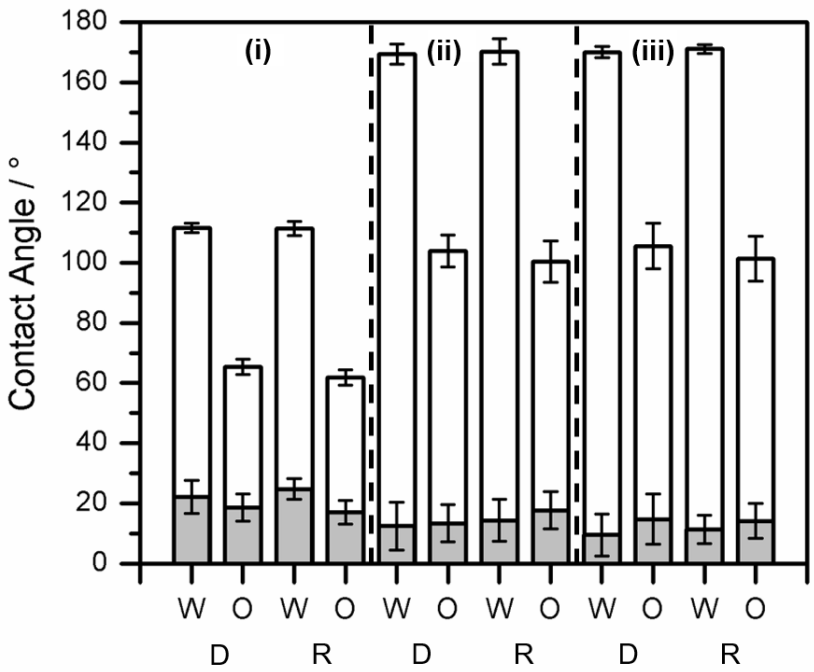

Figure 5.7: Static (open) and hysteresis (shaded) contact angle values using water (W) and hexadecane (O): (i) ASPD perfluorotributylamine coatings; (ii) ASPD 20% w/v *1H,1H,2H,2H*-perfluorododecyl acrylate–perfluorotributylamine coatings (0 min plasma post-treatment); (iii) ASPD 20% w/v *1H,1H,2H,2H*-perfluorododecyl acrylate–perfluorotributylamine coatings (12 min plasma post-treatment): as-deposited (D); and rinsed (R) with propan-2-ol / cyclohexane 1/1 %v/v solution for 1 min. Contact angles using perfluorotributylamine as a probe liquid gave values of < 5° for any plasma polymer coating. 12 min plasma post-treatment of ASPD perfluorotributylamine coatings displayed no changes in the liquid contact angle values.

5.2.7 Microindentation

Microindentation Vickers hardness of ASPD coatings was investigated as a function of the applied load, Figure 5.8(a). ASPD perfluorotributylamine coatings showed ~6-fold harder coatings compared to the ASPD 20% w/v *1H,1H,2H,2H*-perfluorododecyl acrylate–perfluorotributylamine coatings (without plasma post-treatment) at an applied force of 0.49 N.

The mechanical properties of the ASPD 20% w/v *1H,1H,2H,2H*-perfluorododecyl acrylate–perfluorotributylamine coatings were controlled and enhanced by exposing ASPD plasma polymer coatings to plasma after ceasing the atomisation. For the optimum 12 min of plasma post-treatment of the ASPD 20% w/v *1H,1H,2H,2H*-perfluorododecyl acrylate–perfluorotributylamine coatings, the Vickers hardness increased ~10-fold as

compared with those without plasma post-treatment, Figure 5.8(b). Therefore, although the effect of plasma post-treatment did not show any significant change of the liquid repellency, this effect showed enhanced mechanical properties which can be indirectly related to a higher crosslinking density of the plasma polymer upon plasma post-treatment which is also in agreement with the XPS results, Figure 5.2 and Table 5.1.

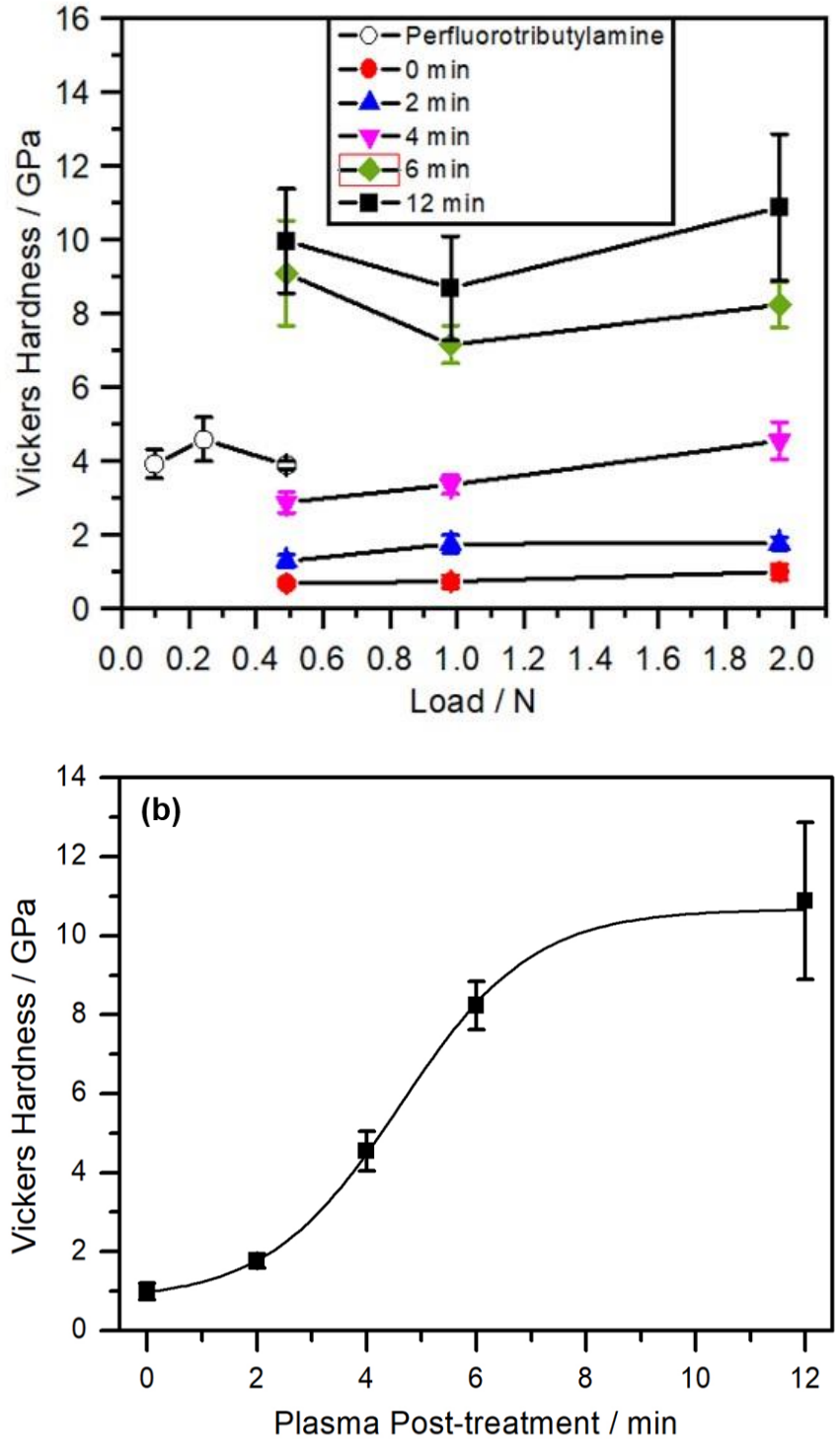

Figure 5.8: (a) Microindentation Vickers hardness as a function of the applied loads for (○) ASPD perfluorotributylamine coating, and ASPD 20% w/v *1H,1H,2H,2H*-perfluorododecyl acrylate–perfluorotributylamine coatings as a function of plasma post-treatment time: (●) 0 min; (▲) 2 min; (▼) 4 min; (◆) 6 min, and (■) 12 min. (b) Microindentation Vickers hardness as a function of plasma post-treatment time of ASPD 20% w/v *1H,1H,2H,2H*-perfluorododecyl acrylate–perfluorotributylamine coatings at an applied force of 1.96 N.

Table 5.3: Microindentation Vickers hardness of ASPD 20% w/v *1H,1H,2H,2H*-perfluorododecyl acrylate–perfluorotributylamine coatings at different plasma post-treatment times.

Coating / Plasma Post-treatment Time	**Vickers Hardness / GPa**				
	0.10 N	**0.25 N**	**0.49 N**	**0.98 N**	**1.96 N**
Perfluorotributylamine	3.9 ± 0.4	4.6 ± 0.6	3.9 ± 0.1	NA	NA
20% w/v *1H,1H,2H,2H*-perfluorododecyl acrylate / Perfluorotributylamine, (0 min)	NA	NA	0.7 ± 0.1	0.7 ± 0.2	1.0 ± 0.2
20% w/v *1H,1H,2H,2H*-perfluorododecyl acrylate / Perfluorotributylamine, (2 min)	NA	NA	1.3 ± 0.2	1.8 ± 0.2	1.8 ± 0.2
20% w/v *1H,1H,2H,2H*-perfluorododecyl acrylate / Perfluorotributylamine, (4 min)	NA	NA	2.9 ± 0.3	3.4 ± 0.2	4.5 ± 0.5
20% w/v *1H,1H,2H,2H*-perfluorododecyl acrylate / Perfluorotributylamine, (6 min)	NA	NA	9.1 ± 1.4	7.2 ± 0.5	8.2 ± 0.6
20% w/v *1H,1H,2H,2H*-perfluorododecyl acrylate / Perfluorotributylamine, (12 min)	NA	NA	10.0 ± 1.4	8.7 ± 1.4	10.9 ± 2.0

5.2.8 Electrical Barrier

Atomised spray plasma deposited perfluorotributylamine coatings showed poor electrical barrier performance of $\log_{10}$ (electrical barrier) 3.7 ± 0.03 Ω at an applied electric field of 10 V mm^{-1} (8 V), Table 5.4. In contrast, the incorporation of 20% w/v *1H,1H,2H,2H*-perfluorododecyl acrylate into the ASPD perfluorotributylamine coatings without plasma post-treatment showed an increase of the wet electrical barrier performance up to $\log_{10}$ (electrical barrier) = 8.9 ± 0.02 Ω at the same applied electric field.

At the higher applied electric field of 75 V mm^{-1} (60 V), the highest electrical barrier ($\log_{10}$ (electrical barrier) = 9.8 ± 0.04 Ω) was found for those ASPD 20% w/v *1H,1H,2H,2H*-perfluorododecyl acrylate–perfluorotributylamine coatings with more than 2 min of plasma post-treatment with a sufficient plasma polymer coating thickness of 3.8 ± 1.9 µm, Figure 5.9. In contrast, the electrical barrier performance decayed ~4 orders of magnitude in the absence of the plasma post-treatment of the ASPD 20% w/v *1H,1H,2H,2H*-perfluorododecyl acrylate–perfluorotributylamine coatings. Therefore, plasma post-treatment of ASPD 20% w/v *1H,1H,2H,2H*-perfluorododecyl acrylate–perfluorotributylamine coated microcircuit boards provide with excellent wet electrical barrier for up to applied electric fields of 75 V mm^{-1} (60 V) that can be used as a protective barrier coating for a range of electronic devices using DC battery voltage up to 24 V.[43]

Therefore, the improved wet electrical barrier performance can be attributed to (i) the effective plasma polymer coating thickness, (ii) the low polarizability of the perfluorinated plasma polymer coatings, (iii) the superhydrophobic properties, Figure 5.7, and (iv) a higher crosslinking degree of the plasma post-treated ASPD polymer coatings as it is shown by the XPS results (i.e., at optimum 12 min of plasma post-treatment), Figure 5.2 and Table 5.1. Particularly, the higher crosslinking degree of the ASPD 20% w/v *1H,1H,2H,2H*-perfluorododecyl acrylate–perfluorotributylamine coatings resulted in enhanced electrical barrier coatings resisting applied electric fields up to 75 V mm^{-1}, acting as a physical barrier to the electron transport from the

anode to the cathode, and thus preventing the electrical breakdown, polymer degradation, corrosion formation, and water diffusion.

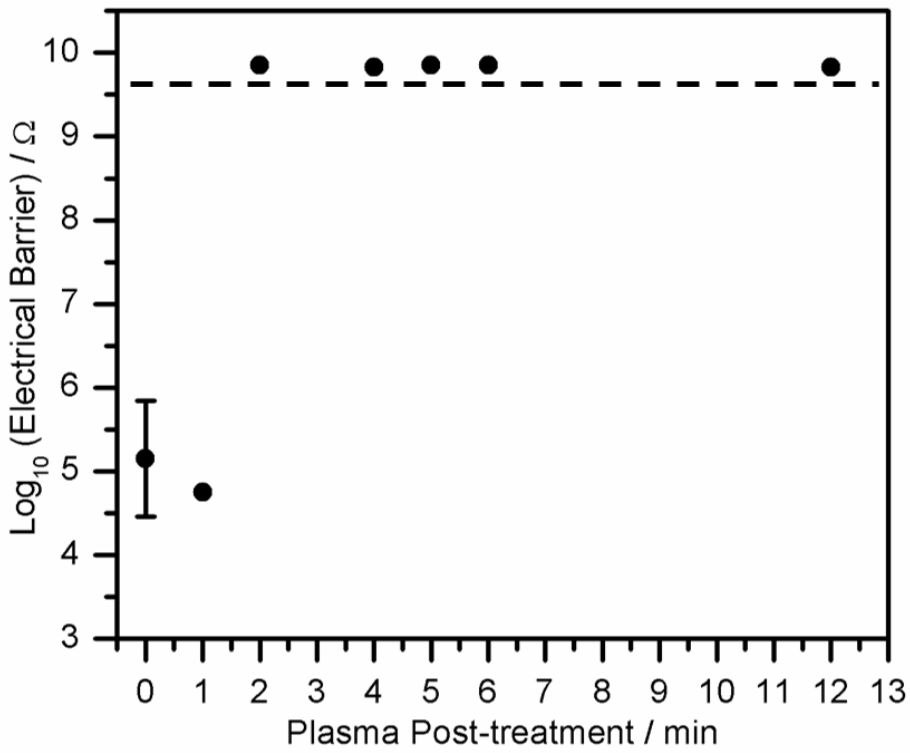

Figure 5.9: Wet electrical barrier as a function of the plasma post-treatment time of ASPD 20% w/v *1H,1H,2H,2H*-perfluorododecyl acrylate–perfluorotributylamine coatings (thickness: 3.8 ± 1.9 µm). Plasma polymer-coated samples were immersed in water for 13 min under an applied electric field of 75 V mm^{-1} (60 V). Samples above the dashed line reached the instrument detection limit of 8 x 10^8 Ω. For all plasma post-treated ASPD 20% w/v *1H,1H,2H,2H*-perfluorododecyl acrylate–perfluorotributylamine coatings the standard deviation is Log_{10} < 0.04 Ω.

Table 5.4: Wet electrical barrier performance after 13 min immersion in water under different applied electric fields, for ASPD 20% w/v *1H,1H,2H,2H*-perfluorododecyl acrylate–perfluorotributylamine coatings (thickness: 3.8 ± 1.9 µm) as a function of plasma post-treatment time, Figure 5.9. † Instrument detection limit of 8 x 10^8 Ω.

ASPD Coating / Plasma Post-treatment Time	**Applied Voltage / V**	**Electric Field / V mm^{-1}**	**Log_{10} (Electrical Barrier) / Ω**
Perfluorotributylamine	8	10	3.7 ± 0.03
20% w/v *1H,1H,2H,2H*-perfluorododecyl acrylate–perfluorotributylamine (0 min)	8	10	8.9 ± 0.02†
20% w/v *1H,1H,2H,2H*-perfluorododecyl acrylate–perfluorotributylamine (0 min)	60	75	5.1 ± 0.7
20% w/v *1H,1H,2H,2H*-perfluorododecyl acrylate–perfluorotributylamine (2–12 min)	60	75	9.8 ± 0.04†

Alternatively, different types of wet electrical barrier coatings that have been deposited via chemical vapour deposition, UV polymerisation, nanocasting, pulsed plasma polymerisation and the wet electrical barrier coatings were tested using different electrochemical techniques. It has been reported a variety of film thicknesses which were analysed by using different electrochemical methods, for instance, by carrying out electrical barrier measurements at an applied voltage of 8 V for wet electrical barrier coating thicknesses: 1.5–2.5 µm;[1,2] by electrochemical measurements for corrosion inhibition: 2–15 µm film thick, Table 5.5.[44,45,46]

However, to date, no previous works have been reported the present measurements of electrical barrier coatings under an applied electric field of 75 V mm^{-1} (60 V). In this work, the wet electrical barrier performance of the 12 min plasma post-treated ASPD 20% w/v *1H,1H,2H,2H*-perfluorododecyl acrylate–perfluorotributylamine coated microcircuit boards was of 9.8 x 10^8 Ω at an applied electric field of 75 V mm^{-1} (60 V) as compared to previous electrical barrier polymer coatings which have reported >3 µm of film thickness and an applied electric field of 10 V mm^{-1}, Table 5.5—a sufficiently high electrical resistance to neglect the electron transport between the electrodes, polymer degradation and corrosion.

Table 5.5: Comparison to the prior art of the wet electrical barrier coatings tested at a fixed applied voltage (8 V) and immersed in water for 13 min. † Samples reached the instrument detection limit of 8 x 10^8 Ω. ✱ Coatings tested at an applied voltage (60 V).

Precursor	**Deposition Method**	**Resistance at 8 V for 13 min**	**Film Thickness**	**Ref.**
Parylene	CVD	> 2 x 10^7	> 2.8 µm	1
PFAC-8	Plasma polymerisation	1) ~8.0 x 10^5 2) 1.5 x 10^7 3) > 6 x 10^8	1) ~1.2 µm 2) ~3.7 µm 3) > 2 µm	
Isodecyl acrylate	Plasma polymerisation	1) ~5 x 10^4 2) 1.8 x 10^7 3) 1.4 x 10^{10}	1) ~0.4 µm 2) ~1.1 µm 3) ~1.9 µm	
Vinyl decanoate	Plasma polymerisation	2.3 x 10^8	~2.2 µm	
Tetradecane	Plasma polymerisation	4.7 x 10^7	~1.1 µm	3
• Polyisoprene (base layer) • Allyl mercaptan	Spin coating / Plasma deposition	> 8 x 10^8	~1.5 µm	2
• PFAC-6	Plasma polymerisation	> 9.2 x 10^9	1.45 µm	5

Precursor	Deposition Method	Resistance at 8 V for 13 min	Film Thickness	Ref.
• Divinyl adipate (Crosslinking agent) • Helium				
Isodecyl acrylate	ASPD (12 min plasma post-treatment)	1) > 2.2 x 10^4 2) 1 x 10^8 3) > 6.5 x 10^8 4) > 8.9 x 10^8 †	1) ~0.26 µm 2) ~1.07 µm 3) ~1.2 µm 4) ~1.9 µm †	(Chapter 4: Figure 4.8)
20% w/v (*1H,1H,2H,2H*-perfluorododecyl acrylate–Perfluorotributylamine)	ASPD (No plasma post-treatment)	1) > 8.9 x 10^8 † at 8 V 2) 3.8 x 10^5 at 60 V ✱	3.8 ± 1.9 µm	Figure 5.9
	ASPD (12 min plasma post-treatment)	> 9.8 x 10^8 at 60 V †	3.8 ± 1.9 µm † ✱	

5.3 Conclusions

Superhydrophobic ASPD 20% w/v *1H,1H,2H,2H*-perfluorododecyl acrylate–perfluorotributylamine coatings were prepared to protect micro-circuit boards from the electrical breakdown produced when micro-circuit boards are in contact with water and under an electric field of 75 V mm^{-1}, surpassing the wet electrical barrier performance of previously reported polymer coatings tested up to 10 V mm^{-1}. The wet electrical barrier performance was enhanced by supplying more energy to the ASPD 20% w/v *1H,1H,2H,2H*-perfluorododecyl acrylate–perfluorotributylamine coatings during the plasma post-treatment step increasing the crosslinking density.

On the other hand, XPS analysis confirmed the elemental composition consistency of plasma polymer coatings after plasma post-treatment but higher crosslinking degree was confirmed by infrared, and microindentation analyses. Therefore, the tune of the functional groups could be possible at an optimum plasma post-treatment time. It is then evident that during the plasma post-treatment, the energy of the reactive species is dissipated or transferred to the polymer surface promoting further crosslinking. The best result was for the optimum 12 min plasma post-treated ASPD 20% w/v *1H,1H,2H,2H*-perfluorododecyl acrylate–perfluorotributylamine coatings which increased up to $\log_{10}$ (electrical barrier) = 9.8 ± 0.04 Ω, and ~11 GPa for the wet electical barrier performance under an applied electric field of 75 V mm^{-1}, and Vickers hardness, respectively, as compared to the samples with no plasma post-treatment.

Therefore, the synergetic effect of superhydrophobicity and insulating properties of the 12 min plasma post-treated ASPD 20% w/v *1H,1H,2H,2H*-perfluorododecyl acrylate–perfluorotributylamine coatings significantly improved the wet electrical barrier performance and mechanical properties, without significant variation of the chemical composition of the plasma polymer coatings.

5.4 References

(1) Coulson, S. R.; Evans, D.; Hellwing, T.; Hopper, F.; Poulter, N.; Siokou, A.; Telford, C. Method for Forming a Coating on an Electric or Electrical Device. Patent WO 2016/198855 A1, Dec 15, 2016.

(2) Fraser, R. C.; Carletto, A.; Wilson, M.; Badyal, J. P. S. Plasmachemical Double Click Thiol–ene for Wet Electrical Barrier. *ACS Appl. Mater. Interfaces* **2016**, *8*, 21832–21838.

(3) Coulson, S. R.; Evans, D.; Siokou, A.; Telford, C. Coating. Patent WO 2016/198856, Dec 15, 2016.

(4) Biswas, S.; Shalev, O.; Pipe, K. P.; Shtein, M. Chemical Vapor Jet Deposition of Parylene Polymer Films in Air. *Macromol.* **2015**, *48*, 5550–5556.

(5) Coulson, S.; Evans, D.; Siokou, A.; Telford, C. Coatings. Patent BE1024652B1, May 16, 2018.

(6) Barthlott, W.; Neinhuis, C. Purity of the Sacred Lotus, or Escape from Contamination in Biological Surfaces. *Planta* **1997**, *202*, 1–8.

(7) Cassie, A. B. D.; Baxter, S. Wettability of Porous Surfaces. *Trans. Faraday Soc.* **1944,** *40*, 546–551.

(8) Wenzel, R. N. Resistance of Solid Surfaces to Wetting by Water. *Ind. Eng. Chem.* **1936**, *28*, 988–994.

(9) Nishino, T.; Meguro, M.; Nakamae, K; Matsushita, M.; Ueda, Y. The Lowest Surface Free Energy Based on $-CF_3$ Alignment. *Langmuir* **1999**, *15*, 4321–4323.

(10) Ryu, J.; Kim, K.; Park, J. Y.; Hwang, B. G.; Ko, Y. G.; Kim, H. J.; Han, J. S.; Seo, E. R.; Park, Y, J.; Lee, S. J. Nearly Perfect Durable Superhydrophobic Surfaces Fabricated by a Simple One-Step Plasma Treatment. *Sci. Rep.* **2017**, *7*, 1–8.

(11) Qian, B.; Shen, Z. Fabrication of Superhydrophobic Surfaces by Dislocation-Selective Chemical Etching on Aluminum, Copper, and Zinc Substrates. *Langmuir* **2005**, *21*, 9007–9009.

(12) Shiu, J.-Y.; Kuo, C.-W.; Chen, P.; Mou, C.-Y. Fabrication of Tunable Superhydrophobic Surfaces by Nanosphere Lithography. *Chem. Matter.* **2004**, *16*, 561–564.

(13) Zhai, L.; Berg, M. C.; Cebeci, F. C.; Kim, Y.; Milwid, J. M.; Rubner, M. F.; Cohen, R. E. Patterned Superhydrophobic Surfaces: Toward a Synthetic Mimic of the Namib Desert Beetle. *Nano Lett*. **2006**, *6*, 1213–1217.

(14) Schaeffer, D. A.; Polizos, G.; Smith, D. B.; Lee, D. F.; Hunter, S. R.; Datskos, P. G. Optically Transparent and Environmentally Durable Superhydrophobic Coating Based on Functionalized SiO_2 Nanoparticles. *Nanotechnol.* **2015**, *26*, 1–8.

(15) Zhang, D.; Wang, L.; Qian, H.; Li, X. Superhydrophobic Surfaces for Corrosion Protection: A Review of Recent Progresses and Future Directions. **2016**, *13*, 11–29.

(16) Blythe, T.; Bloor, D. Electrical Properties of Polymers. Cambridge University Press: Cambridge, 2005; pp 27–58, 186–195.

(17) Gupta, M.; Gleason, K. K. Initiated Chemical Vapor Deposition of Poly(*1H,1H,2H,2H*-Perfluorodecyl Acrylate) Thin Films. *Langmuir* **2006**, *22*, 10047–10052.

(18) Kumar, V.; Pulpytel, J.; Rauscher, H.; Mannelli, I.; Rossi, F.; Arefi-Khonsari, F. Fluorocarbon Coatings via Plasma Enhanced Chemical Vapor Deposition of *1H,1H,2H,2H*-Perfluorodecyl Acrylate - 2, Morphology, Wettability and Antifouling Characterization. *Plasma Process. Polym.* **2010**, *7*, 926–938.

(19) Coulson, S. R.; Woodward, I. S.; Badyal, J. P. S.; Brewer, S. A.; Willis, C. Ultralow Surface Energy Plasma Polymer Films. *Chem. Mater.* **2000**, *12*, 2031–2038.

(20) Kumar, V.; Pulpytel, J.; Arefi-Khonsari, F. Fluorocarbon Coatings via Plasma Enhanced Chemical Vapor Deposition of 1H,1H,2H,2H-Perfluorodecyl Acrylate – 1, Spectroscopic Characterization by FT-IR and XPS. *Plasma Process. Polym.* **2010**, *7*, 939–950.

(21) Mertz, G.; Delmee, M., Bardon, J.; Martin, A.; Ruch, D.; Fouquet, T.; Garreau, S.; Airoudj, A.; Marguier, A.; Ploux, L.; Roucoules, V. Atmospheric Pressure Plasma Co-Polymierization of Two Acrylate Precursors: Toward the Control of Wetting Properties. *Plasma Process. Polym.* **2018**, *15*, 1800073.

(22) Ollgaard, M. Method of Coating a Surface with a Water and Oil repellant Polymer Layer. Patent US 2012/0051018 A1, Mar 1, 2012.

(23) Coulson, S. Novel Method. Patent US 2013/0180129 A1, Jul 18, 2013.

(24) Coulson, S. Microfabricated Devices with Coated or Modified Surface and Method of Making Same. Patent US 2012/0258025 A1, Oct 11, 2012.

(25) Coulson, S. R.; Evans, D.; Siokou, A.; Telford, C. Coatings. Patent US 2018/0171171 A1, Jun 21, 2018.

(26) Legein, F.; Rogge, E. Surface Coatings. Patent WO2014056966 A1, April 17, 2014.

(27) Castaneda-Montes, I.; Ritchie, A. W.; Badyal, J. P. S. Atomised Spray Plasma Deposition of Hierarchical Superhydrophobic Nanocomposite Surfaces. *Colloid Surf. A* **2018**, *558*, 192–199.

(28) Hollander, A.; Thome, J. In *Plasma Polymer Films*; Biederman, H., Ed.; Imperial College Press, London, 2004; p 260–275.

(29) Yasuda, H. Plasma Polymerization. Academic Press, Inc.: Missouri, 1985.

(30) Zong, J. Method for Preparing Waterproof and Electric Breakdown-Resistant Coating. Patent WO2018133237A1, July 26, 2018.

(31) Hofmann, S. Instrumentation. *Auger- and X-Ray Photoelectron Spectroscopy in Materials Science. A User-Oriented Guide*; Springer Series in Surface Science 49; Springer-Verlag: Berlin, 2013; pp 18–19.

(32) Bemson, G.; Briggs, D. *High Resolution XPS of Organic Polymers: The Scienta ESCA300 Database*; John Wiley and Sons: Chichester, England, 1992.

(33) Wren, A. W.; Laffir, F. R.; Mellot, N. P.; Towler, M. R. X-Ray Photoelectron Spectroscopy: Studies from Industrial and Bioactive Glass to Biomaterials. In *X-Ray* Photoelectron Spectroscopy*;* Wagner, J. M., Ed.; Nova Science Publishers, Inc.; New York; 2011; pp 1–31.

(34) Lin-Vien, D.; Colthup, N. B.; Fateley, W. G.; Grasselli, J. G. The Handbook of Infrared and Raman Characteristic Frequencies of Organic Molecules; Academic Press, Inc.: San Diego, 1991.

(35) Kutyreva, M. P.; Gataulina, A. R.; Ulakhovich, N. A.; Terekhova, N. V.; Kutyrev, G. A. Synthesis and Spectral Characteristics of 2,2-Bis(Hydroxymethyl)Propionic Acid Derivatives as Model Compounds for the Estimation of Properties of Modified Hyperbranched Polyesters Polyols. *Russ. J. Org. Chem.* **2015**, *51*, 1376–1381.

(36) Loyer, F.; Bengasi, G.; Franche, G.; Choquet, P.; Boscher, N. Insights in the Initiation and Termination of Poly (Alkyl Acrylates) Synthetized by Atmospheric Pressure Plasma-Initiated Chemical Vapor Deposition (AP-PiCVD). *Plasma Process. Polym.* **2018**, *15*, e1800027.

(37) Loyer, F.; Frache, G.; Choquet, P.; Boscher, N. D. Atmospheric Pressure Plasma-Initiated Chemical Vapor Deposition (AP-PiCVD) of Poly(Alkyl Acrylates): An Experimental Study. *Macromol.* **2017**, *50*, 4351–4362.

(38) Yasuda, H. Plasma Polymerization. Academic Press, Inc.: Missouri, 1985.

(39) Bellamy, L. J. The Infra-Red Spectra of Complex Molecules; Vol. 2; Chapman and Hall Ltd.: London, 1975.

(40) Pretsch, E.; Buhlmann, P.; Badertscher, M. Structure Determination of Organic Compounds: Tables of Spectral Data; Springer-Verlag: Berlin, 2009.

(41) Khalil, M. I.; Al-Qunaibit, M. M.; Al-zahem, A. M.; Labis, J. P. Synthesis and Characterization of ZnO Nanoparticles by Thermal Decomposition of a Curcumin Zinc Complex. *Arab. J. Chem.* **2014**, *7*, 1178–1184.

(42) Poynor, A.; Hong, L.; Robinson, I. K.; Granick, S. How Water Meets a Hydrophobic Surface. *Phys. Rev. Lett.* **2006**, *97*, 266101-1– 266101-4.

(43)https://www2.deloitte.com/content/dam/Deloitte/global/Documents/Technology-Media-Telecommunications/gx-tmt-pred15-smartphone-batteries.pdf (Accessed February 05, 2022).

(44) Wang, J.; Pan, T.; Zhang, J.; Xu, X.; Yin, Q.; Han, J.; Wei, M. Hybrid Films with Excellent Oxygen and Water Vapor Barrier Properties as Efficient Anticorrosive Coatings. *RSC Adv.* **2018**, *8*, 21651–21657.

(45) Chang, K.-C.; Ji, W.-F.; Lai, M.-C.; Hsiao, Y.-R.; Hsu, C.-H.; Chuang, T.-L.; Wei, Y.; Yeh, J.-M.; Liu, W.-R. Synergistic Effects of Hydrophobicity and Gas Barrier Properties on the Anticorrosion Property of PMMA Nanocomposite Coatings Embedded with Graphene Nanosheets. *Polym. Chem.* **2014**, *5*, 1049–1056.

(46) Warner, J. C.; Viola, M. S. Protective Barriers for Electronic Devices. Patent US 2013/0056723 A1, Mar 7, 2013.

6. Atomised Spray Plasma Deposition of Antibacterial Coatings

6.1 Background and Introduction

Bacterial biofilm adhesion to surfaces is considered a common problem in the healthcare sector since bacteria are becoming more resistant to antibiotics; bacteria may proliferate in biofilms due to their effective physical protection from antibiotics.[1] Bacterial biofilms can be a source of potential bacterial infections for biomedical devices, material surfaces, food packaging, or water pipes.[2] Therefore, it is important to reduce the bacteria growth and adhesion at initial stages to prevent the bacterial biofilm formation.

Several strategies have been reported to prevent the bacterial biofilm formation on biomaterial surfaces without changing their bulk properties. For instance, antibacterial surfaces can be prepared by surface functionalisation which inhibits the bacteria growth (e.g., surface functionalisation with: poly L-lysine,[3] antibiotic-ampicillin,[4] amine functional groups,[5,6] quaternary ammonium functional groups,[7,8] phthalocyanine–boronic acid functional groups,[9] poly-oxazoline functional groups[10,11]) or by deposition of functional coatings with antibacterial properties (e.g., matrix polymer coatings hosting: quaternary ammonium salts and releasable silver ions,[12] silver ions,[13] copper ions,[14] polycation-bearing catechol,[15] antibacterial peptides;[16,17] or hybrid polymers such as: polydextran aldehyde–polyethyleneimine,[18] polydopamine–silica polymer,[19] chitosan–copper ions,[20] nanoparticles,[12,21] silver binding peptides,[22] peptides,[23] antibiotics,[29] β-carotene/limonene/eugenol,[24] surfactants.[25,48]).

The fabrication of antibacterial coatings is one of the critical strategies for the prevention of bacteria propagation, bacterial biofilm formation, and bacterial infections associated with the attachment of bacteria onto surfaces. Antibacterial coatings have been classified according to the interaction between the antibacterial agent and the bacteria biofilm: (i) antibacterial agent release coatings, and (ii) antibacterial non-release coatings (contact killing coatings, or bacteria repellent coatings).[26]

In the antibacterial agent release approach, the bacteria growth is neutralised or inhibited as a function of the antibacterial leaching agent released over time from the hosting polymer coating. The antibacterial agent can be either bonded electrostatically or covalently. The electrostatically bonded antibacterial agent leaches out reducing their period of antibacterial activity action, while the covalently bonded antibacterial agent displays a prolonged and limited antibacterial activity.[12,27–29] For instance, Druvari et al.[28] prepared an antibacterial copolymer coating to control the release of quaternary ammonium functional groups biocides bonded either covalently or electrostatically and tested against *S. aureus* and *P. aeruginosa*. Yu et al.[30] deposited mineralised collagen loaded with metal-organic frameworks on titanium surfaces to control the release of naringin as an antibacterial agent, to enhance biocompatibility and osseointegration of orthopaedic implants. Montero et al.[31] prepared copper particles embedded in a methyl methacrylate resin for the controlled release of nanoparticles. The antibacterial activity is attributed to the released copper particles which interacted with the bacteria cell walls resulting in the death of the microorganisms such as *S. aureus, E. coli, P. aeruginosa,* and *L. monocytogenes*.

In the antibacterial agent non-release coating approach, there is not a reservoir nor a release of antibacterial agents from the antibacterial coatings. Instead, the antibacterial activity of the antibacterial agent non-release coatings is attributed to: the disruption of the bacterial cell membrane when bacteria interact the antibacterial agent which is covalently bonded to the surface (contact killing surfaces), or the prevention of bacteria adhesion and this bacterial biofilm formation on hydrophobic/hydrophilic surfaces (bacteria repellent surfaces).[1] For Instance, Humblot et al.[32] immobilised antibacterial peptide onto gold surfaces by self-assembled monolayer technique and tested against *E. faecalis,* and *S. aureus*. They found that the immobilised peptide modified and disrupted the bacterial cell wall causing the prevention of the biofilm formation. Mei et al.[33] reported the incorporation of quaternary ammonium groups into acrylic resins for their potential antibacterial contact killing surfaces. Positively charged coatings interact with the anionic lipids from the bacterial cell membranes yielding the bacterial cell membrane disruption. It is likely that the positive charge of the surfactant strongly interacts with the

negatively charged bacterial cell membrane and then disrupts the cell membrane leading to the cell death.[2]

Alternatively to conventional organic antibacterial agents (e.g., antibiotics,[4,30] peptides,[16,23] surfactants[6,8,46]), there have been reported studies about the coordination of antibiotics, and surfactants with metal ions.[34,35] Particularly, the coordination of surfactants with metal ions, to form metal–surfactant complexes, generally enhances the biological and antibacterial activities.[58] Metallosurfactants form micelles, inverse micelles, and vesicles at a critical micelle concentration, like surfactants with enhanced characteristics, due to their complexation with the metal ion.[41,60]

The metallosurfactants are composed of a hydrophobic tail (i.e., the alkyl chain), a polar head group which is bonded to the metal ion through a coordinate bond, where the metal ion acts as a counter ion.[35,45,48] Kabara et al.[36] evaluated the alkyl chain lengths of alkyl amines and they found that the alkyl chain length of C_{11}–C_{13}, were the most effective alkyl chain length against a range of Gram-positive and Gram-negative bacteria. Therefore, the presence of the metal ion in the metallosurfactant and the alkyl chain length enhance the efficiency of the antibacterial activity, and the mode of interaction between the hydrophobic chain tail and the bacterial membrane wall: the long hydrophobic alkyl chain disrupts the bacterial cell through hydrophobic interactions causing bacteria lysis, and the metal ions cause damage to the bacterial cell due to the oxygen reactive species generation.[37,38] Recently, the synthesis of different cationic and non-ionic metallosurfactants coordinated with different transition metal ions (e.g., Cu^{2+},[45,48,49] Cr^{2+},[39,51] Co^{2+},[40,42] Ni^{2+},[41,58] Ag^{1+},[43] Fe^{2+},[46,50] Pd^{2+},[47,57] Mn^{2+},[52,53] Pt^{2+},[54,55]) has been reported for different applications, Table 6.1. For instance, Kumaraguru et al.[39] synthesised double-chain metallosurfactants of chromium complexes with different alkyl amine ligands. They evaluated the antibacterial activity of single- and double-chain metallosurfactants against Gram-positive, and Gram-negative bacteria and found that the double-chain metallosurfactant showed greater antibacterial activity than the single chain metallosurfactant. Dogra et al. fabricated metallosurfactants of cobalt,[40] and nickel[41] complexes. The antibacterial activity by the inhibition zone method of the metallosurfactants in the form of microemulsions was carried out against *S. aureus* and *E. coli*; the

metallosurfactant microemulsion influenced in the bacteria colony forming growth, and confirmed the interaction of the microemulsion components with the bacterial DNA, indicating the mechanism of bacteria death through bacterial DNA damage. Garg et al.[50,51,52] found that the metallosurfactants coordinated with metal ions (e.g., Fe^{2+}, Co^{2+}, Ni^{2+}, Cu^{2+}, Cr^{2+}, Mn^{2+}) enhanced the fluorescence quantum yield of dyes attributed to the metal–surfactant complex. The metallosurfactants showed enhancement of the self-assembled molecular structures to form liposomes (metallosomes), and thus, evaluated the ability of metallosomes as drug carriers to encapsulate dyes. Kaur et al.[43,48] synthesised double-chained metallosurfactants (Ag^{1+}, Co^{2+}, Ni^{2+}, Cu^{2+}) and tested the antibacterial activity against Gram-positive and Gram-negative bacteria. The metallosurfactants inhibited the bacteria growth at a minimum inhibition concentration, and TEM images showed that bacteria cell absorbed the metallosurfactant gradually, which led to bacteria cell perturbation and thus to bacteria death. Additionally, Kaur et al.[57] also reported that the palladium based metallosurfactant displayed similar average zone of inhibition at concentration 100 times lower than the surfactant precursor. These metallosurfactants enhanced the efficiency of the antibacterial activity at even lower inhibition concentration. However, most of these reported metallosurfactants were antibacterial tested in the form of microdilution or microemulsion, and thus limiting the viability of the metallosurfactants to other applications.

To date, no previous works are available for the deposition of metallosurfactant–hosting polymer coatings. Therefore, in this work, we describe an approach to deposit antibacterial plasma polymer coatings hosting bisdodecylamine copper dichloride (CuDDA) as an antibacterial agent[48] and isodecyl acrylate to act as a polymer host matrix using the atomised spray plasma deposition technique, Structure 6.1. The antibacterial activity of the ASPD poly (CuDDA–isodecyl acrylate) coatings was evaluated against *E. coli* and *S. aureus*, and the results showed that the antibacterial activity efficiency was >99.997% upon bacteria contact with the antibacterial coating (film thickness of ~10 µm) for an interacting time of 5 min for *E. coli*, and >99.999% after 10 min of interacting time for both bacteria, respectively.

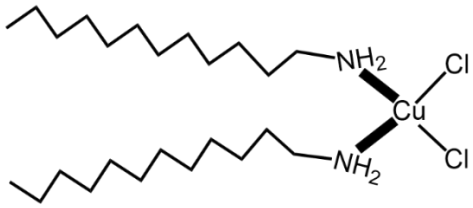

Bisdodecylamine Copper Dichloride

Isodecyl Acrylate

Structure 6.1: Chemical structure of bisdodecylamine copper dichloride metallosurfactant and isodecyl acrylate precursors.

Table 6.1: State of the art of metallosurfactants and applications.

Surfactant / Chelating Ligands	**Metal Ion**	**Antibacterial Activity**	**Applications**	**Ref.**
• Ethylenediamine • Triethylenetetramine • 2,2-bipyridine • 1,10-phenanthroline Axial amine ligands: • Dodecylamine • Cetylamine	• Cr ions	Double-chain metallosurfactants showed excellent antibacterial and antifungal activities against *E. coli, S. aureus, P. vulgaris* and *B. subtilis*	• Antibacterial	39
• Hexadecyltrimethylammonium • Dodecylamine • Hexadecylamine	• Co ions	Excellent antibacterial activity tested by inhibition zone against *S. aureus.*	• Antibacterial	40
• Hexadecyltrimethylammonium • Dodecylamine • Hexadecylamine	• Ni ions	Excellent antibacterial activity tested by inhibition zone against *E. coli.*	• Antibacterial	41
• 2,2'-bipyridine / 1,10-phenanthroline ligands	• Co ions	NA	• Protein transport	42

Surfactant / Chelating Ligands	Metal Ion	Antibacterial Activity	Applications	Ref.
• Cetyltrimethylammonium bromide ligand	• Ag ions	Antibacterial activity against *E. coli* and *S. aureus*. The mechanism is through flagella damage.	• Antimicrobial • Anticancer	43
• Peptide	• Cu ions	Antibacterial activity against *E. coli*, *E. faecalis*, and *S. aureus*.	• Antibacterial • Antifungal	44
• Hexadecyl amine • Dodecyl amine (CuDDA)	• Cu ions	NA	• DNA Interaction	45
• Lauric acid • Palmitic acid • Myristic acid • Steric acid • Morpholine	• Fe ions	The antibacterial activity of cationic surfactants is based on the disruption of the bacterial membrane wall due to the synergetic effect of the hydrophobic interaction and electrostatic absorption. Excellent inhibition zone for *A. nigar, C. albicans, E. coli, B. sutilus*	• Antibacterial activity	46
• Dodecyl amine	• Pd ions	Antibacterial activity against *B. cereus, K. pneumoniae,* and *C. lunata*.	• Catalytic agents • Molecular photo-switches • Antibacterial activity	47
• Dodecyl amine	• Co ions	High antimicrobial activity (inhibition zone) against *B.*	• Protein interaction	48

Surfactant / Chelating Ligands	Metal Ion	Antibacterial Activity	Applications	Ref.
	• Ni ions • Cu ions	*cereus, K. pneumoniae, C. lunata.* The disruption of the bacterial membrane cell can be attributed to the hydrophobic interaction with the metallosurfactant.	• Antimicrobial activity	
• Cationic hexadecyl pyridinium • Bis-hexadecyl pyridinium	• Cu ions	Antimicrobial activity against bacteria (*B. cereus, K. pneumoniae*) and fungus (*C. lunata, H. oryzae, A. fumigates, A. niger, C. herbarum*). Disruption of the bacterial membrane wall through the interaction of the hydrophobic tail. Excellent antibacterial activity tested by inhibition zone.	• Antibacterial activity	49
• Hexadecyl trimethyl ammonium chloride	• Fe ions • Co ions • Ni ions • Cu ions	NA	• Dye-separation process	50
• Hexadecyl trimethyl ammonium	• Cr ions	NA	• Fluorescent label for proteins	51

Surfactant / Chelating Ligands	Metal Ion	Antibacterial Activity	Applications	Ref.
• Cetyltrimethylammonium chloride	• Mn ions	NA	• Gene delivery • Nanoreactors • Drug encapsulation • Controlled release of drugs	52
• Hexadecyltrimethylammonium chloride	• Mn ions	NA	• Photosensitizers	53
• Supramolecular ionic surfactant • *N, N, N*-trimethyl-1-ammonium bromide	• Pt ions	Synergetic effect of hydrophobic and metallic ion interactions. Good inhibition zone for: *P. aeruginosa, E. coli, C. albicans, A. niger*	• Antibacterial • Antifungal • Anticancer	54, 55
• Cetylpyridinium chloride	• Pt ions	Antimicrobial activities against bacteria (*E. coli, P. aeruginosa, S. aureus, B. subtilis*) and fungus (*C. albicans, A. niger*). Results showed high inhibition zone for metalllosurfactants.	• Biological applications	56
• Bis-hexadecyl trimethyl ammonium chloride • Hexadecyl trimethyl	• Pd ions	Results showed high inhibition zone for metalllosurfactants against bacteria (*E. coli* and *S. aureus*) and fungus (*A. niger,*	• Antibacterial • Antimicrobial	57

Surfactant / Chelating Ligands	Metal Ion	Antibacterial Activity	Applications	Ref.
ammonium chloride		*A. fumigatus, C. lunata,* and *H. oryzae*)		
• Dodecyl alcohol • Tetradecyl alcohol • Hexadecyl alcohol • Bromoacetic acid • Diphenyl amine	• Ni ions	Antimicrobial activity against bacteria (*B. pumilus, M. luteus, P. aeruginosa, S. lutea*) yeast (*C. albicans*), and fungi (*P. chrysogenum*). The alkyl chain length affected the antibacterial activity. Therefore, electrostatic interaction and physical disruption due to the hydrophobic interaction may damage the cellular membrane of bacteria	• Biological applications	58
• Dodecyl salicylaldimine	• Co ions	Antibacterial activity against bacteria (*S. aureus, B. cereus, M. luteus, E. coli, K. pneumoniae, P. aeruginosa*) and fungi (*A. niger, penicillium*).	• Antibacterial • Antifungal	59
• Bis-hexadecyl pyridium chloride	• Fe ions • Co ions • Ni ions	Antibacterial activity against *B. cereus, B. polymyxa, K. pneumoniae*, and *P. aeruginosa*.	• Antibacterial	60

6.2 Results and Discussion

6.2.1 Atomised Spray Plasma Deposition

Isodecyl acrylate (+99.9% Sigma-Aldrich Ltd.) and bisdodecylamine copper dichloride (CuDDa) (provided by Dr. Gurpreet Kaur, and Dr. Preeti Garg from the Department of Chemistry, Centre of Advanced Studies in Chemistry, Panjab University, India, who synthesised the metallosurfactant precursors. Dr. Preeti Garg additionally worked on antibacterial tests)[45,48] were used for the fabrication of 2% w/v ASPD (CuDDA–isodecyl acrylate) coatings using the atomised spray plasma deposition, a single-step and substrate-independent method for functional polymer coating deposition. Ambient temperature deposition was carried out using a 50 W continuous wave plasma in conjunction with the atomisation of the liquid–slurry solution into the reaction chamber employing an optimised flow rate of $11 \pm 1 \times 10^{-4}$ mL s^{-1} and plasma post-treatment.

The metallosurfactant, bisdodecylamine–copper dichloride, acted as an antibacterial agent that, upon their incorporation into the plasma polymer coating, displayed high antibacterial activity efficiency. The CuDDA–isodecyl acrylate suspension was introduced in the form of droplets into the electrical discharges where the reactive plasma species activated the carbon–carbon double bond of the acrylate group in the plasma phase followed the free radical polymerisation leading to the deposition of the plasma polymer coating and this polymeric matrix hosted the metallosurfactants through electrostatic interactions.

6.2.2 X-ray Photoelectron Spectroscopy

The ASPD poly (isodecyl acrylate) layer was analysed by XPS, and it just detected carbon and oxygen corresponding to the elemental composition of the precursor monomer, Figure 6.1 and Table 6.2. In contrast, with the incorporation of the metallosurfactant, bisdodecylamine copper dichloride (CuDDA), to yield the 2% w/v ASPD (CuDDA–isodecyl acrylate) layers,

additional XPS elemental signals were detected (0.2–5 nm XPS sampling depth[61]) such as nitrogen, chloride, and copper corresponding to the elemental composition of the metallosurfactant. Additionally, a small amount of palladium contaminant was detected which may have been incorporated during the preparation of metallosurfactants using different metallic ions (others metal ions used for the preparation of metallosurfactants, not included in this work: Pd^{2+}, and Fe^{2+}), Figure 6.1.

The C(1s) XPS spectra of the ASPD poly (isodecyl acrylate) coatings were fitted to three Gaussian Mg $K\alpha_{1,2}$ components in conjunction with their corresponding Mg $K\alpha_3$, and Mg $K\alpha_4$ satellite peaks shifted towards lower binding energies by ~8.4 and ~10.2 eV respectively, Figure 6.2. The C(1s) Mg $K\alpha_{1,2}$ components being: hydrocarbon carbon $\underline{C}_xH_y$ at 285.0 eV, alkoxy $\underline{C}$–O, at 286.7 eV, and ester O–$\underline{C}$=O, at 289.0 eV showed good retention of the functional groups which agrees with the composition of the precursor monomer. On the other hand, upon the incorporation of the metallosurfactant, the alkoxy, $\underline{C}$–O, group decreased slightly; an additional peak at 282.1 eV corresponding to a metal carbide was detected which may be due to the decomposition of the metallosurfactant; then the metal ion (copper or palladium) covalently bonded to carbon during the atomised spray plasma deposition process.[62,63]

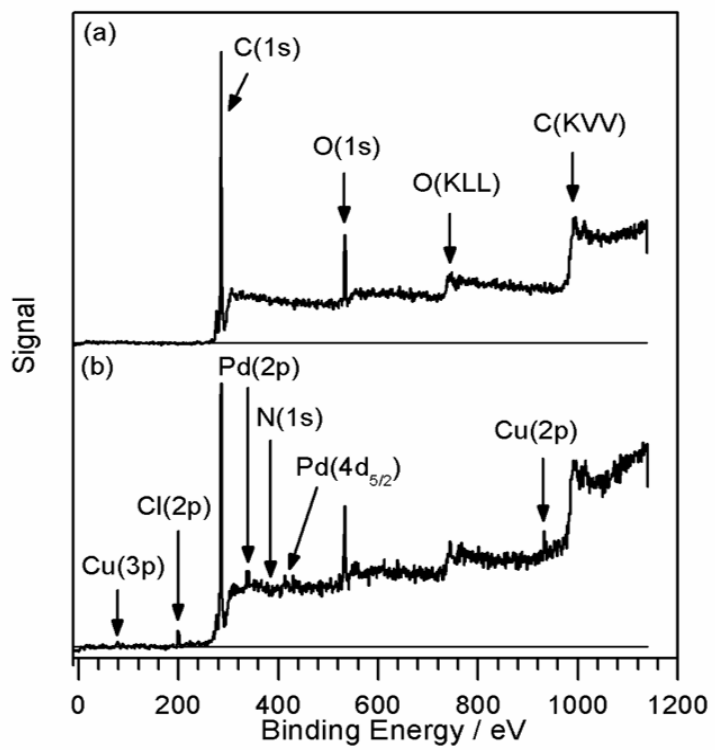

Figure 6.1: Wide scan spectra of: (a) ASPD poly (isodecyl acrylate) coating, and (b) 2% w/v ASPD (CuDDA–isodecyl acrylate) coating.

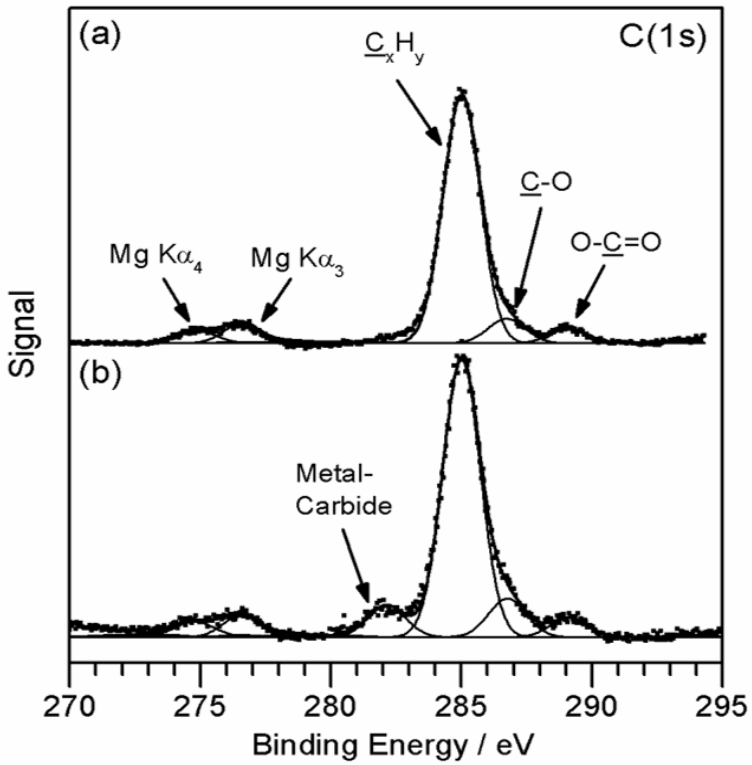

Figure 6.2: C(1s) XPS spectra of: (a) ASPD poly (isodecyl acrylate) coatings, and (b) 2% w/v ASPD (CuDDA–isodecyl acrylate) coating.

Table 6.2: XPS elemental composition for precursors (theoretical) and the corresponding ASPD polymer coating.

System / Plasma Post-treatment Time	Atomic Composition / %					C:O Ratio	C(1s) Component / %			O(1s) Component / %	
	C	O	N	(Cu + Pd)	Cl		$\underline{C}_xH_y$	$\underline{C}$–O	O–$\underline{C}$=O	C=$\underline{O}$	C–$\underline{O}$
Theoretical isodecyl acrylate	86.7	13.3	NA	NA	NA	6.5	84.6	7.7	7.7	50	50
Theoretical CuDDA	82.8	NA	6.9	3.4	6.9	NA	NA	NA	NA	NA	NA
ASPD poly (isodecyl acrylate) layer, 1 min	88.9 ± 1.3	11.1 ± 1.3	NA	NA	NA	8.1 ± 1.0	86.3 ± 0.9	8.5 ± 0.6	5.2 ± 0.4	50.3 ± 4.3	49.7 ± 4.3
ASPD poly (CuDDA-isodecyl acrylate) layer, 1 min	82.1	9.1	3.3	1.5	3.9	9.0	82.7	11.6	5.7	51.3	48.7

6.2.3 Infrared Spectroscopy

The infrared spectroscopy of the ASPD poly (isodecyl acrylate) coated polypropylene cloth showed the disappearance of the vinyl functional group of the acrylate which suggest that conventional radical polymerisation occurred through the vinyl group during the atomisation of isodecyl acrylate within the plasma, Figure 6.3. The infrared spectrum of the ASPD poly (isodecyl acrylate) coated polypropylene cloth indicates the functional groups´ retention associated with the isodecyl acrylate precursor with the following characteristic infrared bands: alkyl chains (2957–2830 cm^{-1}); carbonyl ester, C=O (1731 cm^{-1}); and the $–CH_2–$ stretching (1459 cm^{-1}) and $–C(CH_3)$ symmetric bending (1382 cm^{-1}) corresponding to the polypropylene cloth substrate.

On the other hand, there is no visible change in the functional groups or fingerprint of the spectrum related to the absorption bands of the metallosurfactant in the 2% w/v ASPD (CuDDA–isodecyl acrylate) coating, although incorporation of the metallosurfactant into the plasma polymer coating was confirmed by the XPS results. The absence of any characteristic infrared band from the metallosurfactant may be due to the small concentration of the bisdodecylamine copper dichloride metallosurfactant, and that the infrared analysis is not a sensitive surface analysis (depth penetration of 0.5–6 µm in ATR[64]).

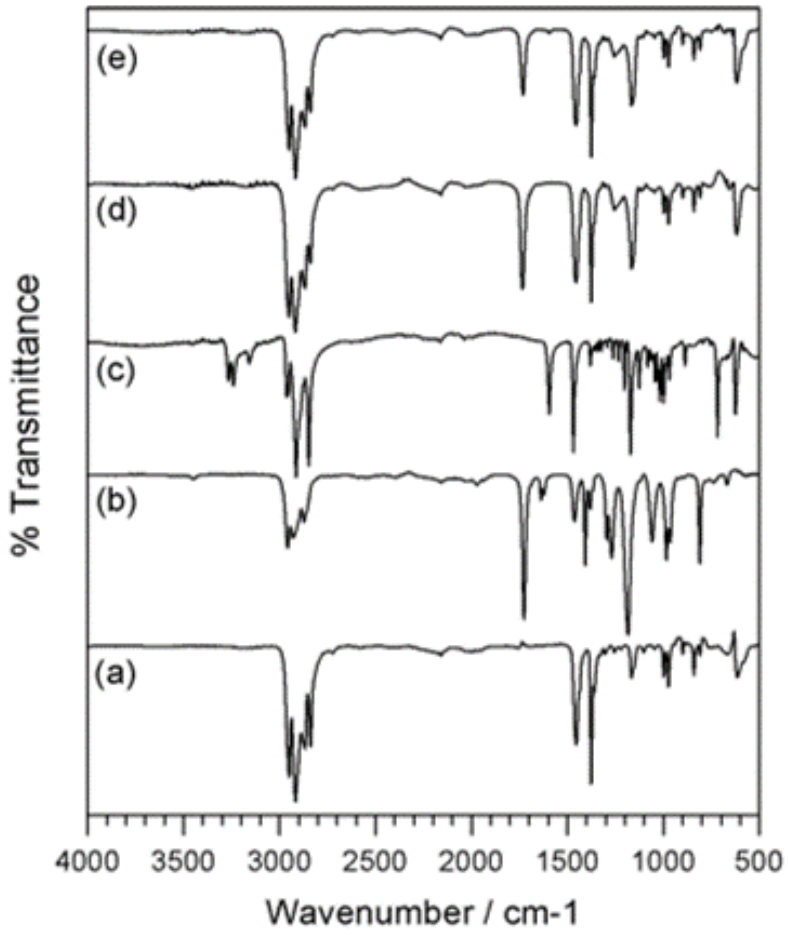

Figure 6.3: Infrared spectra of: (a) polypropylene cloth; (b) isodecyl acrylate precursor; (c) bisdodecylamine copper dichloride (CuDDA); (d) ASPD poly (isodecyl acrylate) coating; (e) 2% w/v ASPD (CuDDA–isodecyl acrylate) coating. Plasma polymer coatings were deposited on polypropylene cloth.

Table 6.3: Infrared assignments for precursors and the corresponding ASPD polymer coatings.[65,66]

Assignment	Absorption Frequency / cm^{-1}				
	Substrate	Precursors		ASPD Coatings	
	Polypropylene Cloth	Isodecyl Acrylate	CuDDA	ASPD poly (isodecyl acrylate)	2% w/v ASPD poly (CuDDA–isodecyl acrylate)
$R–NH_2$ symmetric stretching	-	-	3240	-	-
CH_3 antisymmetric stretching	2953	2960	2960	2953	2953
CH_2 antisymmetric stretching	2917	2924	2914	2921	2917
CH_3 antisymmetric stretching	2867	2870	2848	2864	2867
CH_2 symmetric stretching	2831	2860–2830	2860–2830	2838	2838
C=O stretching	-	1727	-	1731	1731
C=C stretching	-	1632	-	-	-
$R–NH_2$ bending	-	-	1595	-	1595
$–CH_2–$ stretching	1459	1463	1463	1456	1456
$=CH_2$ bending	-	1402	-	-	-
$–CH(CH_3)$ symmetric bending	1382	1377	1380	1377	1377
C–O stretching	-	1260, 1181	-	1260, 1181	1260, 1181
C–N stretching	-	-	1174	-	-

Assignment	Absorption Frequency / cm^{-1}				
	Substrate	Precursors		ASPD Coatings	
	Polypropylene Cloth	Isodecyl Acrylate	CuDDA	ASPD poly (isodecyl acrylate)	2% w/v ASPD poly (CuDDA–isodecyl acrylate)
$–CH(CH_3)_2$ stretching	1175–1140 1060–1040	1175–1140	1175–1140	1175–1140	1175–1140
$=CH_2$ bending	-	983	-	983	983

6.2.4 Scanning Electron Spectroscopy

Surface topography of the polypropylene cloth with different ASPD plasma polymer coatings was analysed by SEM, Figure 6.4. The cloth threads of the untreated PP cloth exhibited clean and smooth surfaces. Similarly, the ASPD poly (isodecyl acrylate) coated PP cloth showed a smooth and uniform coating over the thread surface. On the contrary, in the 2% w/v ASPD (CuDDA–isodecyl acrylate) coated PP cloth showed the randomly dispersed particles encapsulated by the plasma polymer which is attributed to the incorporation of the metallosurfactant and it is even observed deeper into the PP cloth substrate. This may suggest that due to the hydrophobic nature of the isodecyl acrylate precursor monomer and the hydrophobic interactions between the hydrophobic parts of both precursors, the metallosurfactant formed reverse vesicles prior to the ASPD as observed in the aggregation of metallosurfactants in non-polar solvents,[52] and remained trapped within the ASPD poly (isodecyl acrylate) coating acting as a host matrix containing the inverse vesicles.

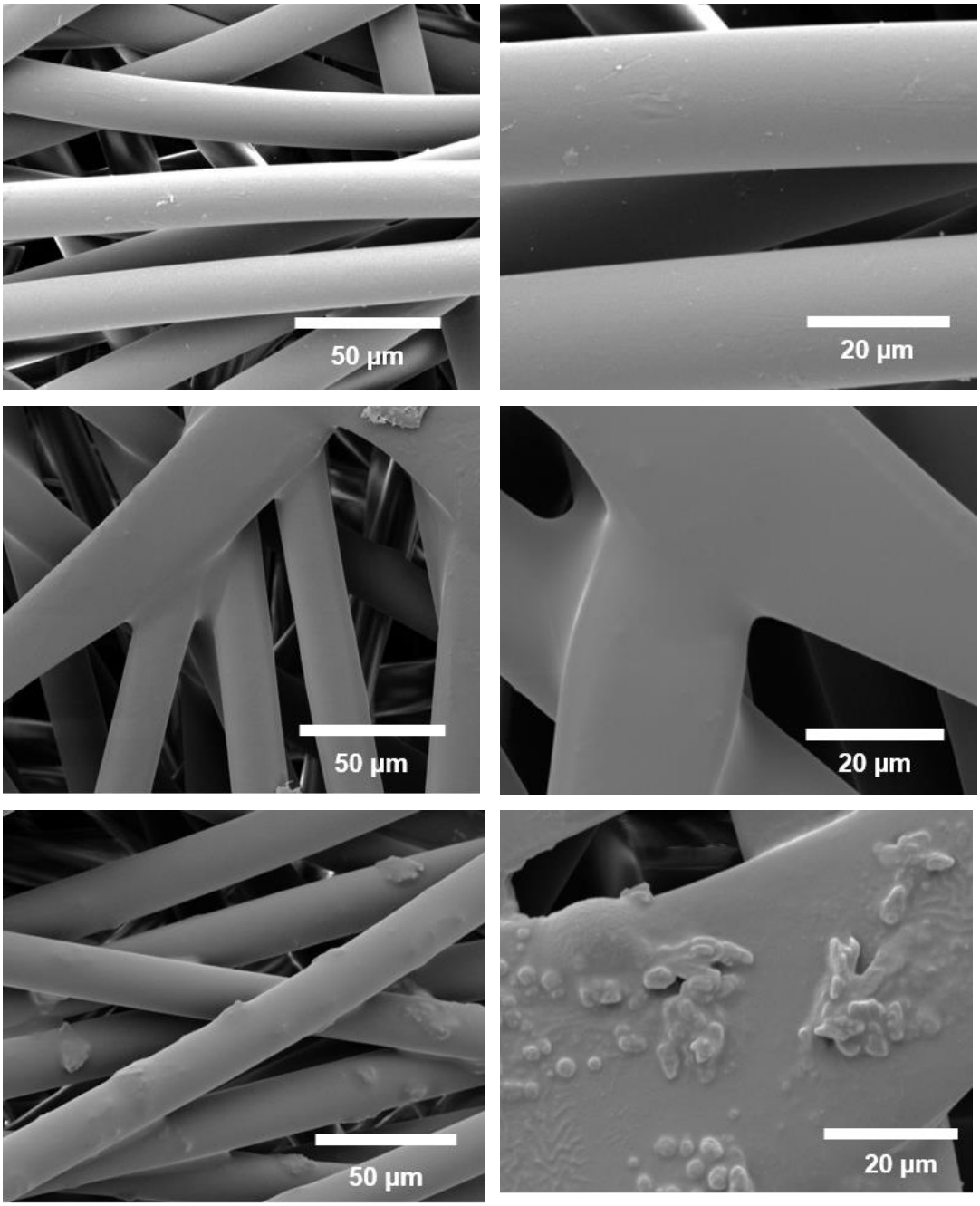

Figure 6.4: SEM images of polypropylene cloth coated with: (top row) untreated; (middle row) ASPD poly (isodecyl acrylate) coating; and (bottom row) 2% w/v ASPD (CuDDA–isodecyl acrylate) coating.

6.2.5 Deposition Rate

The ASPD poly (isodecyl acrylate) coating was carried out at an optimum flow rate of 11 ± 1 x 10^{-4} mL s^{-1} resulting in an optimum deposition rate of 1.0 ± 0.3 µm min^{-1} and film thickness of 8.4 ± 2.9 µm. The incorporation of the metallosurfactant led to an increase of the deposition rate and film thickness of the 2% w/v ASPD (CuDDA–isodecyl acrylate) layer by ~50% and ~18% respectively, Table 6.4.

Table 6.4: Characteristics of the optimum 2% w/v ASPD (CuDDA–isodecyl acrylate) coatings.

Coating	**Deposition Rate / µm min^{-1}**	**Film Thickness / µm**	**Water Contact Angle / °**
Untreated polypropylene cloth	**-**	**-**	**94°**
ASPD poly (isodecyl acrylate) coating	1.0 ± 0.3	8.4 ± 2.9	98 ± 4
2% w/v ASPD (CuDDA–isodecyl acrylate) coating	1.5 ± 0.8	9.9 ± 4.7	105 ± 4

6.2.6 Static Contact Angle

ASPD poly (isodecyl acrylate) layers showed a hydrophobic behaviour measured by the water contact angle technique. Similarly, the 2% w/v ASPD (CuDDA–isodecyl acrylate) layers displayed a slight rise in the hydrophobicity, Table 6.4.

6.2.7 Antibacterial Activity Test

Antibacterial activity test was performed against Gram-negative *E. coli* wild-type (CGSC 7636; rrnB3 ΔbcZ4787 hsdR514 Δ(araBAD)567 Δ(rhaBAD)568 rph-1) and Gram-positive *S. aureus* (FDA209P, an MSSA strain; ATCC 6538P) bacteria species at an interacting time of 16 h for different samples, Figure 6.5. Both control samples, untreated polypropylene cloth and ASPD poly (isodecyl acrylate) coated cloth, displayed no antibacterial activity against both bacteria species. The incorporation of 1% w/v of metallosurfactant, i.e. 1% w/v ASPD (CuDDA–isodecyl acrylate) coated cloth, displayed a bacterial log reduction of ~1 against *E. coli*. In contrast, the optimum 2% w/v ASPD (CuDDA–isodecyl acrylate) coated cloth showed higher antibacterial activity (log reduction > 9) against both *E. coli* and *S. aureus* displaying 100% elimination of bacteria, Figure 6.5.

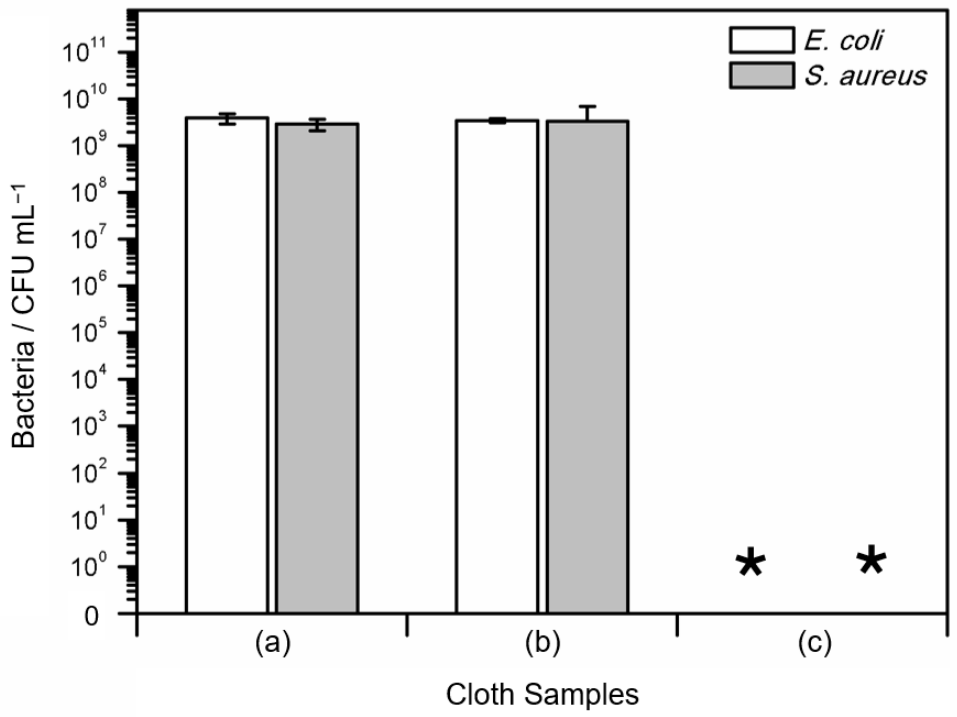

Figure 6.5: Antibacterial activity against *E. coli* and *S. aureus* at an interacting time of 16 h for: (a) untreated polypropylene cloth; (b) ASPD poly (isodecyl acrylate) coated polypropylene cloth; and (c) optimum 2% w/v ASPD (CuDDA–isodecyl acrylate) coated polypropylene cloth. ✶ indicates no bacterial growth on the sample surface.

The antibacterial activity performance of the optimum 2% w/v ASPD (CuDDA–isodecyl acrylate) coated cloth was analysed as a function of the interacting time when tested against *E. coli* and *S. aureus*, Figure 6.6. The antibacterial activity of the 2% w/v ASPD (CuDDA–isodecyl acrylate) coated cloth against *E. coli* was observed after 5 min displaying a log reduction of ~4.5 (bacterial reduction of 99.997%), and higher than 99.999% of bacterial reduction after 10 min of interacting time for both bacteria species, *E. coli* (log reduction = 4.9), and *S. aureus* (log reduction = 8.0)—a coating is considered antibacterial if the log reduction is higher than 3.[67] These results indicate higher antibacterial efficiency of the optimum 2% w/v ASPD (CuDDA–isodecyl acrylate) coated cloth towards *E. coli*, probably due to its cell wall susceptibility to physical damage in the presence of the metallosurfactant due to the thin peptidoglycan layer and the focused attack of copper ions to the periplasmic space, and hydrophobic interaction between the hydrophobic part of the metallosurfactant and the hydrophobic character of the cell membrane.[2,41,45]

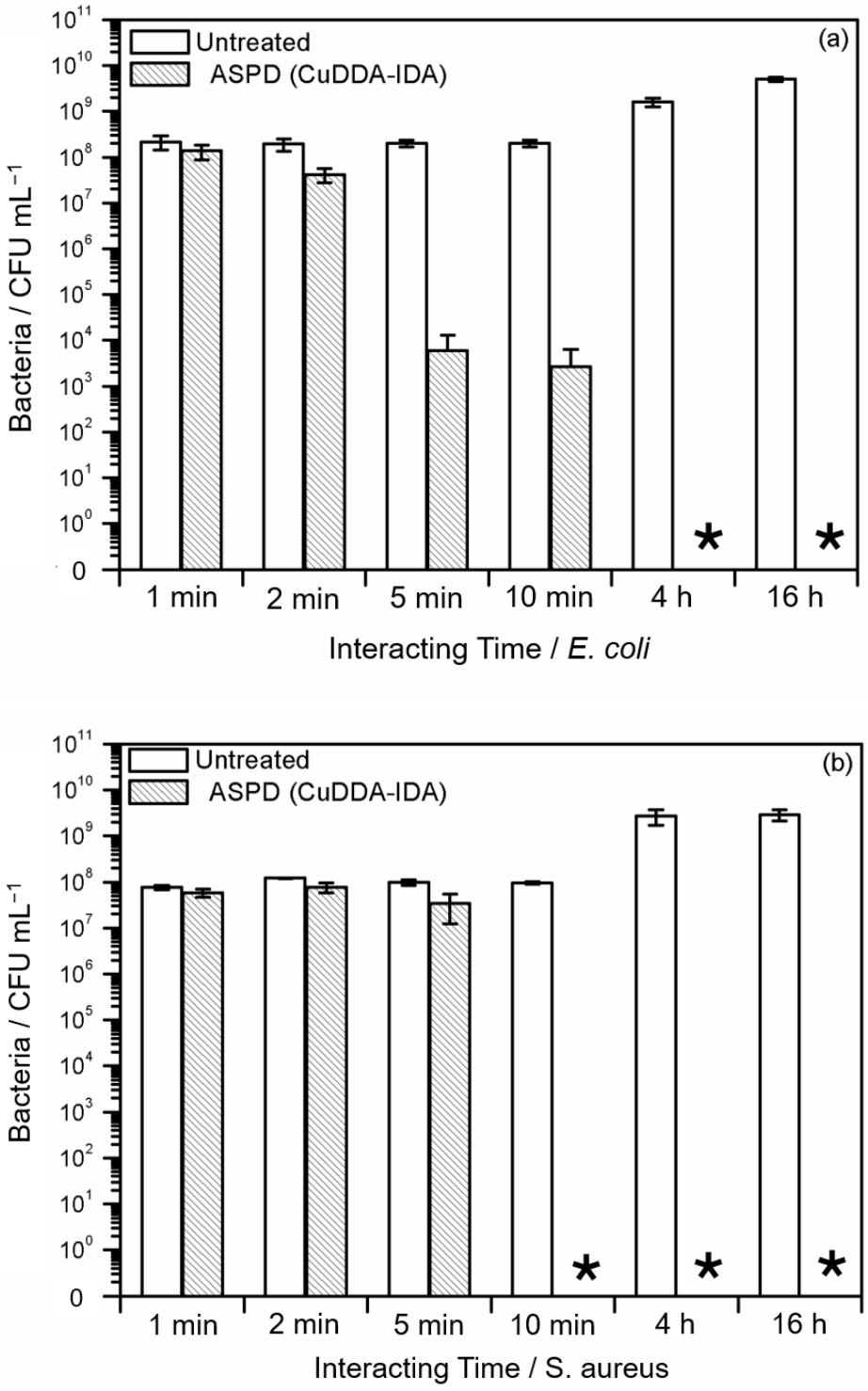

Figure 6.6: Antibacterial activity of the optimum 2% w/v ASPD (CuDDA–isodecyl acrylate) coated cloth against (a) *E. coli* and (b) *S. aureus* as a function of the interacting time. * indicates no bacterial growth on the sample surface.

The antibacterial performance of the optimum 2% w/v ASPD (CuDDA–isodecyl acrylate) coated cloth against *E. coli* and *S. aureus* was evaluated as a function of the recycling cycles, Figure 6.7. The antibacterial activity against *E. coli* of the optimum 2% w/v ASPD (CuDDA–isodecyl acrylate) coated cloth was higher than 99.991% up to the 3rd recycling cycle, and sharply decreased for the 4th recycling cycle displaying a bacteriostatic reduction of ~42%. This indicates the rapid depletion and leaching of the metallosurfactant from the optimum 2% w/v ASPD (CuDDA–isodecyl acrylate) coated cloth. On the other hand, the antibacterial performance of the optimum 2% w/v ASPD (CuDDA–isodecyl acrylate) coated cloth against *S. aureus* showed a bacteriostatic reduction remaining over ~95% up to the 4th recycling cycle.

For the recycling process, the 2% w/v ASPD (CuDDA–isodecyl acrylate) coated cloth samples were taken from the x10^{-1} bacterial solution and rinsed with Milli-Q® water for 1 min and dried for the next recycling cycle. The decrease of the antibacterial activity efficiency after consecutive recycling cycles, may be attributed to the depletion and leaching of the metallosurfactant incorporated within the hydrophobic plasma–polymer matrix host when the liquid bacterial solution interacts with the 2% w/v ASPD (CuDDA–isodecyl acrylate) coated cloth. Additionally, the rapid leaching of the metallosurfactant may suggest that the metallosurfactant contained within the 2% w/v ASPD (CuDDA–isodecyl acrylate) coated cloth is incorporated through hydrophobic, and electrostatic interactions within the hydrophobic alkyl chain of both the metallosurfactant and ASPD poly (isodecyl acrylate) coating.

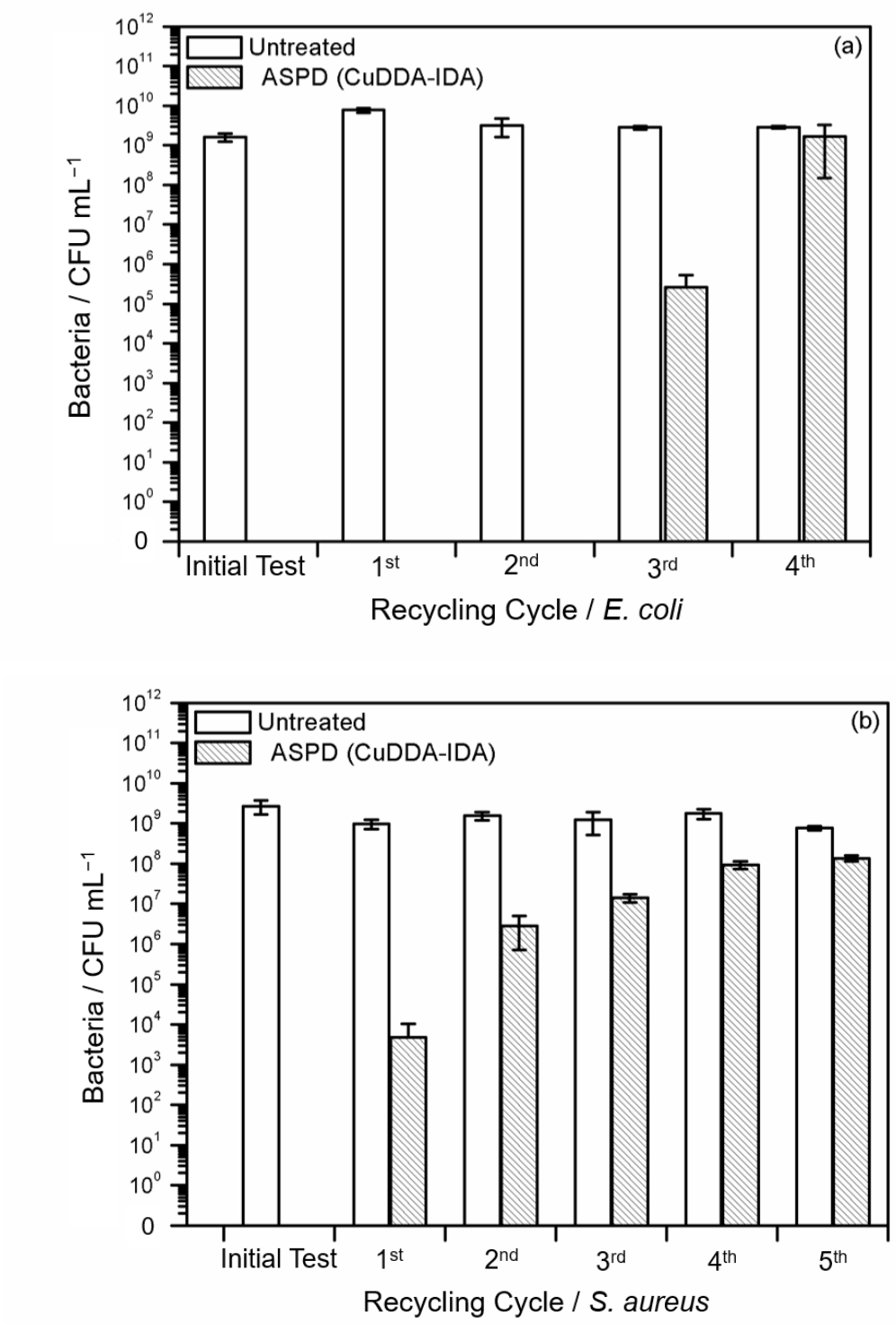

Figure 6.7: Antibacterial performance at different recycling cycle steps against (a) *E. coli* and (b) *S. aureus* at interacting time of 4 h for the optimum 2% w/v ASPD (CuDDA–isodecyl acrylate) coated cloth, compared to untreated controls.

Overall, due to the antibacterial agent release characteristics of the 2% w/v ASPD (CuDDA–isodecyl acrylate) coatings, it is suggested that the

released metallosurfactants interact with bacteria in the testing bacterial aqueous solution, and thus, causing bacterial cell wall disruption and bacterial cell death. It has been reported that metallosurfactants in microemulsion are absorbed by the bacteria cells causing membrane disruption, DNA damage, and bacteria cell lysis as a synergetic effect of metal–surfactant complex enhancing the cell damage, and thus, the antibacterial activity efficiency.[40,43] Furthermore, copper ions generate reactive oxygen species which damage the outer membrane, periplasm, cytoplasm, and DNA, and inhibit essential enzymes in the periplasm through the absorption of the metallosurfactants causing membrane disruption and bacteria cell death.[2,40,68] However, *E. coli* bacteria are reported to be more susceptible to membrane disruption because copper ions interact mostly with the periplasmic space found only in Gram-negative bacteria causing oxidative stress, faster membrane disruption and bacteria death,[69,70,71] which is in accordance with the faster bacteria-reduction response for *E. coli* in this work, Figure 6.6. On the other hand, considering that the hydrophobic alkyl chain length has a notable effect in the antibacterial activity of alkyl amines,[36] and the cell membrane is composed of lipids and proteins, which make the cell membrane to have hydrophobic behaviour.[2] The hydrophobic alkyl chain may interact with the bacterial cell membrane through hydrophobic interactions, causing mechanical disruption, additional bacterial cell membrane damage, and faster bacteria death.[36] Therefore, The experimental results showed that the optimum 2% ASPD poly (CuDDA–isodecyl acrylate) coated cloth displayed excellent antibacterial activity efficiency (>99.999%) after 10 min of interacting time between the bacteria and the antibacterial plasma polymer coating surface with a film thickness of ~10 µm.

6.3 Conclusions

Atomised spray plasma deposition technique was used to fabricate antibacterial polymer coatings using a double-alkyl chain copper metallosurfactant as an antibacterial agent, resulting in the optimum 2% w/v ASPD poly (CuDDA–isodecyl acrylate) coatings. The optimum 2% w/v ASPD

poly (CuDDA–isodecyl acrylate) coatings displayed excellent antibacterial activity against both Gram-negative and Gram-positive bacteria at 10 min of interacting time.

The incorporation of the double-alkyl-chained copper metallosurfactant was confirmed with the XPS, and infrared analyses. After ASPD treatment, the morphology of the substrate surface did not change significantly, although random trapped metallomicelles were found within the plasma polymer coating as observed in SEM images. The hydrophobic behaviour of the optimum 2% w/v ASPD poly (CuDDA–isodecyl acrylate) coatings did not represent any disadvantage for the antibacterial activity since the results indicated that the plasma polymer coatings were effective against both Gram-positive and Gram-negative bacteria—commonly, hydrophobic coatings repel the bacteria from the surface rather than acting as a contact killing surface. However, due to the composition and structure of the cell membrane, *E. coli* bacteria were more susceptible to cell membrane disruption than *S. aureus*.

6.4 References

(1) Riool, M.; Breji, A.; Drijfhout, J. W.; Nibbering, P. H.; Zaat, S. Antimicrobial Peptides in Biomedical Device manufacturing. Frontier Chem. 2017, 5, 00063.

(2) Tortora, G. J.; Funke, B. R.; Case, C. L. *Microbiology An Introduction*; Pearson Education Inc.: United States of America, 2016; pp 150–172.

(3) Ghilini, F.; Rodriguez-Gonzalez, M. C.; Schilardi, P. L. Highly Stabilized Nanoparticles on Poly- L- Lysine-Coated Oxidized Metals: A Versatile Platform with Enhanced Antimicrobial Activity. *ACS Appl. Mater. Interface* **2018**, *10*, 23657–23666.

(4) Pissinis, D. E.; Benitez, G. A.; Schilardi, P. L. Two.Step Biocompatible Surface Functionalization for Two-Pathway Antimicrobial Action Against Gram-Positive Bacteria. *Colloid. Surf.* **2018**, *164*, 262–271.

(5) Subik, J.; Takacsova, G.; Psenak, M.; Devinsky, F. Antimicrobial Activity of Amine Oxides: Mode if Action and Structure-Activity Correlation. *Antimicrob. Agent Ch.* **1977**, *12*, 139–146.

(6) Endo, Y.; Tani, T.; Kodama, M. Antimicrobial Activity of Tertiary Amine Covalently Bonded to a Polystyrene Fiber. *Appl. Environ. Microb.* **1987**, *53*, 2050–2055.

(7) Wang, B.; Xu, Q.; Ye, Z.; Liu, H.; Lin, Q.; Nan, K.; Li, Y.; Wang, Y.; Qi, L.; Chen, H. Copolymer Brushes with Temperature-Triggered, Reversibly Switchable Bactericidal and Antifouling Properties for Biomaterial Surfaces. *ACS Appl. Mater. Interfaces* **2016**, *8*, 27207–27217.

(8) Ortega, P.; Copa-Patiño, J. L.; Muñoz-Fernandez, M. A.; Soliveri, J.; Gomez, R.; de la Mata, F. J. Amine and Ammonium Functionalization of Chloromethylsilane-ended Dendrimers. Antimicrobial Activity Studies. *Org. Biomol. Chem.* **2008**, *6*, 3264–3269.

(9) Galstyan, A.; Schiller, R.; Dobrindt, U. Boronic Acid-Functionalized Photosensitizers: A Straightforward Strategy to Target the Sweet Site of Bacteria and Implement Active Agents in Polymer Coating. *Angew. Chem. Int. Ed.* **2017**, *56*, 10362–10366.

(10) Charnley, M.; Textor, M.; Acikgoz, C. Designed Polymer Structures with Antifouling-Antimicrobial Properties. *React. Funct. Polym.* **2011**, *71*, 329–334.

(11) Fik, C. P.; Krumm, C.; Muenning, C.; Baur, T. I.; Salz, U.; Bock, T. Impact of Functional Satellite Groups on the Antimicrobial Activity and Hemocompatibility of Telechelic Poly(2-methyloxazoline)s. *Biomacromol.* **2011**, *13*, 165–172.

(12) Li, Z.; Lee, D.; Sheng, X.; Cohen, R. E.; Rubner, M. F. Two-Level Antibacterial Coating with Both Release-Killing and Contact-Killing Capabilities. *Langmuir* **2006**, *22*, 9820–9823.

(13) Marini, M.; Niederhausern, S. Iseppi, R.; Bondi, M.; Sabia, C.; Toselli, M.; Pilati, F. Antibacterial Activity of Plastics Coated with Silver-Doped Organic–Inorganic Hybrid Prepared by Sol–Gel Processes. *Biomacromol.* **2007**, *8*, 1246–1254.

(14) Sun, C.; Li, Y.; Li, Z.; Su, Q.; Wang, Y.; Liu, X. Durable and Washable Antibacterial Copper Nanoparticles Bridged by Surface Grafting Polymer Brushes on Cotton and Polymeric Materials. *Hindawi J. Nanomater.* **2018,** 6546193.

(15) Faure, E.; Falentin-Daudre, C.; Lanero, T.; Vreuls, C.; Zocchi, G.; de Weerdt, C.; Jerome, C.; Duwez, A.-S.; Detrembleur, C. Functional Nanogels as Platforms for Imparting Antibacterial, Antibiofilm, and Antiadhesion Activities to Stainless Steel. *Adv. Funct. Mater.* **2012**, *22*, 5271–5282.

(16) Albada, B.; Metzler-Nolte, N. Highly Potent Antibacterial Organometallic Peptide Conjugates. *ACC. Chem. Res.* **2017**, *50*, 2510–2518.

(17) Kandiyote, N. S.; Avisdris, T.; Arnush, C. J.; Kasher, R. Grafted Polymer Coatings Enhance Fouling Inhibition by an Antimicrobial Peptide on Reverse Osmosis Membranes. *Langmuir* **2019**, *35*, 1935–1943.

(18) Meng, Q. Li, Y.; Shen, C. Antibacterial Coatings of Biomedical Surfaces by Polydextran Aldehyde/Polyethylenimine Nanofibers. *ACS Appl. Bio Mater.* **2019**, *2*, 562–569.

(19) Fu, Y.; Cai, M.; Zhang, E.; Cao, S.; Ji, P. A Novel Polymer Network for Efficient Anticorrosive and Antibacterial Coatings. *Ind. Eng. Chem. Res.* **2016**, *55*, 4482–4489.

(20) Mitra, D.; Li, M.; Kang, E.-T.; Neoh, K. Transparent Copper-Loaded Chitosan/Silica Antibacterial Coatings with Long-Term Efficacy. *ACS Appl. Mater. Interfaces* **2017**, *9*, 29515–29525.

(21) Chen, J.; Li, S.; Luo, J.; Wang, R.; Ding, W. Enhancement of the Antibacterial Activity of Silver Nanoparticles Against Phytopathogenic Bacterium *Ralstonia solanacearum* by Stabilization. *J Nanomater.* **2016**, *7135852*, 15.

(22) Jo, Y. K.; Seo, J. H.; Choi, B. H.; Kim, B. J.; Shin, H. H.; Hwang, B. H.; Cha, H. J. Surface-Independent Antibacterial Coating using Silver Nanoparticle-Generating Engineered Mussel Glue. *ACS Appl. Mater. Interfaces* **2014**, *6*, 20242–20253.

(23) Majhi, S.; Arora, A.; Mishra, A. Surface Immobilization of a Short Antimicrobial Peptide (AMP) as an Antibacterial Coating. *Materialia* **2019**, *6*, 100350.

(24) Breloy, L.; Quarabi, C. A.; Brosseau, A.; Dubot, P.; Brezova, V.; Andaloussi, S.; Malval, J. Versace, D. β-Carotene/Limonene Derivatives/Eugenol: Green Synthesis of Antibacterial Coatings under Visible-Light Exposure. *ACS Sustainable Chem. Eng.* **2019**, *7*, 19591–19604.

(25) Czuba, U.; Quintana, R.; Lassaux, P.; Bombera, R.; Geccome, G.; Bañuls-Ciscar, J.; Moreno-Couranjou, M.; Detrembleur, C.; Choquet, P. Anti-Biofouling Activity of Ranaspumin-2 Bio-Surfactant on Catechol-Functional PMMA Thin Layers Prepared by Atmospheric Plasma Deposition. *Colloid Surf. B.* **2019**, *178*, 120–128.

(26) Cloutier, M.; Mantovani, D.; Rosei, F. Antibacterial Coatings: Challenges, Perspectives, and Opportunities. *Trend Biotechnol.* **2015**, *33*, 637–652.

(27) Kougia, E.; Tselepi, M.; Vasilopoulos, G.; Lainioti, G.; Koromilas, N. D.; Druvari, D.; Bokias, G.; Vantarakis, A.; Kallitis, J. K. Evaluation of Antimicrobial Efficiency of New Polymers Comprised by Covalently Attached and/ or Electrostatically Bound Bacteriostatic Species, Based on Quaternary Ammonium Compounds. *Molecule* **2015**, *20*, 21313–21327.

(28) Druvari, D.; Koromilas, N. K.; Lainioti, G.; Bokias, G.; Vasilopoulos, G.; Vantarakis, A.; Baras, I.; Dourala, N.; Kallitsis, J. Polymeric Quaternary Ammonium-Containing Coatings with Potential Dual Contact-Based and Release-Based Antimicrobial Activity. *ACS Appl. Mater. Interfaces* **2016**, *8*, 35593–35605.

(29) Wang, B.; Liu, H.; Wang, Z.; Shi, S.; Nan, K.; Xu, Q.; Ye, Z.; Chen, H. A Self-Defensive Antibacterial Coating Acting Through the Bacteria-Triggered Release of a Hydrophobic Antibiotic from a Layer-by-Layer Films. *J. Mater. Chem. B* **2017**, *5*, 1498.

(30) Yu, M.; You, D.; Zhuang, J.; Lin, S.; Dong, L.; Weng, S.; Zhang, B.; Cheng, K.; Weng, W.; Wang, H. Controlled Release of Naringin in Metal-Organic Framework-Loaded Mineralized Collagen Coating to Simultaneously Enhance Osseointegration and Antibacterial Activity. *ACS Appl. Mater. Interfaces* **2017**, *9*, 19698–19705.

(31) Montero, D. A.; Arellano, C.; Pardo, M.; Vera, R.; Galvez, R.; Cifuentes, M.; Berasain, M. A.; Gomez, M.; Ramirez, C.; Vidal, R. Antimicrobial Properties of a Novel Copper-Based Composite Coating with Potential for Use in Healthcare Facilities. *Antimicrob. Resist. In.* **2019**, *8*, 1–10.

(32) Humblot, V.; Yala, J.-F.; Thebault, P.; Boukerma, K.; Hequet, A.; Berjeaud, J.-M. Pradier, C.-M. The Antibacterial Activity of Magainin I Immobilized onto Mixed Thiols Self-Assembled Monolayers. *Biomaterials* **2009***, 30*, 3503–3512.

(33) Mei, L.; Ren, Y.; Loontjens, T. J. A.; va der Mei, H. C.; Busscher, H. J. Contact-Killing of Adhering Streptococci by a Quaternary Ammonium Compound Incorporated in an Acrylic Resin. *Int. J. Artif. Organs* **2012**, *35*, 854–863.

(34) Al-Khodir, F. A. I.; Refat, M. S. Synthesis, Spectroscopic, Thermal Analyses, and Anti-Cancer Studies of Metalloantibiotic Complexes of Ca(II), Zn(II), Pt(II), Pd(II), and Au(III) with Albendazole Drug. *Russian J. Gral. Chem.* **2015**, *85*, 1734–1744.

(35) Fallis, I. A.; Griffiths, P. C.; Griffiths, P. M.; Hibbs, D. E.; Hursthouse, M. B.; Winnington, A. L. Solid State and Solution Behavior of Novel Transition Metal Containing. *Chem. Commun.* **1998**, *10*, 65–66.

(36) Kabara, J. J.; Conley, A. J.; Truant, J. P. Relationship of Chemical Structure and Antimicrobial Activity of Alkyl Amides and Amines. *Antimicrobial Agent Chemotherapy* **1972**, *2*, 492–498.

(37) Kenawy, E. R.; Worley, S. D.; Broughton, R. The Chemistry and Applications of Antimicrobial Polymers: A State-of-Art Review. *Biomacromolecules* **2007**, *8*, 1359–1384.

(38) Kumar, S.; Dhar, D. N.; Saxena, P. N. Applications of Metal Complexes of Schiff Bases-A Review. *J. Sci. Ind. Res. India* **2009**, *68*, 181–187.

(39) Kumaraguru, N.; Santhakumar, K. Synthesis, Characterization, Critical Micelle Concentration Determination, and Antibacterial Studies of Some Complexes of Chromium (III) Metallosurfactants. *J. Coord. Chem.* **2009**, *62*, 3500–3511.

(40) Dogra, V.; Kaur, G.; Jindal, S.; Kumar, R.; Kumar, S.; Singhal, N. K. Bactericidal Effects of Metallosurfactants Based Cobalt Oxide/Hydroxide Nanoparticles Against *Staphylococcus aureus*. **2019**, *681*, 350–364.

(41) Dogra, V.; Kaur, G.; Kaur, A.; Kumar, A.; Kumar, R.; Kumar, S. In vitro Assessment of Antimicrobial and Genotoxic Effect of Metallosurfactant Based Nickel Hydroxide Nanoparticles Against *Escherichia coli* and its genomic DNA. *Colloid Surface B* **2018**, *170*, 99–108.

(42) Vugnesh, G.; Parthiban, M.; Senthilkumar, R. Molecular Interaction Studies of Some C0(III)-Surfactants with the Transport Protein. *Colloid Surface B*, **2018**, *169*¸160–167.

(43) Kaur, G.; Kumar, S.; kant, R.; Bhanjana, G.; Dibaghi, N.; Guru, S. K.; Bhushan, S.; Jaglan, S. One-Step Syntesis of Silver Metallosurfactant as an Efficient Antibacterial and Anticancer Material. *RSC Adv.* **2016**, *6*, 57084–57097.

(44) Loboda, D.; Kozlowski, H.; Rowinska-Zyrek, M. Antimicrobial Peptide–Metal Ion Interactions – a potential Way of Activity Enhancement. *New J. Chem.* **2018**, *42*, 7560–7568.

(45) Kaur, G.; Dogra, V.; Kumar, R.; Kumar, S.; Bhanjana, G.; Dilbaghi, N.; Singhal, N. K. DNA Interaction, Anti-Proliferative Effect of Copper Oxide Nanocolloids Prepared from

Metallosurfactant Based Microemulsions Acting as Precursor, Template and Reducing Agent. *Int. J. Pharmaceutics* **2018***, 535*, 95–105.

(46) Aiad, I.; Ahmed, M. H. M.; Hessein, A.; Ali, M. Preparation, Surface, and Biological Activities of Some Novel Metallosurfactants. *J. Disper. Sci. Technol.* **2012**, *33*, 1144–1153.

(47) Chaudhary, G. R.; Singh, P.; Kaur, G.; Mehta, S. K.; Kumar, S.; Dilbaghi, N. Multifaceted Approach for the Fabrication of Metallomicelles and Metallic Nanoparticles Using Solvophobic Bisdodecylaminepalladium (II) Chloride as Precursor. *Inorg. Chem.* **2015**, *54*, 9002–9012.

(48) Kaur, G.; Singh, P.; Mehta, S. K.; Kumar, S.; Dilbaghi, N.; Chaudhary, G. R. A Facile Route for the Synthesis of Co, Ni, and Cu Metallic Nanoparticles with Potential Antimicrobial Activity Using Novel Metallosurfactants. *Appl. Surf. Sci.* **2017**, *404*, 254–262.

(49) Kaur, G.; Kumar, S.; Dilbaghi, N.; Bhanjana, G.; Guru, S. K.; Bhushan, S.; Japlan, S.; Hassan, P. A.; Aswal, V. K. Hybrid Surfactants Decorated with Copper Ions: Aggregation Behavior, Antimicrobial Activity and Anti-Proliferative Effect. *Phys. Chem. Phys.* **2016**, *18*, 23961–23970.

(50) Garg, P.; Kaur, G.; Chaudhary, G. R. Transition Metal Based Single Chained Surfactant: Synthesis, Agglomeration, Aggregation Behaviour and Enhanced Photoluminescence Properties of Fluorescein. *RSC Adv.* **2016**, *6*, 108573–108582.

(51) Garg, P.; Kaur, G.; Chaudhary, G. R. Chromium-Based Metallosurfactants: Synthesis, Physicochemical Characterization and Probing of their Interacitons with Xanthene Dyes. *New J. Chem.* **2018**, *42*, 1141–1150.

(52) Garg, P.; Kaur, G.; Chaudhary, G. R.; Gawali, S. L.; Hassan, P. A. Fabrication of Metalosomes (Metal Containing Cationic Liposomes) using Single Chain Surfactants as a Precursor via Formation of Inorganic Organic hybrids. *Phys. Chem. Chem. Phys.* **2017**, *19*, 25764–25773.

(53) Kaur, G. Garg, P.; Chaudhary, G. R. Role of Manganese-Based Surfactant Towards Solubilization and Photophysical Properties of Fluorescein. *RSC Adv.* **2016**, *6*, 7066–7077.

(54) Sharma, N. K.; Singh, M. Multifunctional Supramolecular Ionic Metallosurfactants (SMIMs) for Antimicrobial, Anticancer and Serum Albumins Binding. *J. Mol. Liq.* **2018**, *263*, 463–471.

(55) Sharma, N. K.; Singh, M.; Bhattarai, A. Hydrophobic Study of Increasing Alkyl Chain Length of Platinum Surfactant Complexes: Synthesis, Characterization, Micellization, Thermodynamics, Thermogravimetrics and Surface Morphology. *RSC Adv.* **2016**, *6*, 90607–90623.

(56) Sharma, N. K.; Singh, M. New Class of Platinum Based Metallosurfactant: Synthesis, Micellization, Surface, Thermal Modelling and *in vitro* Biological Properties. *J. Mol. Liq.* **2018**, *268*, 55–65.

(57) Kaur, G.; Kumar, S.; Dilbaghi, N.; Kaur, B.; Kant, R.; Guru, S. K.; Bhushan, S.; Jaglan, S. Evaluation of Bishexadecyltrimethyl Ammonium Palladium Tetrachloride Based Dual Functional Colloidal Carrier as a Antimicrobial and Anticancer Agent. *Dalton Trans.* **2016**, *45*, 6582–6591.

(58) Adawy, A. I.; Khowdiary, M. M. Structure and Biological Behaviors of Some Metallo Cationic Surfactants. *J. Surfact. Deterg.* **2013**, *16*, 709–715.

(59) Chandar, S. C. N.; Santhakumar, K.; Arumugham, M. N. Metallosurfactant Schiff Base Cobalt (III) Coordination Complexes, Synthesis, Characterization, Determination of CMC Values and Biological Activities. *Transition Met. Chem.* **2009**, *34*, 841–848.

(60) Kaur, G.; Garg, P.; Kaur, B.; Chaudhary, G. R.; Kumar, S.; Dilbaghi, N.; Gawali, S. L. Cationic Double Chained Metallosurfactants: Synthesis, Aggregation, Cytotoxicity, Antimicrobial Activity, and their Impact on the Structure of Bovine Serum Albumin. *Soft Matter.* **2018**, *14*, 5306–5318.

(61) Briggs, D. *Surface Analysis of Polymers by XPS and Static SIMS.* Cambridge University Press, 1998, pp. 34–39.

(62) Thermo Fisher Scientific: XPS Simplified, http://xpssimplified.com/elements/carbon.php (accessed April, 08, 2019).

(63) Lascovich, J. C.; Scaglione, S. Comparison Among XAES, PELS, and XPS Techniques for Evaluation of Sp^2 Percentage in a –C:H.*Appl. Surf. Sci.* **1994**, *78*, 17–23.

(64) Stuart, B. *Infrared Spectroscopy: Fundamentals and Applications;* John Wiley & Sons: Sydney, 2004; pp. 131.

(65) Lin-Vien, D.; Colthup, N. B.; Fateley, W. G.; Grasselli, J. G. *The Handbook of Infrared and Raman Characteristic Frequencies of Organic Molecules;* Academic Press, Inc.: San Diego, 1991.

(66) Bellamy, L. J. *The Infra-Red Spectra of Complex Molecules;* Vol. 2; Chapman and Hall Ltd.: London, 1975.

(67) FTTS-FA-001 Specified Requirements of Antibacterial Textiles for General Use; The committee for Conformity Assessment of Accreditation and Certification of Functional and technical Textiles: Taiwan, 2005.

(68) Hobman, J. L.; Crossman, L. C. Bacterial Antimicrobial Metal Ion Resistance. *J. Medical Microbiol.* **2014**, *64*, 471–497.

(69) Grass, G. Rensing, C.; Solioz, M. Metallic Copper as an Antimicrobial Surface. *Appl. Environ. Microbiol.* **2011,** *77*, 1541–1547.

(70) Pontel, L. B.; Soncini, F. C. Alternative Periplasmic Copper-Resistance Mechanisms in Gram Negative Bacteria. *Molec. Microbiol.* **2009**, *73*, 212–225.

(71) Bondarczuk, K.; Piotrowska-Seget, Z. Molecular Basis of Active Copper resistance Mechanisms in Gram-Negative Bacteria. *Cell Biol. Toxicol.* **2013**, *29*, 397–405.

7. Conclusions and Further Work

In this thesis, the atomised- spray plasma deposition technique was used to fabricate functional polymer coatings for different applications, such as: liquid repellent coatings, wet electrical barrier coatings at two level of wettability, and antibacterial agent release coatings.

Atomised spray plasma deposition technique is used for surface functionalisation. This solventless and substrate-independent technique overcomes the limitation of several surface functionalisation methods, and thus, allowing the deposition of nanoparticles, viscous and low-vapour-pressure precursors, and due to the reactive plasma species, it is also possible to deposit precursors with non-polymerisable functional groups. However, the ASPD technique is limited to a certain nanoparticle concentration in the slurry mixture, which enable it to use higher nanoparticle concentrations to increase roughness in the fabrication of superhydrophobic surfaces. During the fabrication of functional polymer coatings, the precursor is atomised within electrical discharges, where electrons gain sufficient energy from the electrical discharges and thus sustain the plasma. The reactive plasma species activate the precursor molecules within the liquid/slurry droplets leading to the polymer film growth onto the plasma-activated surface.

In Chapter 3, a fluorocarbon–nanoparticle mixture was atomised into the plasma discharges to fabricate ASPD nanocomposite coatings. During the atomisation of the precursor, the liquid droplets interacted with the reactive plasma species causing the fragmentation or ionisation of the precursor molecules, and thus, impacting on the substrate surface for the subsequent plasma polymer deposition where it is suggested that the nanoparticles remained embedded within the plasma polymer matrix. The incorporation of nanoparticles to the ASPD of perfluorotributylamine layers induced surface roughness with low-surface-energy coatings yielding liquid repellent surfaces with enhanced mechanical properties. Further work on the increase of roughness can be achieved by increasing the nanoparticle concentration along with using a different spray nozzle which allows higher ultrasonic atomisation of nanoparticle–liquid slurry mixture. Even when the water contact angle value is very high, the oil contact angle value is below to those reported in the literature, thus the approach of increasing the surface roughness will consequently increase the oil contact angle value.

The plasma deposition of low-vapour-pressure precursors have been achieved by using high applied power or the use of crosslinking agents to overcome the oiliness of the plasma polymer coatings as described by other methods. In chapter 4, plasma post-treatment of the ASPD poly (isodecyl acrylate) coatings was performed to overcome the oiliness which is characteristic of previously reported approaches using the same deposition technique. This approach allows to deliver more energy per surface molecule, and thus, increasing the crosslinking degree, mechanical properties, and wet electrical barrier performance attributed to the incidence of energetic reactive plasma species (mainly vacuum UV photons). Plasma post-treatment of the ASPD poly (isodecyl acrylate) coatings remarkably enhanced the wet electrical barrier performance of the coated micro-circuit boards at an applied electrical field of 10 V mm^{-1}. Further work on this area could involve to introducing Alkyl acrylates of different alkyl chain lengths which may be possible to observe their impact on the wet electrical barrier performance. Furthermore, further chemical analysis may be carried out to study the changes of the surface chemistry of the plasma post-treated polymer coatings under the influence of the plasma post-treatment time.

In chapter 5, the incorporation of *1H,1H,2H,2H*-perfluorododecyl acrylate to fabricate the optimum ASPD 2% w/v (*1H,1H,2H,2H*-perfluorododecyl acrylate–perfluorotributylamine) coatings resulting in liquid repellent surfaces and plasma polymer coatings with high electrical strength for an applied electrical field up to 75 V mm^{-1}. The surface roughness was produced by the formation of micro-sphere-like features attributed to phase separation of the precursor mixture. The applied plasma post-treatment enhanced the mechanical and electrical barrier performance of the optimum plasma polymer coating, and no elemental composition change was observed by the XPS analysis. Further work could involve the optimization of the plasma polymer coating thickness at an applied electric field of 75 V mm^{-1}. Similarly, it is proposed to carry out further chemical analysis of the plasma post-treated plasma polymer coatings to observe the impact of the plasma post-treatment time on the surface chemistry of the samples.

In chapter 6, an antibacterial metallosurfactant, bisdodecylamine copper dichloride, was used to fabricate antibacterial ASPD poly (CuDDA–isodecyl acrylate) coatings. These antibacterial polymer coatings displayed high antibacterial activity towards both Gram-negative *E. coli*, and Gram-positive *S. aureus* bacteria, which is attributed to the synergetic effect of the antibacterial surfactant, with long alkyl

hydrophobic tail, and amine head group, and the copper ions causing faster bacteria cell death. Additionally, on this area, it may be possible to further explore other natural antibacterial compounds to be plasma polymerized and covalently bonded to the substrate surface, this may result in obtaining antibacterial polymer coatings which would be environmentally friendly with longer antibacterial activity action overcoming the limitation of the antibacterial agent release approach.

Overall, atomised spray plasma deposition has been used for the deposition of different functional coatings taking advantage of the physicochemical properties of the precursor molecules. Optimisation of the atomised spray plasma deposition experimental settings is required to prevent excessive molecular fragmentation and maintain the integrity of the precursor molecules.